Coherence in Nanostructured Excitons

by

Dylan H. Arias

B.S. Chemistry, University of California, Berkeley 2007

Submitted to the Department of Chemistry
in partial fulfillment of the requirements for the degree of

Doctor of Philosophy

at the

MASSACHUSETTS INSTITUTE OF TECHNOLOGY

June 2013

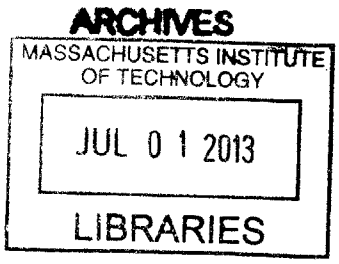

Author .....
Department of Chemistry
May 7, 2013

Certified by .....
Keith A. Nelson
Professor of Chemistry
Thesis Supervisor

Accepted by .....
Robert W. Field
Chairman, Department Committee on Graduate Theses

This doctoral thesis has been examined by a Committee of the Department of Chemistry as follows:

Professor Robert G. Griffin .....
Chairperson

Professor Keith A. Nelson .....
Thesis Supervisor

Professor Moungi G. Bawendi .....
Thesis committee member

Coherence in Nanostructured Excitons

by

Dylan H. Arias

Submitted to the Department of Chemistry
on May 7, 2013, in partial fulfillment of the
requirements for the degree of
Doctor of Philosophy

Abstract

Nanotechnology and optoelectronics have the potential to revolutionize the medicine, communications, and energy industries, with applications utilizing nanotechnology beginning to appear. However, there are still fundamental questions about optoelectronic devices incorporating nanotechnology. In particular, how do nanometer-scale materials affect potential functionality, and how can we take advantage of this scale to design nanomaterials for applications?

Natural light harvesting systems in bacteria and plants provide exquisite examples of nanomaterial design, featuring remarkably efficient light harvesting antennas. Sunlight absorption first creates excitons. Complex antenna architectures control the excitons, directing them to reaction centers for conversion to chemical energy. Recently, studies found that excitonic interactions play a significant role in controlling antennas' light harvesting abilities, and that coherence may greatly affect energy transport efficiencies. While these studies have propelled our understanding of excitons in these systems, it is desirable to extend our expertise to artificial systems. In this thesis I describe experiments uncovering many fundamental properties of excitons in various nanostructured materials, relating physical structure to excitonic structure and perhaps to subsequent function in an excitonic device.

Nonlinear spectroscopy offers distinct possibilities for detailed exploration of excitonic properties and processes in nanomaterials. Transient grating experiments are sensitive to population dynamics and energy transport, while multi-dimensional spectroscopy clearly reveals excitonic interactions, correlations, and coherence. In this thesis, these techniques are performed with a unique multi-dimensional spectrometer using femtosecond pulse shaping.

I present results on two classes of artificial nanostructures: supramolecular J-aggregates and semiconductor quantum wells. In J-aggregate thin films I determined that coherence is controlled by thermal dephasing rather than film inhomogeneities, even at cryogenic temperatures. Tubular J-aggregates in solution undergo morphological rearrangement while maintaining a common sub-unit that remains relatively intact both structurally and excitonically. In semiconductor quantum wells, many-body correlations among excitons were shown to decay on the timescale picoseconds,

depending on the exciton density and therefore revealing of high-order correlations.

These insights into coherence and excitonic structure are important in determining the origin and strength of coherence in excitonic systems, potentially leading toward methods to alter or control exciton dynamics and toward possible novel application of coherence in optoelectronic devices.

Thesis Supervisor: Keith A. Nelson
Title: Professor of Chemistry

Acknowledgments

This thesis is the culmination of a dream, lived and breathed every day alongside my wife.

Learning, inquiry, and people are the foundation for this dream. It began in second grade when my teacher, Mrs. Youngs, had us discuss what we thought "science" was, what is a hypothesis, what does it mean to "test" a hypothesis. We put our ideas into practice with memorable experiments involving two rats that lived in a cage in the classroom. We would give them a series of challenges and see how completed them. I serendipitously found myself in Mrs. Youngs class again in fourth grade and our explorations into the scientific method continued. However, this time we came up with our own hypotheses and tests. I enjoyed the field of optics, although I didn't know it as such at the time, and chose to figure out how optical illusions work. I created a series of illusions, based on those I found in books from the library, and asked people what they saw when looking at the different illusions, and why they thought the illusions worked or didn't work.

This enjoyment of inquiry-based exploration did not develop significantly further until I attended high school, when I began taking chemistry, physics, and calculus. Mr. Dempsey, my calculus teacher who by coincidence graduated from MIT, stands out as prominently altering my world view with mathematics. In addition, he amazingly gave a book to each and every student tailored to their own curiosity; my book was "Four Great Ideas in Physics" and covered quantum mechanics, energy conservation, the second law of thermodynamics, and relativity. This singular action had a profound effect upon me: I wanted to be a scientist.

The dream continued into college, where I studied chemistry at UC Berkeley. My first graduate student instructor, Delphine Farmer, and my first chemistry professor, Ron Cohen, introduced me to the world of studying chemistry and physics for the benefit of people, to figure out solutions to immense problems. My phsyics professor Dunghai Lee led me through the mathematical complexity that is quantum mechanics. At this point, I knew I wanted to use quantum mechanics to study problems that

affect many people, specifically focusing on energy and the environment.

I entered graduate school with the plan of using spectroscopy to study quantum mechanical systems. I am grateful to my ever-energetic advisor with boundless enthusiasm, Keith Nelson. He gave me the platform for launching into projects that I desired, and the freedom to pursue them with all the gusto I could muster. Kathy Stone, Duffy Turner, and Kenan Gundogdu were the initial people working in my sub-group, who taught me everything practical in terms of being a scientist: how do to do science in the lab every day, how to think like a scientist every day.

Patrick Wen joined the Nelson group the same time I did, and we have had such an adventure that he deserves his own paragraph.

The people that fill my everyday life make working in science possible. Steph, forever to my left with a glare and smile; OGW, ever ready for a furious round of insults; Colby, my eager, incredibly thoughtful, and spectacularly capable greenhorn; Sharly, with his constant threatening and posturing; Kit, an endless source of rules and workplace-appropriate humor; Kara, the enthusiastic bike-ready explorer; Jeff, our 6'-8" champion of champions; and Harold, the whiskey-loving fountain of great ideas.

The entirety of the Nelson group, both past and present (including Raoul), made graduate school a thoroughly transformative and amazing experience, both professionally and personally, and I can't thank them enough.

I must acknowledge all my wonderful collaborators as well, it could not have and would not have happened without you. Yaakov Tischler, Gleb Akselrod and Vladimir from the Bulović group, Joel and Alan from the Aspuru-Guzik group, and Dörthe Eisele and Moungi from the Bawendi group. Dörthe in particular, your joyful, enthusiastic outlook is inspiring and unquenchable.

My parents started the dream. To my mom, who gave me the drive and desire to accomplish. To my dad, who gave me the humor and happiness to survive. To you both, who gave me the resilience, ability, and well-being to become who I am.

Elizabeth Louise Lemon, while we may not be driving around in a van solving mysteries, every day I dream a little dream of you.

Contents

1 Introduction **19**

2 Spectroscopy **23**

2.1 The Semi-Classical Description of Spectroscopy 23

2.1.1 Macroscopic Polarization 24

2.1.2 Light-Matter Interaction 25

2.2 Linear Spectroscopy 27

2.2.1 Response Function Formalism 27

2.3 Coherence and Dephasing 29

2.4 Nonlinear Spectroscopy 32

2.4.1 Diagrammatic Perturbation Theory 33

2.4.2 Phase-Matching 35

2.5 Nonlinear Techniques 35

2.5.1 Pump-Probe and Transient Grating 35

2.5.2 Photon Echo Spectroscopy 38

2.5.3 Two-Quantum Spectroscopy 39

2.5.4 Multi-Dimensional Spectroscopy 39

2.6 Detection Methodology for Nonlinear Experiments 43

2.6.1 Heterodyne Detection and Spectral Interferometry 44

2.6.2 Rotating Frame Detection 46

3 Experimental Setup **47**

3.1 Ultrafast laser system 47

3.2 Noncollinear Optical Parametric Amplifier 47
3.3 Pulse Shaping 49
3.3.1 Beam Pattern Generation 49
3.3.2 Temporal Pulse Shaping 50
3.3.3 Wavevector Shaping 52
3.3.4 Diffraction-Based Pulse Shaping 52
3.4 Pulse Shaping Calibrations 54
3.4.1 Phase to Grayscale 55
3.4.2 Pixel to Wavelength 56
3.4.3 Temporal Distortions 56
3.4.4 Carrier Frequency 57
3.5 Transient Grating Spectroscopy 58

4 *J*-Aggregates **61**
4.1 Linear J-aggregate Model 62
4.1.1 Frenkel Exciton Hamiltonian 62
4.1.2 Idealized Many-Site Model 63
4.2 Disordered Aggregate Model 66
4.2.1 Static Disorder 67
4.2.2 Exciton-Phonon Interactions 70
4.3 Two-Exciton States 74
4.4 Tubular J-aggregates 75

5 Exciton Delocalization in Superradiant Molecular Aggregate Films 81
5.1 Motivation and Background 81
5.2 Nonlinear Spectroscopy Applied to J-aggregates 83
5.3 Experimental Details 85
5.4 Theoretical Description 87
5.4.1 Excitons in One Dimension 87
5.4.2 Excitons in Two Dimensions 90
5.5 Exciton Coherence Lengths and Dephasing 91

5.6 Conclusions 96

6 Morphology and Excitonics in Supramolecular Nanotubes 99

6.1 Introduction 100

6.2 Electron Microscopy and Linear Spectroscopy 102

6.2.1 TEM of Supramolecular Nanotubes 102

6.2.2 Polarized Linear Spectroscopy 103

6.3 2D Spectroscopy of Nanotubes 106

6.4 Microscopic Model for Isolated Inner Wall 113

6.5 Conclusions 115

7 Quantum Process Tomography of Supramolecular Excitons 117

7.1 Quantum Process Tomography Methodology 118

7.1.1 Basic Method 118

7.1.2 Example V-Level Excitonic System 122

7.2 QPT of Nanotubular Excitons 130

7.2.1 Experimental Parameters 130

7.2.2 Transient Grating Results 130

7.2.3 QPT Results 134

7.3 Conclusions 138

8 Many-Body Effects in Quantum Wells 139

8.1 Semiconductor Quantum Wells 140

8.2 Experimental Details 142

8.3 2D Spectra and Analysis 143

8.3.1 2D Correlation Spectra 143

8.3.2 Lineshape Analysis 145

8.4 Excitonic Many-Body Interactions 147

8.5 Conclusions 149

9 Conclusions and Outlook 151

A Additional QPT Feynman Diagrams 155

List of Figures

2-1 Absorption of a Two-Level System 28
2-2 Interference of Sinusoids 30
2-3 Feynman Diagrams 34
2-4 Phase-Matching Conditions 36
2-5 Time-Domain Photon Echo 40
2-6 Two-Dimensional Photon Echo 41
2-7 Correlation Spectrum 42
2-8 Three-Level System 43

3-1 NOPA Optical Design 48
3-2 Pulse Shaping Optical Design 50
3-3 Multi-Dimensional Spectrometer 55
3-4 Carrier Frequency Calibration 57
3-5 Transient Grating Setup 58

4-1 BIC and U3 Cyanine Dye Molecular Structure 61
4-2 Dimeric Energetics and Dipoles 63
4-3 Many-Site Aggregate 63
4-4 Homogeneous Aggregate Properties 65
4-5 Homogeneous Aggregate Absorption Spectrum 66
4-6 Disordered Aggregate Properties 68
4-7 Disordered Aggregate Absorption Spectrum 69
4-8 Aggregate Absorption Spectrum 74
4-9 C8S3 Cyanine Dye Nanotubes 76

4-10 C8S3 Dye and Nanotube Optical Spectra 77
4-11 Nanotube Geometrical Model 79

5-1 Exciton Delocalization Experiment 84
5-2 Thin Film J-aggregate Correlation Spectra 92
5-3 Temperature-Dependent Coherence Length 94
5-4 Thin Film J-aggregate Photon Echoes 95
5-5 Temperature-Dependent Exciton Dephasing 95
5-6 Dephasing-Controlled Exciton Delocalization 96

6-1 Nanotubular J-aggregate System 101
6-2 Nanotube Morphology 104
6-3 Nanotube Linear Dichroism 105
6-4 2D ES Polarization Schemes 107
6-5 HHHH Feynman Diagrams 108
6-6 HHVV Feynman Diagrams 109
6-7 Bundled 2D ES HHVV Feynman Diagrams 110
6-8 Nanotubular 2D ES 111
6-9 Optical Spectroscopy of Clusters and Isolated Nanotubes 113
6-10 Optical Spectrum and Model of Single-wall Nanotube 114
6-11 Nanotubular Morphological Change 115

7-1 QPT and Feynman Diagrams 121
7-2 V-Level Excitonic System and QPT Experiment 122
7-3 QPT Feynman Diagrams 124
7-4 QPT Transfer Feynman Diagrams 125
7-5 Linear Absorption and Pulses for QPT 131
7-6 Nonlinear Spectroscopy QPT 132
7-7 Nonlinear experiment IIO 133
7-8 Process Matrix Elements 135
7-9 Calculated Nanotube Populations 136

8-1 Quantum Well Experiment 142
8-2 Quantum Well Correlation Spectra 144
8-3 Many-Body Interaction Time Dependence 146
8-4 Excitonic Scattering 148

A-1 QPT Population Feynman Diagrams 156
A-2 QPT Coherence Feynman Diagrams 157

List of Tables

4.1 Properties of Aggregates and Particle-in-a-box 65

Chapter 1

Introduction

Nanotechnology and optoelectronic devices have revolutionized the world of communications and hold great promise for the development of energy and medical technologies from photovoltaic cells to optical computing and biomedical imaging [1, 2]. The full potential of these technologies can only be realized if we understand both the optical and electronic components. Excitons are the fundamental unit of electronic excitation in many of the nanomaterial systems, typically created via absorption of a photon [3, 4]. Therefore, the study of excitons is vitally important to understanding, controlling, and designing optoelectronic device functionality for novel applications.

Control of nanoscale structure and morphology grants unprecedented control of excitonic properties in both organic and inorganic systems [5, 6]. Exciton wavefunctions, dynamics, and interactions can be engineered using quantum confinement effects, dimensionality, and geometry [7, 8, 9]. Exciton-exciton interactions and correlations lead to effects such as coherence, supertransfer, and enhanced nonlinearities; while exciton interactions with the environment are important for energy and coherence dissipation [5, 10]. Of particular interest are natural light harvesting antenna complexes, optimized through billions of years of evolution to take advantage of nanoscale effects for highly efficient and highly robust light harvesting and energy conversion in plants and bacteria [11, 12, 13, 14]. An artificial photosynthetic system with the ability to efficiently capture sunlight and cheaply convert it into usable electrical energy or storable fuels would cause a significant transformation of the field of energy

technology with wide ranging implications for society as a whole.

A complete understanding of natural photosynthesis would immensely benefit our efforts toward an artificial system [15, 13, 14]. However, this understanding remains elusive due to the complexity and scale of the complete photosynthetic cycle, which covers many orders of magnitude in both size and duration [12, 16]. On the shortest length scales (nanometers) and time scales (femtoseconds), on which the initial steps in photosynthesis occur, individual chromophore molecules are arranged into absorbing antenna complexes with a few to a few hundred thousand molecules per antenna [17, 18]. The interactions among the chromophores and their interactions with the surrounding environment determine the optical properties, e.g. the absorption spectrum, and exciton dynamics. Typically the antennas are treated as excitonic systems weakly coupled to the environment. There are several examples of light harvesting antenna complexes with a determined structure, allowing optical spectroscopy experiments to probe the excitonic band structure and dynamics in a meaningful way and provide insight on the exciton-environment interactions that determine the efficiencies of the complexes [17, 19, 20, 21, 22]. For example, the Fenna-Matthews-Olson complex has been studied as a model antenna complex that acts as a quantum wire that may utilize excitonic coherence to quickly transport energy to a reaction center [23, 20].

In the last few decades nonlinear optical spectroscopy has emerged as the technique of choice for studying exciton properties and dynamics [24, 25, 26, 27, 28, 29, 19, 30, 31]. Pump-probe, transient grating, and photon echo spectroscopy began to reveal the relationship between excitons and the environment, the types of solvent modes interacting with the excitons, and the strength of those interactions [25, 26, 32, 33]. Coherent spectroscopy, notably multi-dimensional photon echo spectroscopy and multiple-quantum spectroscopy, has led efforts to disentangle coherence and correlations among excitons from population effects as well as the role they may play in guiding transport and enhancing energy transfer efficiency [20, 34, 21, 35, 31, 22].

The insights gained from these advanced characterization techniques have greatly benefited efforts to construct artificial light harvesting complexes and other optoelec-

tronic structures using advanced materials and geometrical architectures [36, 7, 37, 13, 14]. Supramolecular J-aggregates, initially discovered in the 1930s [38, 39, 40], self-assemble from different types of chromophore dye molecules and resemble some natural light harvesting systems [41, 40, 42]. New morphologies continue to be developed including tubular structures [43, 44, 45, 46, 47, 48], oriented and monolayer thin films [49, 50, 51, 52], and aggregates electrostatically linked to quantum dots and semiconductor nanowires [53, 54, 55, 56]. Nonlinear optical techniques including transient grating, photon echo, and multi-dimensional spectroscopy have been applied to various J-aggregate morphologies to study the exciton dynamics and interactions and have elucidated the nature of coherence in these systems [57, 58, 59, 60, 61, 62, 63, 64, 65, 66, 67, 68, 69, 70]. This insight has benefited their use in potential applications such as polariton lasers and ultrafast optical switches [71, 72, 73, 74, 75].

Excitons in inorganic semiconductors, termed Wannier excitons, provide a contrasting set of physical properties for developing excitonic devices [6]. Weak dielectric screening and the support for high carrier concentrations lead to possibilities for several applications [5]. In addition, semiconductor architectures typically do not suffer from the drawbacks of structural and morphological inhomogeneity and are much more photostable, although they may be more expensive and energy intensive to produce. Still, they have found widespread use in e.g. photovoltaics, communications, and computing. Nonlinear spectroscopy techniques have also been applied to semiconductors to explore exciton dynamics and correlations [76, 77, 6, 78]. Those studies yield different yet complementary insight to the nature of excitonic coherence and interactions in nanostructured materials.

This thesis is organized in the following fashion. First I introduce linear and nonlinear spectroscopy in Chapter 2. Then I develop the background and methodology of our experimental apparatus, beginning with the Coherent Libra amplifier laser system and ending with a description of the multi-dimensional spectrometer and the transient grating setup. Next I give a brief overview of J-aggregates with descriptions of delocalized Frenkel excitons and their properties. In Chapter 5 I present

the temperature-dependence of exciton delocalization in thin films of J-aggregates. Chapter 6 continues with J-aggregates of the tubular variety. Exciton interactions and coherence in these self-assembled supramolecular nanotubes are determined via multi-dimensional spectroscopy, and the correlation between excitonic changes and morphological rearrangement is determined with a combination of electron microscopy and linear and nonlinear spectroscopy. Results on quantum process tomography are presented in the next chapter as examples of a new methodology for interpreting nonlinear spectroscopy experiments. In Chapter 8 I discuss a different class of excitons, in Gallium Arsenide semiconductor quantum wells, determining the time-dependence of many-body effects using multi-dimensional spectroscopy. Finally, I conclude with a brief reflection on the work that comprises this thesis as well as future directions for these projects and others.

Chapter 2

Spectroscopy

Spectroscopy is the science of understanding matter using light. It ranges across the electromagnetic spectrum from radio waves to gamma rays including many techniques from time-resolved microwave conductivity to Raman spectroscopy to X-ray diffraction. The experiments described in this thesis aim to understand how electrons behave when excited. The techniques used fall into the general category of resonant electronic spectroscopy which I describe in the following chapter.

I begin by describing the interaction between light and matter using a semi-classical approach. I then introduce the methodology used to understand both linear and nonlinear spectroscopy and how different physical phenomena manifest in an optical spectrum. Next, I go through several nonlinear spectroscopy techniques used to separate and quantify those phenomena. Finally, I describe multi-dimensional electronic spectroscopy and the technical challenges associated with performing multi-dimensional spectroscopy experiments. For an excellent in-depth tutorial on most of the topics covered in this chapter see Andrei Tokmakoff's Nonlinear Spectroscopy notes [79].

2.1 The Semi-Classical Description of Spectroscopy

In classical electricity and magnetism, electromagnetic waves (light) pass through and interact with matter according to Maxwell's Equations [80, 81]. The light waves

generate a macroscopic polarization that depends only on the average (ensemble) properties of the material without requiring a detailed description of the microscopic basis for the ensemble properties. The semi-classical approach attempts to bridge the macro- and microscopic worlds by treating the material on a microscopic, perturbative and fully quantum mechanical level; while leaving the light waves as classical fields essentially unchanged by the quantum system [82, 25].

2.1.1 Macroscopic Polarization

I start with the classical description of the macroscopic response of the system to an incident light wave, the polarization [80]. The simplest case is when the polarization $\vec{P}$ is linearly proportional to the incident light field $\vec{E}$,

$$\vec{P}\left(\vec{k},\omega\right) = \chi(\omega)\vec{E}\left(\vec{k},\omega\right). \tag{2.1}$$

As indicated in Equation 2.1 the polarization and linear susceptibility are functions of light frequency ω and direction (wavevector $\vec{k}$). In Maxwell's Equations, $\vec{P}$ acts as a source term for the output light wave $\vec{E}_{out}$, leading to a dependence of $\vec{E}_{out}$ on $\vec{P}$,

$$\vec{E}_{out}\left(\vec{k},\omega\right) = i\frac{2\pi\omega l}{nc}\vec{P}\left(\vec{k},\omega\right) sinc\left(\frac{\Delta\vec{k}l}{2}\right) e^{i\Delta\vec{k}l/2}, \tag{2.2}$$

where l is the system length, n is the index of refraction, c the speed of light, and $\Delta\vec{k}$ the directional (wavevector) mismatch. For large wavevector mismatch, $\vec{E}_{out}$ vanishes. To first order this requires the output electric field to travel in the same direction as the input electric field for the linear macroscopic response.

In general the polarization is not linearly proportional to the electric field and contains both linear and nonlinear components,

$$\vec{P}\left(\vec{k},\omega\right) = \chi^{(1)}(\omega)\vec{E}\left(\vec{k},\omega\right) + \chi^{(2)}(\omega)\vec{E}^2\left(\vec{k},\omega\right) + \chi^{(3)}(\omega)\vec{E}^3\left(\vec{k},\omega\right) + \ldots \tag{2.3}$$

This thesis utilizes two of the nonlinear terms: $\chi^{(2)}$ processes (second-harmonic gen-

eration and parametric scattering) are used in the NOPA as described in Section 3.2 while the experiments themselves are derived from $\chi^{(3)}$ processes. We can explore the $\chi^{(3)}$ processes in further detail, approximating the electric fields as envelopes $a_n(t)$ times carrier waves, $\vec{E}_n\left(\vec{k},\omega\right) = a_n(t)e^{i(\vec{k}_n\cdot r-\omega_n t)} + c.c.$, and expanding the third-order term,

$$\begin{aligned}\vec{P}^{(3)}\left(\vec{k},\omega\right) = \chi^{(3)}(\omega) \times\ & a_1a_2a_3e^{i(\vec{k}_1+\vec{k}_2+\vec{k}_3)\cdot r-i(\omega_1+\omega_2+\omega_3)t} + \\ & a_1^*a_2a_3e^{i(-\vec{k}_1+\vec{k}_2+\vec{k}_3)\cdot r-i(-\omega_1+\omega_2+\omega_3)t} + \\ & a_1a_2^*a_3e^{i(\vec{k}_1-\vec{k}_2+\vec{k}_3)\cdot r-i(\omega_1-\omega_2+\omega_3)t} + \\ & a_1a_2a_3^*e^{i(\vec{k}_1+\vec{k}_2-\vec{k}_3)\cdot r-i(\omega_1+\omega_2-\omega_3)t} + c.c. \end{aligned} \tag{2.4}$$

From Equation 2.4 it is clear that several signals are generated during the nonlinear process. According to the phase-matching condition $\Delta\vec{k} = 0$ from Equation 2.2, the signals propagate in well-defined directions allowing for spatial selection of the signal of interest.

2.1.2 Light-Matter Interaction

In the semi-classical approach the material of interest and the light-matter interaction are quantum mechanical [79, 25]. The Hamiltonian takes the form

$$H(t) = H_0 + V(t) = H_0 - \vec{\mu}\cdot\vec{E}(t), \tag{2.5}$$

where H_0 is the material Hamiltonian and $V(t) = -\vec{\mu}\cdot\vec{E}(t)$ is the light-matter interaction potential consisting of the dipole operator $\vec{\mu}$ dotted with the electric field. Using the density matrix $\rho(t) = |\psi\rangle\langle\psi|$ as opposed to wavefunctions $|\psi\rangle$ [83] simplifies the derivation and manipulation of the equations for nonlinear spectroscopy. The Schrödinger equation becomes the Liouville-Von Neumann equation for the time-dependence of the density matrix,

$$\frac{\partial \rho}{\partial t} = -\frac{i}{\hbar}[H, \rho]. \tag{2.6}$$

The interaction picture removes the dependence on the material Hamiltonian H_0 and isolates the light-matter interaction. In the interaction picture, $\rho_I = U_0^\dagger \rho U_0$ and $V_I(t) = U_0^\dagger V(t) U_0$ with the time propagator $U_0 = \exp_+[-\frac{i}{\hbar}\int_{t_0}^{t} H_0(t')\,dt']$. The Liouville-Von Neumann equation becomes

$$\frac{\partial \rho_I}{\partial t} = -\frac{i}{\hbar}[V_I(t), \rho_I]. \tag{2.7}$$

Equation 2.7 can be integrated to obtain

$$\rho_I(t) = \rho_I(t_0) - \frac{i}{\hbar}\int_{t_0}^{t} [V_I(t'), \rho_I(t')]\,dt'. \tag{2.8}$$

Substituting this equation into itself gives a perturbation expansion series, of which the first- and third-order terms most relevant to the spectroscopy in this thesis are

$$\rho_I^{(1)}(t) = -\frac{i}{\hbar}\int_{-\infty}^{t} [V_I(t_1), \rho_{eq}]\,dt_1. \tag{2.9}$$

$$\rho_I^{(3)}(t) = -\left(\frac{i}{\hbar}\right)^3 \int_{-\infty}^{t} dt_3 \int_{-\infty}^{t_3} dt_2 \int_{-\infty}^{t_2} dt_1\, [V_I(t_3), [V_I(t_2), [V_I(t_1), \rho_{eq}]]]\,. \tag{2.10}$$

The macroscopic polarization is obtained directly from the density matrix and dipole operator, $P(t) = Tr\,(\mu_I(t)\rho_I(t))$, and each perturbative term in ρ_I leads to a corresponding term in the series expansion of the polarization in Equation 2.3,

$$P = P^{(1)} + P^{(2)} + P^{(3)} + \ldots = Tr(\mu_I \rho_I^{(1)}) + Tr(\mu_I \rho_I^{(2)}) + Tr(\mu_I \rho_I^{(3)}) + \ldots \tag{2.11}$$

In the next several sections I describe the results for the first-order and third-order polarizations and how we use them to interpret various linear and nonlinear optical spectroscopy experiments. In addition, I show how physical phenomena such as

dephasing dynamics and absorption and dispersion manifest in experiments.

2.2 Linear Spectroscopy

Materials that have a dipole-allowed transition from the ground state to an excited state will enact frequency-dependent changes upon an input light wave. Linear changes in the phase (dispersion) and amplitude (absorption) of the light map to the real and imaginary parts, respectively, of the index of refraction and are directly related to the linear susceptibility (Equation 2.1). With some manipulations we can re-write the polarization in terms of the input electric field and a response function which we can use to find the linear susceptibility. The linear polarization is determined by the light-matter interaction potential and the density matrix,

$$P^{(1)}(t) = -\frac{i}{\hbar}\int_{-\infty}^{t} Tr\left(\mu_I[V_I(t_1), \rho_{eq}]\right)\, dt_1. \tag{2.12}$$

Rearranging Equation 2.12 and using $V_I(t) = -\mu_I \cdot E(t)$ leads to

$$P^{(1)}(t) = \frac{i}{\hbar}\int_{0}^{\infty} E(t-\tau) Tr\left([\mu_I(\tau), \mu_I(0)]\rho_{eq}\right)\, d\tau. \tag{2.13}$$

Equation 2.13 resembles linear response theory, where an output response, $P^{(1)}(t)$, linearly depends on the input driving force, $E(t-\tau)$, with the response function $R^{(1)}(t)$ the proportionality constant. From Equation 2.13, $R^{(1)}(t) = Tr\left([\mu_I(\tau), \mu_I(0)]\rho_{eq}\right)$. Comparing Equations 2.13 and 2.1 it is clear that $R^{(1)}(t)$ and $\chi^{(1)}(\omega)$ are related by a Fourier transform. Thus, by finding the response of the system using the dipole operator and the density matrix we can simply do a Fourier transform to find the frequency-dependent dispersion and absorption spectrum, related to the real and imaginary parts of $\chi^{(1)}(\omega)$, respectively.

2.2.1 Response Function Formalism

In this section I use a simple example, a two-level system, to demonstrate how the response function $R^{(1)}(t)$ translates to absorption and dispersion spectra. The two-

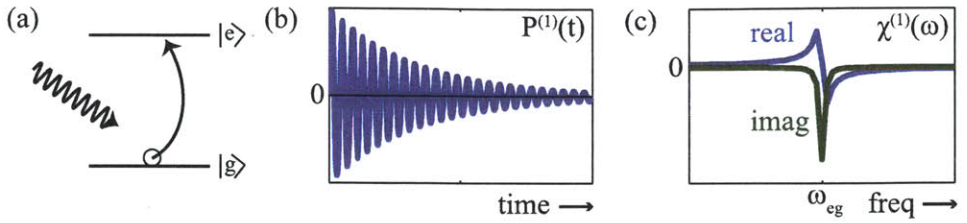

Figure 2-1: Linear absorption example. (a) Two-level system. (b) Time domain polarization. (c) Frequency domain susceptibility, with real (blue) and imaginary (green) components.

level system has a ground state, $|g\rangle$, and an excited state, $|e\rangle$, accessible by light absorption (Figure 2-1(a)). $R^{(1)}(t)$ for this system is calculated using the two-level Hamiltonian H_0, time propagator U_0, and the transition dipole moment μ which connects $|g\rangle$ and $|e\rangle$,

$$\begin{aligned} H_0 &= \epsilon_g|g\rangle\langle g| + \epsilon_e|e\rangle\langle e|, \\ U_0 &= \exp(iH_0t/\hbar), \\ \mu(t) &= U_0^\dagger \mu U_0,\ \mu = \mu_{ge}|g\rangle\langle e| + \mu_{eg}|e\rangle\langle g|. \end{aligned} \tag{2.14}$$

Combining the equation for $R^{(1)}(t)$ and Equation 2.14 leads to

$$R^{(1)}(t) = |\mu_{eg}|^2 \sin(\omega_{eg}t) \tag{2.15}$$

with $\omega_{eg} = \left(\frac{\epsilon_e - \epsilon_g}{\hbar}\right)$. Furthermore, using a δ-pulse, adding a phenomenological damping parameter (discussed further in Section 2.3), and combining Equation 2.15 with Equation 2.13 leads to,

$$P^{(1)}(t) \propto R^{(1)}(t) = |\mu_{eg}|^2 \sin(\omega_{eg}t)e^{-\gamma_{eg}t}. \tag{2.16}$$

This result is plotted in Figure 2-1(b). The Fourier transform of the damped oscillating signal has both real and imaginary parts, corresponding to the dispersive and

absorptive responses, respectively (Figure 2-1(c)). The absorptive part is peaked at the energy difference, ω_{eg}, reflecting the resonant nature of the interaction with light.

2.3 Coherence and Dephasing

There are multiple ways to interpret the oscillating polarization in Figure 2-1(b). In the classical and possibly more intuitive picture, the polarization results from spatially-dependent oscillations in the system of interest. In the case of molecules it is easy to picture bonds vibrating or twisting giving rise to infrared radiation and vibrational spectroscopy; or electron clouds oscillating across the relatively fixed backbone of nuclei leading to electronic spectroscopy. The process of absorption occurs when an oscillating electric field polarizes the charge density of the system. The charge density (or polarization) oscillates at the resonant frequency and emits an oscillating electric field exactly out of phase with the incoming electric field, causing destructive interference and therefore net absorption.

Quantum mechanics offers a similar picture but with perhaps less intuitive language. When calculating the polarization, the density matrix and transition dipole operator act in conjunction. The elements of the density matrix simply describe the wavefunction of the system: diagonal terms relate to the population in different eigenstates whereas off-diagonal terms relate to *coherences*, i.e. superpositions, among eigenstates. The light-matter interaction requires the density matrix to contain off-diagonal amplitude in order to create a polarization, meaning that a superposition of eigenfunctions must exist in the system, that the system exists in a *coherence*. The coherent superposition state is responsible for driving the polarization and eventually emitting photons.

Creating a coherence is different than changing the population in the system eigenstates (diagonal density matrix elements). Whereas creating a coherence requires a single electric field interaction, transferring population between eigenstates requires two electric field interactions because both the bra and ket of the density matrix ($\rho = |\psi\rangle\langle\psi|$ must change from the initial to final state, whereas a coherence only

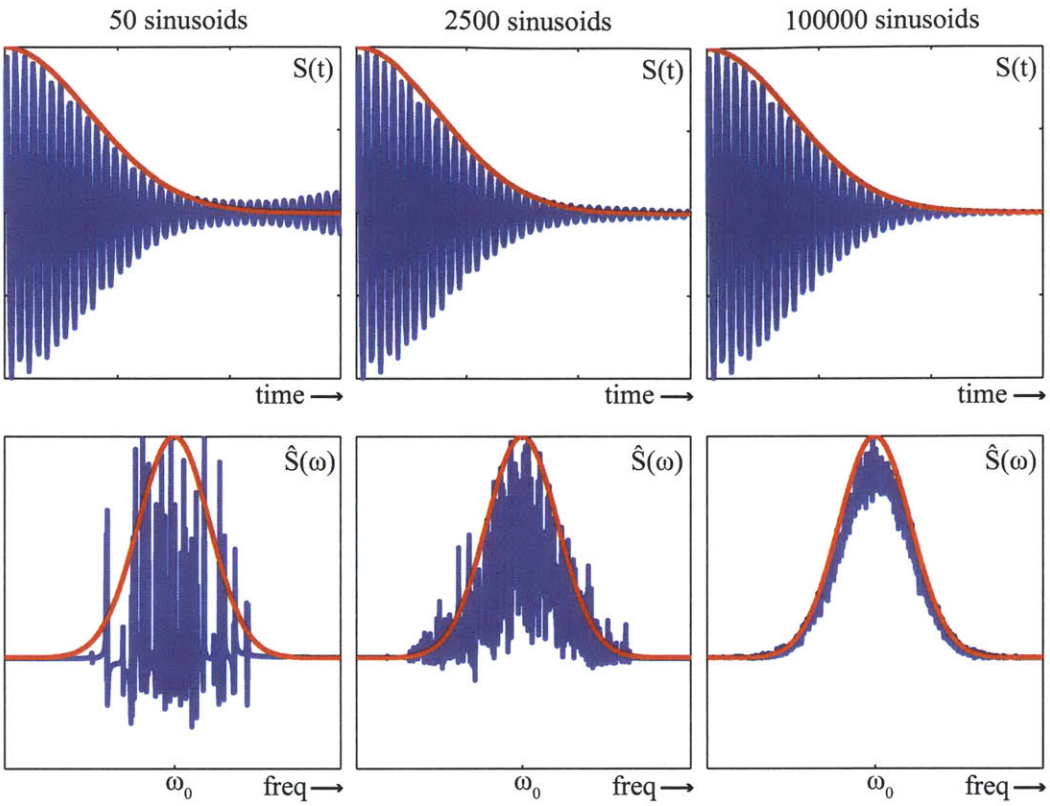

Figure 2-2: Addition of undamped sinusoidal functions with the frequencies taken from a gaussian distribution, demonstrating inhomogeneous dephasing. Going from left to right there are an increasing number of time-domain sinusoids added together, increasing the destructive interference at longer times. Top panels show the resulting time domain signal $S(t)$, bottom panels show the Fourier transform of the time domain signal,$\hat{S}(\omega)$. In red are the analytical gaussian functions.

requires one to change.

The connection between the classical description and quantum mechanical coherence is the fact that eigenstates are stationary states with a static wavefunction. In quantum mechanics any motion, spatial or otherwise, is a direct result of coherence among multiple eigenstates. For example, a vibrating bond may be composed of several eigenstates whose superposition leads to an oscillating nuclear wavefunction. Similarly, an electron cloud oscillating across a molecule is composed of a coherence among electronic eigenstates that leads to an oscillating electronic wavefunction.

There are two main classes of damping (or decoherence) that reduce the coherence,

and therefore the polarization, after creation. The first is irreversible and ubiquitous, termed homogeneous dephasing or dynamic dephasing. The system, whether it be vibrations, excitons, electrons, etc., is always coupled to a fluctuating environment and always exhibits homogeneous dephasing. This disorder causes fluctuations in the system, e.g. nuclear positions, atomic/molecular energies, which cause random and time-dependent phase changes in the wavefunctions and therefore in the coherences. This manifests in spectroscopy as exponential damping of coherent oscillations (see Figure 2-1(b)).

Inhomogeneous dephasing is the second class of dephasing. If there is a separation of fluctuation timescales, then the fast fluctuations lead to homogeneous dephasing and the slow fluctuations lead to inhomogeneous dephasing. The slow fluctuations appear as static disorder, such as the different configurations of a protein affecting vibrational frequencies or variability in the sizes of semiconductor nanocrystal quantum dots leading to a distribution of exciton energies. For systems exhibiting small homogeneous dephasing the polarizations and coherences can still decay very quickly because oscillations with a distribution of frequencies interfere destructively to reduce the signal. The signals in Figure 2-2, composed by the addition of sine waves of varying frequencies, demonstrate this effect . The frequencies are taken from a gaussian distribution, simulating a random distribution of frequencies. Even for 50 sine waves (left panels) the coherence damps fairly quickly, however a clear temporal revival occurs at the edge of the panel. The Fourier transform (bottom left panel) shows the different frequencies of the sine waves. For 2500 sine waves (middle panels), the revival is greatly reduced and the Fourier transform resembles the original gaussian distribution. The time domain and frequency domain signals from $100,000$ sine waves (right panels) follow the analytical gaussian distribution very closely.

There are many different models to include both homogeneous and inhomogeneous dephasing. Many of the models culminate in a description of the lineshape function, $g(t)$; for the two-level model above $g(t) = -\gamma_{eg}t$. In general, the lineshape function can take many forms and is included in the polarization in an exponential,

$$P^{(1)}(t) \propto |\mu_{eg}|^2 \sin(\omega_{eg}t)e^{-g(t)}. \tag{2.17}$$

For systems that exhibit the effects of homogeneous and inhomogeneous dephasing simultaneously the linear polarization and linear spectroscopy in general is insufficient to separate the magnitudes of either or to determine the mechanism. The next sections describe nonlinear spectroscopy techniques specifically designed to examine directly homogeneous versus inhomogeneous dephasing, energy transfer dynamics, and coherence and correlations in general.

2.4 Nonlinear Spectroscopy

Nonlinear spectroscopy is the study of light-matter interactions when the system response and polarization depend on many electric field interactions. In this section I extend the analysis from Section 2.1.2 to the nonlinear polarization, specifically $P^{(3)}$, using Equations 2.10 and 2.11. $P^{(3)}$ is obtained using similar substitutions as for the linear polarization, leading to

$$P^{(3)}(t) = \int_0^\infty d\tau_3 \int_0^\infty d\tau_2 \int_0^\infty d\tau_1 R^{(3)}(\tau_3,\tau_2,\tau_1)E_3(t-\tau_3)E_2(t-\tau_3-\tau_2)E_1(t-\tau_3-\tau_2-\tau_1) \tag{2.18}$$

$$R^{(3)}(\tau_3,\tau_2,\tau_1) = \left(-\frac{i}{\hbar}\right)^3 Tr\left([[[\mu_I(\tau_3+\tau_2+\tau_1),\mu_I(\tau_2+\tau_1)],\mu_I(\tau_1)],\mu_I(0)]\rho_{eq}\right) \tag{2.19}$$

Expanding the commutators and rearranging several terms leads to a simplified form for $R^{(3)}(\tau_3,\tau_2,\tau_1)$,

$$R^{(3)}(\tau_3,\tau_2,\tau_1) = \left(-\frac{i}{\hbar}\right)^3 \sum_{\alpha=1}^{4} R_\alpha(\tau_3,\tau_2,\tau_1) - R_\alpha^*(\tau_3,\tau_2,\tau_1) \tag{2.20}$$

$$\begin{aligned}
R_1 &= Tr\left(\mu_I(\tau_3+\tau_2+\tau_1)\mu_I(\tau_2+\tau_1)\mu_I(\tau_1)\mu_I(0)\rho_{eq}\right) \\
R_2 &= Tr\left(\mu_I(\tau_3+\tau_2+\tau_1)\mu_I(\tau_1)\rho_{eq}\mu_I(0)\mu_I(\tau_2+\tau_1)\right) \\
R_3 &= Tr\left(\mu_I(\tau_3+\tau_2+\tau_1)\mu_I(\tau_2+\tau_1)\rho_{eq}\mu_I(0)\mu_I(\tau_1)\right) \\
R_4 &= Tr\left(\mu_I(\tau_3+\tau_2+\tau_1)\mu_I(0)\rho_{eq}\mu_I(\tau_1)\mu_I(\tau_2+\tau_1)\right)
\end{aligned} \tag{2.21}$$

The four terms R_1 to R_4 correspond to *ket/ket/ket*, *bra/ket/bra*, *bra/bra/ket*, and *ket/bra/bra* interactions, respectively, based on how the transition dipole moment operator acts on the density matrix.

2.4.1 Diagrammatic Perturbation Theory

A useful method for understanding and keeping track of the R_α terms' contributions to a particular experiment are Feynman diagrams [79, 25, 80]. Each diagram represents a specific pathway that contributes to the signal, and by adding all the pathways together a complete nonlinear signal is generated. Each R_α has a particular diagram or set of diagrams associated with it, depending on the system. For clarity I will continue with the example of the two-level system, showing the contribution from each R_α.

In each Feynman diagram (see Figure 2-3) time increases from bottom to top. The relevant density matrix element for each pathway is listed in between the vertical lines. Each arrow represents a single light-matter interaction, causing a transition on either the bra or ket side of the density matrix. The strength of the transition is directly weighted by the transition dipole moment. After each interaction, the density matrix propagates via the appropriate time propagator. For all of the R_α diagrams, the system exists in a coherent superposition between the ground and excited state after the first interaction, a population after the second interaction, and a final coherence that emits the signal field after the third interaction. Using these principles, the

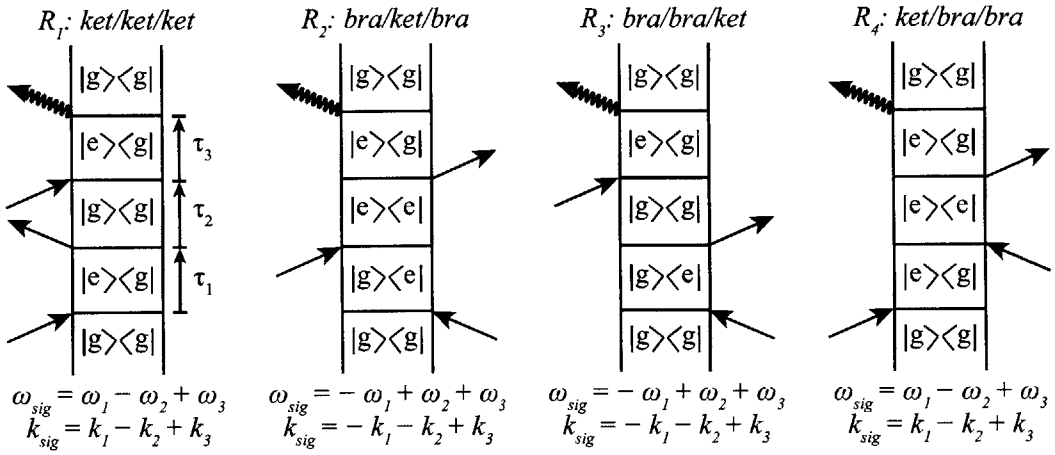

Figure 2-3: Pathways for the R_α contributions to third-order signal.

signals for R_2 and R_4 are

$$R_2 = |\mu_{eg}|^4 \exp(-i\omega_{eg}(\tau_3 - \tau_1) - \gamma_{eg}(\tau_1 + \tau_3) - \Gamma_e \tau_2)$$
$$R_4 = |\mu_{eg}|^4 \exp(-i\omega_{eg}(\tau_3 + \tau_1) - \gamma_{eg}(\tau_1 + \tau_3) - \Gamma_e \tau_2) \quad (2.22)$$

The main difference between R_2 and R_4 is the accumulation of phase during the initial and final coherence times. For R_2, the phase is reversed between the first and final times whereas for R_4 the phase accumulates further. Therefore, when $\tau_3 = \tau_1$ for R_2 (and R_3) there is a rephasing in that the phase is fully reversed. This is the basis for the photon echo, which will be further discussed in Section 2.5.2.

While the Feynman diagram approach is quite useful, it does not completely recover the dynamics and interactions in many systems. Many-body interactions in semiconductors, e.g. excitation-induced effects, Coulomb correlations, and exciton–free-carrier scattering, lead to nonlinear signals and yet are not captured by the Feynman diagrams approach because Feynman diagrams specifically deals with eigenstates of the material Hamiltonian [84, 85, 86, 87, 88, 89, 90]. Theoretical and experimental methods to identify and quantify these effects are discussed in further detail in Chapter 8.

2.4.2 Phase-Matching

When applying the additional action of the electric fields to the response function to generate the polarization, the wavevectors of the electric fields add and subtract depending on if the light-matter interaction was on the bra or ket side in the Feynman diagram. The generated signal wavevectors, k_{sig}, are listed at the bottom of Figure 2-3 for each R_α. Based on the phase-matching condition $\Delta k = 0$, it is clear that R_1 and R_4 co-propagate and that R_2 and R_3 co-propagate. However, each pair of contributions propagates in a unique direction. The first two signals are termed non-rephasing while the last two are rephasing or photon echo signals. These signals and several others are discussed in the next section.

2.5 Nonlinear Techniques

The experiments described in later chapters in this thesis take advantage of several nonlinear spectroscopy techniques that have been utilized and expanded upon for many years. Those first described are experiments designed to examine population dynamics [91, 82, 92]. The next technique is the photon echo, specifically aimed at disentangling coherence and dephasing dynamics [93, 82, 32, 94]. Two-quantum experiments are described next, specifically looking for correlations and interactions between excitations. Finally I describe multi-dimensional spectroscopy, an extension of all the previous methods that disentangles dynamics and correlations by spreading the spectral information into multiple dimensions.

2.5.1 Pump-Probe and Transient Grating

Pump-probe or transient absorption spectroscopy is a widespread technique used for monitoring the dynamics of excited states in many systems. A pump pulse excites the system and the change in absorption over time is monitored with a time-delayed probe pulse. While transient absorption can be described classically in terms of the third-order polarization and kinetics, the Feynman pathways approach allows for

straightforward interpretation and calculation of the spectral changes and dynamics. The geometry of a pump-probe experiment is shown in Figure 2-4(a). The pump pulse interacts twice with the system, creating excited state population. After a time delay the probe interrogates the state of the system. The phase-matching condition requires the third-order signal to co-propagate with the probe pulse. The interference between the signal and probe is the reason the probe sees increased absorption or transmission. However, transient absorption experiments only monitor the imaginary part of the response: only changes in absorption are detected by the experiment.

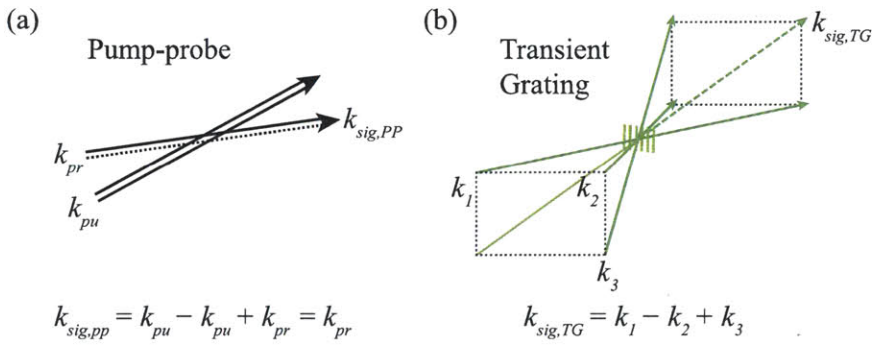

Figure 2-4: Phase-matching conditions for third-order spectroscopy. (a) Phase-matching geometry for pump-probe spectroscopy. (b) BOXCARS phase-matching geometry for transient grating.

The transient grating is a natural extension of transient absorption. Two different pulses with different wavevectors k_1 and k_2 are time-coincident on a sample, interfering in a periodic fashion (Figure 2-4(b)). The interference pattern creates a periodic change in the index of refraction with spacing $d = \lambda/2\sin(\theta/2)$, potentially in both the real and imaginary components. A third pulse with wavevector k_3 is focused to the same grating and upon seeing a periodically varying index of refraction diffracts into the phase-matched direction $k_{sig,TG} = k_1 - k_2 + k_3$. If the grating contains both real and imaginary components then the signal will have both real and imaginary parts. The imaginary part is exactly the same as in transient absorption. However, the real part contains information pertaining to non-resonant effects, e.g. coherent acoustic waves, thermal heating, and the dispersion associated with the absorption peak (see Figure 2-1).

The transient grating technique is also highly sensitive to transport [95, 91, 96, 97, 98]. The probe diffraction efficiency depends on the depth of the grating ΔN, i.e. the contrast between the peaks and nulls of the grating. Diffusion of e.g. acoustic waves or excitons will lower the contrast in tandem with the decay of the excitation due to its finite lifetime. A simple model for the transient grating decay uses the one-dimensional diffusion equation

$$\frac{\partial N(x,t)}{\partial t} = D\frac{\partial^2 N(x,t)}{\partial x^2} - \Gamma N(x,t)$$
$$N(x,t) = e^{-\Gamma t}[1 + \exp(-\Delta^2 Dt)\cos(\Delta x)]/2. \tag{2.23}$$

where D is the diffusion constant, Γ is the excitation decay rate, and the grating wavevector $\Delta = \frac{2\pi}{d}$. The grating depth and decay rate are

$$\Delta N = N(x=0,t) - N(d/2,t) = \exp(-Kt/2)$$
$$K = 2(\Delta^2 D + \Gamma). \tag{2.24}$$

A series of experiments with varied angles between the excitation beams changes the rate of decay due to diffusion while leaving the decay due to the finite lifetime unchanged, allowing separation of the diffusive and lifetime effects on the grating signal.

Both transient absorption and transient grating typically monitor excited-state dynamics. However, there are a couple of disadvantages. The first is that all of the information content from R_1 through R_4 is contained in the signal; both rephasing and nonrephasing signals contribute. This means it is impossible to isolate dephasing dynamics in these experiments. The second disadvantage is the trade off between frequency selectivity in the pump and time resolution. In order to know exactly which excitation was pumped, a narrowband frequency-selective pump must be used. However, a frequency-selective narrowband spectrum leads to a long pulse in the time

domain, leading to a minimum time that can be resolved in the experiment. This deficiency is overcome by multi-dimensional spectroscopy as described in Section 2.5.4.

2.5.2 Photon Echo Spectroscopy

Photon echo spectroscopy is another extension of the previously mentioned techniques, performed by using the BOXCARS geometry and changing the time-ordering of the pulses in the transient grating experiment [32, 94]. When the pulse with the negative wavevector contribution (the conjugate pulse) arrives first, as discussed previously for R_2 and R_3, a rephasing occurs when the final coherence time is equal to the initial coherence time. This is because of the phase reversal during those two time periods. This is extremely useful when significant inhomogeneous broadening affects the system. For the two-level system, setting $\tau_2 = 0$ in R_2 and R_3 and including appropriate lineshape functions for homogeneous and inhomogeneous broadening [25] in the derivation for the nonlinear polarization leads to

$$R^{(3)} = |\mu_{eg}|^4 \exp(-i\langle\omega_{eg}\rangle(\tau_3 - \tau_1) - \gamma_{eg}(\tau_1 + \tau_3) - (\tau_3 - \tau_1)^2\Delta^2/2), \tag{2.25}$$

where $\langle\omega_{eg}\rangle$ is the average frequency and Δ is the width of the frequency distribution. From Equation 2.25 it is clear that for $\tau_3 = \tau_1$ the only decay remaining is due to the homogeneous dephasing, γ_{eg}. The standard experimental setup uses an integrating detector, e.g. photodiode, which for highly inhomogeneous systems ($\Delta \gg \gamma_{eg}$ leads to

$$I_{sig}(\tau_1) \propto e^{-4\gamma_{eg}\tau_1}. \tag{2.26}$$

The inhomogeneous component no longer contributes to the signal decay due to the rephasing. The factor of four reflects the homogenous dephasing over two time periods and the fact that the integrating detector doubles the decay rate.

2.5.3 Two-Quantum Spectroscopy

Two-quantum (2Q) experiments involve the same geometry and phase-matching as an echo but the pulse time-ordering is switched: the conjugate pulse is the *third* pulse in the sequence. Thus, 2Q experiments are also referred to as S3 experiments. Similarly, photon echoes are S1 experiments and non-rephasing are S2. Because the S3 is specific to multiple excitations and their interactions, the simple two-level system example produces identically zero signal for S3. A higher-lying excited state accessible from the first excited state must exist. Vibrational overtones are directly probed in S3 IR measurements and anharmonicity is readily apparent [99]. In molecules the excitation of both electrons from the HOMO to the LUMO leads to S3 signals [100, 101, 102, 103], whereas in excitonic systems it is the excitation of multiple excitons across multiple atoms in inorganic semiconductors [104, 105, 106, 107, 108, 109, 110, 111] or molecules in organic semiconductors [35, 112, 70]. In gas phase atoms, S3 signals can be generated due to excited atoms producing a local electric field (weak dipole-dipole interaction) that influences the neighboring atoms, coupling the excitations together to form a correlated doubly-excited state [113].

In a 2Q experiment, the first two pulses create a coherence between the doubly-excited state and the ground state, giving insight to its energy and lifetime. For example, the dephasing time is directly related to the correlation time for local field effects. The energy of the doubly-excited state reports on the binding or anti-binding between quasi-particles, as occurs when hydrogen-like excitons bind to form biexcitons.

2.5.4 Multi-Dimensional Spectroscopy

The third-order polarization contains information about many processes occurring in the systems across three different time periods. To gain maximum knowledge of these processes would require three-dimensional spectroscopy. While that has been accomplished for some systems and under certain conditions [114, 115, 107, 116, 117], three-dimensional spectroscopy is somewhat impractical and time consuming due to

technical limitations. However, many research groups are adopting the more tractable two-dimensional spectroscopy (2DS) [118, 29, 119, 120]. This typically involves setting one of the time delays in the third-order polarization to zero. The experiments in this thesis are comprised almost entirely of 2DS experiments.

2DS offers many unique advantages compared to traditional one-dimensional spectroscopies like linear absorption, pump-probe and transient grating, and 1D photon echoes. Spreading the information content of the polarization out over multiple dimensions disentangles different types of dephasing, coupling and interactions, and dynamics. This is illustrated in Figure 2-5 for the photon echo. On the left is the case with $\Delta = 0$, showing uniform homogeneous damping. Δ increases moving left to right, showing that with large inhomogeneous broadening, rephasing occurs along $\tau_3 = \tau_1$ diagonal. The decay along the diagonal is determined primarily by homogeneous dephasing (and is the same magnitude as that in the left panel) whereas the anti-diagonal decay is primarily governed by inhomogeneous dephasing.

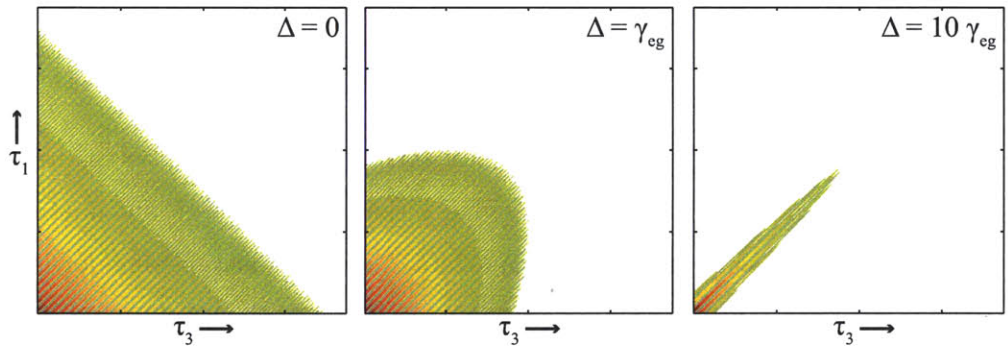

Figure 2-5: Time-domain photon echo. Going from left to right displays signals with increasing inhomogeneity (Δ), showing the interplay between inhomogeneous and homogeneous dephasing.

A double Fourier transform of the time-domain photon echo in Figure 2-5 separates the inhomogeneous and homogeneous lineshapes into two dimensions (Figure 2-6), clarifying the quantity of each present in the system. The anti-diagonal linewidth is related to the amount of homogeneous dephasing and for inhomogeneous systems the diagonal lineshape reflects the degree of inhomogeneity.

Even though the 2D photon echo separates the homogeneous and inhomogeneous

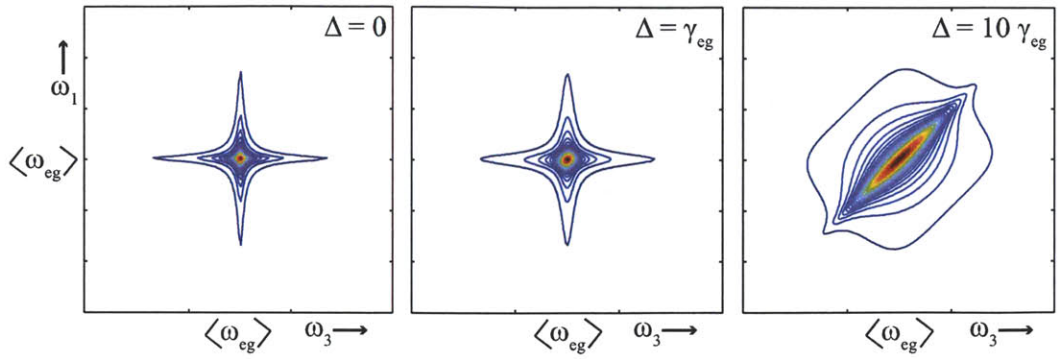

Figure 2-6: Frequency-domain two-dimensional photon echo. Going from left to right displays signals with increasing inhomogeneity (Δ), showing the increasing broadening along the diagonal frequency while maintaining a narrow linewidth along the anti-diagonal.

lineshapes, the imaginary and real parts of the echo signal do not correspond to the absorptive and dispersive components, respectively. Pump-probes and transient grating signals are directly related to absorptive and dispersive lineshapes because, as mentioned in Section 2.5.1, they contain all four Feynman diagrams $R1 - R4$. When extracting the susceptibility and the absorption spectrum from $P^{(1)}(t)$ a full Fourier transform is performed. For the photon echo and non-rephasing signals only a half-sided Fourier transform is performed with respect to τ_1. This is due to restrictions imposed by pulse-ordering: in the echo the conjugate pulse comes first, in the non-rephasing experiment the conjugate pulse comes second. This leads to phase twist in the real and imaginary components of S1 and S2 signals [121, 122]. Adding the rephasing and non-rephasing spectra together forms correlation spectra with no phase twist and purely absorptive and dispersive components. This is demonstrated in Figure **??** for the two-level system example from previous sections. The left and middle panels show the imaginary components of the rephasing and non-rephasing signals. In a pump-probe experiment only stimulated emission and ground state bleaching terms appear, leading to a purely negative signal. The rephasing and non-rephasing signals have both positive and negative parts, whereas the correlation spectrum is purely negative.

Another unique advantage of 2DS is its direct sensitivity to coupling among ex-

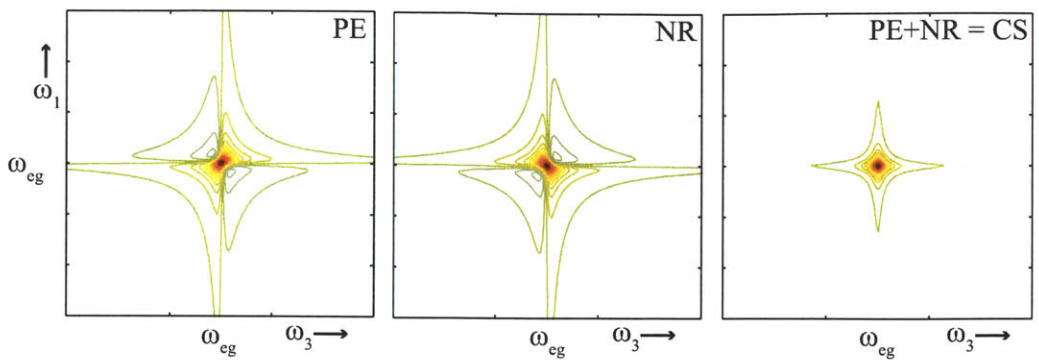

Figure 2-7: Imaginary components of 2D spectra. Addition of photon echo (PE, left) and non-rephasing (NR, middle) 2D spectra lead to correlation spectra (CS, right) with purely absorptive lineshapes in the imaginary component.

citations. When a broadband laser pulse excites the sample, coupled transitions will cause additional signals compared to the uncoupled case in the 2DS spectrum. The physical mechanism generating the new signals involves polarizations coupling to one another. A light-matter interaction involving one transition leads to a polarization. If the excited transition is coupled to a second transition, the excited polarization acts as a source for a polarization involving the second transition. This is illustrated by the Feynman diagrams in Figure 2-8(b). The signals caused by coupling manifest in a 2DS spectrum as crosspeaks (Figure 2-8(c)), indicating that excitation at one frequency leads to emission at another, even with $\tau_2 = 0$. This is due to delocalizaiton of the wavefunction across the two states.

Scanning τ_2 allows for population and coherent dynamics to occur, same as in a pump-probe or transient grating measurement. However, the high frequency resolution in the absorption and emission dimensions is maintained, allowing for the full recovery of coherent and energy transfer dynamics. For example, the crosspeaks in Figure 2-8(c) will oscillate because the system wavefunction is in a coherent superposition between states $|e\rangle$ and $|f\rangle$ during τ_2. Energy transfer or dynamic Stokes shifts will manifest as increasing amplitude in the crosspeak with high energy absorption and low energy emission. In this way it is possible to see directly energy transfer processes [118, 29, 20].

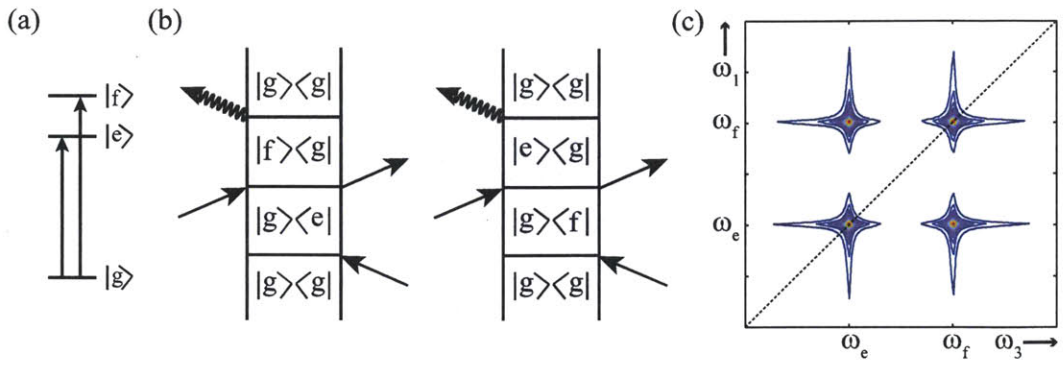

Figure 2-8: Three-level system 2DS. (a) "V" system states. (b) New Feynman diagrams for $\tau_2 = 0$ that arise due to coupling between states $|e\rangle$ and $|f\rangle$. (c) 2D photon echo spectrum with diagonal peaks and crosspeaks.

2.6 Detection Methodology for Nonlinear Experiments

There are many detection techniques for nonlinear spectroscopy. Photodiodes and photomultiplier tubes are inherently single-point detectors whereas spectrometers are one dimensional. This means that using a spectrometer as the detector automatically gives knowledge of the entire emission spectrum (or timetrace if Fourier transformed); this is the method of choice for transient absorption. For the τ_1 and τ_2 time delays typically motorized translation stages are used. The major drawback for this technique is the phase jitter associated with sending different beams through different optical paths. Air currents and mount and optic vibrations cause changes to the optical pathlength and therefore the optical phase. For the infrared and longer wavelengths this is a surmountable problem because the wavelength is much larger than the pathlength changes, translating into small changes in phase. However, for electronic spectroscopy in the $400 - 700$ nm region, these small pathlength changes cause significant phase changes. This scrambles the phase of the emitted signal and only amplitude information is retained. This is still useful for determining an overall dephasing time for a transition using a 1D echo, for example; however the drawback is

that the energies of the initially excited states are lost because the signal does not oscillate. Even if the phase is stable, a phase-sensitive detection scheme is required, otherwise the amplitude is again the only information retained.

There are several methods to retain phase stability and enable phase-sensitive detection for coherent optical spectroscopy experiments. Active phase stabilization uses interferometric loops with HeNe tracer beams for each loop to keep track of the phase [123]. Fluorescence-detected 2DS [124], 2D nanoscopy [125], and single shot 2DS [126, 127, 128] have recently been demonstrated. Passive phase stabilization is perhaps the easiest method to implement. Many research groups successfully use pairs of glass wedges to introduce time delays, allowing all the laser beams to propagate the same optical path and retain a stable phase relationship [129, 130]. The method used in this thesis and in several other research groups is pulse shaping [131, 132, 133, 134, 135, 136]. All the beams have a common optical path, and femtosecond spatiotemporal pulse shaping is used to control the optical phases, time delays, and other pulse parameters.

In the next sections I briefly describe the detection technique used throughout this thesis and an experimental advantage offered by pulse shaping that significantly reduces experimental acquisition time.

2.6.1 Heterodyne Detection and Spectral Interferometry

Any time-integrating light detection device detects the intensity of the light and loses the phase information retained in the light field. For example, a spectrometer detects the intensity I_{det} of the emitted signal field from a nonlinear interaction as a function of frequency,

$$I_{det} \propto |E_{sig}(\omega)|^2 \propto |iP^{(3)}(\omega)|^2. \tag{2.27}$$

Even though intensity is insensitive to absolute phase, it is sensitive to phase differences between interfering waves. If two electric fields are simultaneously detected in the spectrometer, the phase difference, $\Delta\varphi(\omega) = \varphi_{sig}(\omega) - \varphi_{ref}(\omega)$, manifests in the

interference term between the two waves,

$$I_{det} \propto |E_{sig}(\omega) + E_{ref}(\omega)e^{i\Delta\varphi}|^2 \propto I_{sig} + I_{ref} + 2\sqrt{I_{sig}I_{ref}}\cos(\Delta\varphi). \tag{2.28}$$

Optical heterodyne detection refers to the use of a reference beam spatially overlapped with the signal beam to cause phase-sensitive interference in the detector (spectromter). To retrieve the signal phase from the interference, and simultaneously remove the homodyne components, we delay the reference beam a small amount, leading to interference fringes in the spectrum. This is known as spectral interferometry, a well known technique for extracting the signal phase using a well-characterized reference [137, 138, 139]. With a time delay τ_{ref} the reference phase becomes $\varphi_{ref}(\omega) = \omega\tau_{ref}$ and Equation 2.28 becomes

$$I_{det} \propto I_{sig} + I_{ref} + 2\sqrt{I_{sig}I_{ref}}\cos(\varphi_{sig} - \omega\tau_{ref}). \tag{2.29}$$

An inverse Fourier transform to the time domain and application of the Fourier Shift Theorem leads to

$$I_{det}(t) \propto I_{sig}(t) + I_{ref}(t) + I_{sr}(t - \tau_{ref}, \varphi_{sig}) + I_{sr}(t + \tau_{ref}, \varphi_{sig}). \tag{2.30}$$

I_{sr}, with contributions from both the signal and reference, is the interference term of interest. Applying a filter that isolates $I_{sr}(t - \tau_{ref}, \varphi_{sig})$, Fourier transforming back to the frequency domain, and dividing by the reference amplitude leads to

$$I_{filt}(\omega) \propto \sqrt{I_{sig}(\omega)}e^{-i\varphi_{sig}(\omega)}. \tag{2.31}$$

From Equation 2.31 it is clear that the nonlinear signal amplitude and phase are fully isolated.

2.6.2 Rotating Frame Detection

The final section of this Chapter describes an additional advantage of using pulse shaping. In Section 3.3.4 I explain that pulse shaping delays only the envelope of a pulse, not the user-defined carrier wave. The implications for this are that all of the experiments are performed in the rotating frame, meaning that any phase changes occurring during the experiment are always with respect to the carrier wave [121, 108]. If the phase of the carrier wave is stable then the experimental phase changes are slow and the oscillations are reduced by the frequency of the carrier wave. To see this more clearly we can calculate the linear polarization, Equations 2.13 and 2.16, with a pulse-shaper-delayed pulse, $E(t-\tau) = E_0\, a(t-\tau)e^{i\omega_c\tau}$,

$$P^{(1)}(t) \propto E_0|\mu_{eg}|^2 \int_0^\infty a(t-\tau)e^{i\omega_c\tau}e^{-i\omega_{eg}\tau-\gamma_{eg}\tau} + c.c. \tag{2.32}$$

Due to the extra factor $e^{i\omega_c\tau}$ from the electric field, the oscillations in $P^{(1)}$ are reduced in frequency to the difference $\omega_{eg} - \omega_c$. With pulse shaping we are able to control the Nyquist frequency required to fully capture the dynamics, and therefore significantly reduce the number of time steps taken in each experiment and perform each 2DS experiment in a fraction of the time.

Chapter 3

Experimental Setup

This chapter serves as a general overview of the experimental apparatus, starting with the ultrafast laser amplifier source and ending with the calibrations required for the complete multi-dimensional spectrometer. For further details see the theses of Joshua Vaughan [140], Katherine Stone [141] and Daniel Turner [142], and the comprehensive review by Turner et al. [136]. The final section describes implementation of a transient grating setup for measuring transport on very short length scales.

3.1 Ultrafast laser system

The majority of the experiments described in this thesis were performed using the Coherent Libra titanium sapphire (Ti:Sa) regenerative amplifier system. The output of the Libra was a 3.5 Watt, 10 kHz pulse train of approximately 70 fs pulses centered at 800 nm. For a subset of experiments performed in Chapter 5 and Chapter 8 a KMLabs Ti:Sa oscillator was used. The oscillator output was a 92.5 MHz pulse train centered near 800 nm.

3.2 Noncollinear Optical Parametric Amplifier

In order to perform experiments on a diverse range of nanostructured materials a readily tunable ultrafast laser source was required. I designed and built a Noncollinear

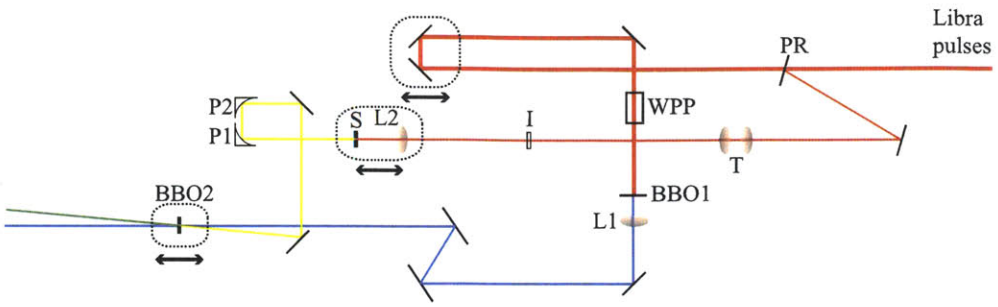

Figure 3-1: The NOPA optical design. The Libra output passes through a partial reflector (PR), reflecting 5% of the light to the seed arm. The non-reflected pulses generate the blue pump pulses in a BBO crystal (BBO1) after retro-reflecting along a variable translation stage and passing through a waveplate-polarizer (WPP) to control the power. Lens L1 focuses the blue pump to the mixing BBO (BBO2). The seed arm is enlarged by a telescope (T) and passes through a variable iris (I) for attenuation. Lens L2 focuses the seed to a 1 mm thick sapphire plate (S) generating a white light continuum. Two off-axis parabolic reflectors (P1, focal length 10 cm; P2, focal length 30 cm) collect and focus the seed to BBO2 where parametric amplification occurs.

Optical Parametric Amplifier (NOPA) that utilizes several nonlinear optical processes to generate pulses from 500 nm to 750 nm with varying pulse widths [143, 144, 145, 146, 147, 148, 149]. The pump laser source is the Coherent Libra amplifier. Three nonlinear processes occur to generate the desired output laser pulses (Figure 3-1). First, the Libra pulse is split by a 95/5 partial reflector into a pump arm and a seed arm. The pump arm travels on a translation stage, allowing timing control between the pump and seed pulses. The pump beam then enters a nonlinear crystal Beta Barium Borate (BBO) optimized to generate the second harmonic of the Libra pulse at 400 nm. The 400 nm pump light is then focused via a 40 cm focal length lens to a second BBO crystal optimized for parametric amplification. The seed arm first passes through a telescope increasing the size. An iris is used to control the intensity and spatial distribution of the seed beam. The seed is then focused by a 3 cm focal length lens into a 1 mm sapphire plate, producing a white light continuum. The continuum is collected, colllimated, and then refocused by two off-axis parabolic mirrors to the BBO for parametric amplification.

The amplified NOPA output beam is sent into a fused silica prism compressor followed by focusing through a $50-70$ micron spatial filter to produce near transform

limited, TEM_{00} beams. The parametric amplification process produces nearly 150 nm of bandwidth, which generally greatly exceeds that desired for our experiments. A slit consisting of two razor blades inserted into the prism compressor filters the spectral content, both center wavelength and bandwidth. We typically use $20-30$ fs pulses.

The final NOPA beam is sent first to a spatial beam shaper to generate the desired beam geometry. Then the beams are sent to a two-dimensional pulse shaper for wavevector shaping, controlling both the spectral amplitude and phase of each beam. After careful calibration of each step the beams are sent to the experiment.

3.3 Pulse Shaping

After passing through the prism compressor, the NOPA pulses are sent to the pulse shaping setup. The unique characteristics of two-dimensional femtosecond pulse shaping offer several advantages [150, 151, 152, 153, 154, 140]. Common path optics offer phase stabilization because air currents and vibrations affect the beams essentially concurrently and equally [131, 129, 130]. Additionally, phase cycling techniques increase the sensitivity to particular pulse sequences (along with phase-matching conditions) to increase signal to noise and subtract spurious signals [131, 140, 141, 142]. While all pulse shaping techniques enable coherent control experiments [155, 156, 157, 158, 159, 160, 161], two-dimensional pulse shaping in particular enables phase *and* amplitude shaping experiments not possible with other types of traditional nonlinear spectroscopy or one-dimensional pulse shaping setups. Finally, pulse shaping enables rotating frame detection, reducing the stringent Nyquist-limit requirements for coherent femtosecond spectroscopy [121, 162, 106, 141, 142, 136].

3.3.1 Beam Pattern Generation

The Beam Shaping component of the multi-dimensional spectrometer consists of two parts, a telescope and a transmissive diffractive optic (phase mask) at the focal plane (Figure 3-2(a)). For four-wave mixing experiments, we typically use a pattern of two

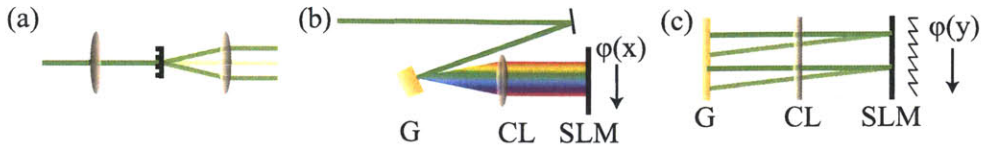

Figure 3-2: Optical designs for pulse shaping. (a) Beam Shaper consisting of a phase mask at the focal plane of a 1:1 telescope demonstrating one-dimensional diffraction. (b) Temporal Pulse Shaper with a top-down view of the grating (G), cylindrical lens (CL), and spatial light modulator (SLM) with a frequency-dependent phase $\phi(x)$. (c) Wavevector Shaping with a side view of G, CL, and SLM with an example diffraction pattern ($\phi(y)$) for diffraction-based pulse shaping.

perpendicular gratings optimized for first-order diffraction, generating the ubiquitous BOXCARS geometry. A significant advantage offered by imaging the phase mask to the sample is that the beams automatically have phase-matched wavevectors, including the reference local oscillator beam. This leads to reconstruction of the initial diffraction pattern and greatly enhanced signal when compared to crossing the beams using steering mirrors [163, 164, 165]. This also reduces the complexity of the experiment as no additional steering mirrors are required for alignment and a common path for all the beams is automatically implemented.

3.3.2 Temporal Pulse Shaping

The beams generated in the Beam Shaper are imaged to the temporal pulse shaping setup. The critical components in the temporal pulse shaper are shown in Figure 3-2(b) with a single beam. Diffraction off a grating, typically around 1000 lines/mm and blazed for the desired wavelength, separates the wavelengths making up the ultrafast pulse. A cylindrical lens focuses the individual frequencies to a horizontal stripe across the active pulse shaping element, the Spatial Light Modulator (SLM).

We utilize two-dimensional phase-only SLMs. In the horizontal direction frequency-dependent phase patterns ($\phi(x)$ or alternatively $\phi(\omega)$) are applied to the input optical field, $E_{in}(\omega)$, which alter the time-dependent electric field of the output pulse, $E_{out}(t)$, according to Fourier Transforms,

$$E_{out}(t) \propto \int_{-\infty}^{\infty} E_{in}(\omega) e^{i(\omega t + \phi(\omega))}\, d\omega. \tag{3.1}$$

For example, a linear change in phase with frequency, $\phi(\omega) = \omega\tau$, leads to a time delay,

$$E_{out}(t) \propto \int_{-\infty}^{\infty} E_{in}(\omega) e^{i(\omega t + \omega\tau)}\, d\omega = \int_{-\infty}^{\infty} E_{in}(\omega) e^{i(\omega(t+\tau))}\, d\omega = E_{in}(t+\tau). \tag{3.2}$$

There are three imperfections in temporal pulse shaping primarily responsible for reducing the fidelity of the waveforms produced. The finite spectral resolution, $\delta\omega$, of the grating and cylindrical lens resulting from the diffraction-limited focus leads to a gaussian time window, $exp(-\pi^2\delta\omega^2 t^2)$, reducing the intensity of the generated waveform as a time delay is applied. In addition, the pixelated nature of the SLM, which can be represented by the top-hot function

$$T(x) = \begin{cases} 1 & 0 \leq x \leq 1 \\ 0 & x < 0, x > 1 \end{cases}, \tag{3.3}$$

leads to a sinc window in the time domain, $sinc(\pi\Delta\omega t)$, with $\Delta\omega$ the bandwidth of a single pixel. Together these two effects create an effective time-window for possible delays on the pulses,

$$window \propto exp(-\pi^2\delta\omega^2 t^2) sinc(\pi\Delta\omega t). \tag{3.4}$$

The largest effect caused by the time-window is additional decrease in signal due to the laser pulse intensity decreasing with time delay. However, in our temporal pulse shaping setup the time-window typically has a $1/e$ time of several picoseconds whereas in our samples the relevant timescales of interest (dephasing and energy transfer dynamics) are on the order of a few hundred femtoseconds to one or two picoseconds at low temperature, mitigating the effect of the time-window.

The third negative effect caused by temporal pulse shaping with SLMs is the fact

that SLMs cannot change the phase arbitrarily but have a maximum phase change typically not much larger than 2π. To get around this limitation we take advantage of the fact that an addition of 2π radians does not change the pulse characteristics. Therefore, we wrap the applied phase modulo 2π. However, this wrapping is imperfect in SLMs, leading to a periodic, frequency-dependent imperfection in the phase profile of the pulse. This leads to a periodic series of pulses in the time domain whose spacing depends on the phase-wrapping period in the frequency domain. We avoid these unwanted modulator replica pulses via diffraction-based pulse shaping, as explained in the following sections.

3.3.3 Wavevector Shaping

Section 3.3.2 described waveforms created through spectral phase modulations. While very powerful, this technique is limited in that the spectral amplitude of the pulse cannot be controlled. We take advantage of the two-dimensional nature of the SLMs to enable amplitude modulation for coherent control as well as to get rid of the modulator replica pulses. A diffraction pattern is applied in the vertical dimension of the SLM ($\phi(y)$ in Figure 3-2). A lens at the back focal plane of the SLM focuses the diffraction to series of spots where we isolate the first-order diffraction for use in the experiment. By controlling the efficiency of diffraction via the groove depth for different wavelengths we control the spectral content of the pulse in addition to the phase control in horizontal (temporal) direction. The desired shaped pulse diffracts into the first-order spot while the spurious modulator replica pulses all diffract into different diffraction orders because those orders contain by definition an additional spatial phase of 2π.

3.3.4 Diffraction-Based Pulse Shaping

The combination of femtosecond temporal pulse shaping and wavevector shaping, termed diffraction-based pulse shaping, gives unprecedented control over both the phase and amplitude of not only a single pulse but over multiple pulses simultane-

ously. The reconfigurable nature of the SLMs makes the pulse shaping setup useful for many types of experiments including multi-dimensional spectroscopy, transient grating, Raman spectroscopy, transient absorption, and many other nonlinear spectroscopies. Pulse shaping gives two additional advantages: the experiments are performed in the rotating frame (see Section 3.3.2) to increase data acquisition times; and we can implement phase cycling techniques to further enhance the sensitivity of the experiment to a specific generated signal.

Rotating Frame Detection

Rotating frame detection was described in Section 2.6.2. In this section I describe how pulse shaping enables this technique. Any phase pattern applied to a pulse is always in reference to a specific carrier frequency, ω_c, that is user-defined for each experiment. We define the phase at ω_c to be zero for any applied phase pattern. For the delay described in Section 3.3.2 this means the actual phase pattern we apply is $\phi(\omega) = (\omega - \omega_c)\tau$. According to Equation 3.1,

$$E_{out}(t) \propto E_{in}(t+\tau)e^{-i\omega_c\tau}. \tag{3.5}$$

If $E_{in}(\omega)$ has the form of an envelope and a carrier wave, $e(t)e^{i\omega_c t}$, then a pulse delayed via pulse shaping by a time τ will have the form,

$$E_{out}(t) \propto e(t+\tau)e^{i\omega_c t}. \tag{3.6}$$

Thus the envelope of the pulse is delayed while the carrier wave is not, allowing for rotating frame detection. We typically choose ω_c within the pulse bandwidth to allow calibration.

Phase Cycling

Incoherent light scattering can lead to spurious electric fields from the excitation beams interfering with the nonlinear signal. For example, using spectral interferometry a spectrometer could detect the nonlinear signal, proportional to $iP^{(3)}$, as well

as electric fields from the scattered excitation beams,

$$I_{det} \propto |iP^{(3)} + E_1 + E_2 + E_3 + E_{ref} + c.c.|^2. \tag{3.7}$$

Pulse shaping enables phase cycling, a process by which the spurious interferences are removed from the collected spectra via cycling the phases of the beams generating the nonlinear signal [121, 131, 133, 136]. For the $\chi^{(3)}$ experiments in this thesis with the phase-matching condition $k_{sig} = -k_1 + k_2 + k_3$, the nonlinear polarization depends on the phases of the input beams in a specific way,

$$P^{(3)} \approx \chi^{(3)} E_1^* E_2 E_3 = \chi^{(3)} a_1^* a_2 a_3 e^{-i((-k_1+k_2+k_3)\cdot r-(-\omega_1+\omega_2+\omega_3)t)} e^{-i(-\varphi_1+\varphi_2+\varphi_3)}. \tag{3.8}$$

Only the third-order polarization has this particular phase dependence. Therefore, cycling the phase of the input beams in a particular order and adding the generated signals subtracts the spurious interferences while simultaneously enhancing the nonlinear signal. For the phase dependence in Equation 3.8, the appropriate phase cycling scheme is an eight-step procedure,

$$\begin{aligned} I_{sig} =& I(\phi_1, \phi_2, \phi_3) \\ & - I(\phi_1 + \pi, \phi_2, \phi_3) - I(\phi_1, \phi_2 + \pi, \phi_3) - I(\phi_1, \phi_2, \phi_3 + \pi) \\ & + I(\phi_1 + \pi, \phi_2 + \pi, \phi_3) + I(\phi_1 + \pi, \phi_2, \phi_3 + \pi) + I(\phi_1, \phi_2 + \pi, \phi_3 + \pi) \\ & - I(\phi_1 + \pi, \phi_2 + \pi, \phi_3 + \pi) \\ =& 16|iP^{(3)} + E_{ref} + c.c.|^2 \end{aligned} \tag{3.9}$$

3.4 Pulse Shaping Calibrations

The multi-dimensional spectrometer consists of all the previously described components, from the Libra amplifier to pulse shaping (Figure 3-3). First, the Libra amplifier beam is sent to the NOPA to generate tunable ultrafast laser pulses. This single

beam is sent to the beam shaper, generating several beams in a phase-matched geometry. This geometry is imaged through the pulse shaper where well-defined temporal delays, chirps, optical phases and spectral amplitudes are applied to the pulses to perform the experiment. The pulse shaper output, consisting of several shaped beams, is focused to the sample where nonlinear signal is generated in a phase-matched direction. The signal is sent to an Acton 2300i imaging spectrometer with a PIXIS400 CCD camera as the detector.

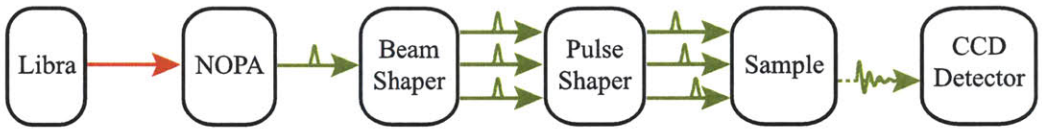

Figure 3-3: Multi-dimensional spectrometer sequences from pulse generation, pulse shaping, signal generation, to signal detection.

Each component of the multi-dimensional spectrometer must be properly aligned and calibrated for successful experiments. The Libra typically requires little to no daily maintenance as its output characteristics are robust. The NOPA requires daily tuning to ensure the proper wavelength, pulse compression, and spatial mode. The Beam Shaper only requires alignment or tuning when changing the beam pattern and phase mask. The pulse shaper requires four calibrations outlined below.

3.4.1 Phase to Grayscale

The first calibration, phase to grayscale, determines how the SLM controls the phase of incoming light. The calibration procedure is as follows: a single beam of the desired frequency hits a phase mask, generating two replicas. The replicas are focused to the left and right sides of the SLM, reflect off the SLM, recombine through the phase mask and are focused onto a photodiode. One half of the SLM is scanned through its voltage levels for one beam, thereby changing its overall phase and causing interference between the two beams aligned in the photodiode. The sinusoidal interference signal is converted to a phase difference, giving a relationship between applied voltage (grayscale) and applied phase. This relationship is inverted to give the grayscale as

a function of phase to allow user-defined phases to be applied.

This calibration is only required when significantly changing wavelengths. For the limited bandwidth laser pulses we use, a single phase to grayscale is sufficient. For much broader bandwidth applications a different phase to grayscale could be applied for each frequency.

3.4.2 Pixel to Wavelength

The second calibration sets the relationship between SLM pixel number and wavelength in order to apply frequency-dependent phases such as time delays and temporal chirps. To perform this calibration, the spectrum of one of the diffracted beams is imaged in the spectrometer and a three-pixel-wide vertical stripe is illuminated and scanned horizontally across the SLM. The narrowband spectrum in the spectrometer corresponds directly to the specific pixels illuminated, allowing generation of a pixel-to-wavelength calibration curve.

3.4.3 Temporal Distortions

The third calibration performed corrects the different temporal chirps and time delays acquired by different beams from imperfect imaging in the pulse shaping setup due to spherical and chromatic aberrations from the cylindrical lens. First, a single beam is sent to a Frequency Resolved Optical Gating (FROG) [166, 167] setup and the cylindrical lens–SLM distance and grating angle are tuned to compress the pulse to near transform limited. Next, all the beams generated by the Beam Shaper are focused into a 30 micron BBO crystal at the sample position. Cross correlations are taken between the transform limited pulse and the other pulses, and the pulse shaper is used to remove the temporal distortions on all the beams to make them all transform limited. The FROG-corrected pulse also serves as a timing reference to ensure all the pulses for the experiment are initially time coincident.

3.4.4 Carrier Frequency

The final calibration determines the carrier frequency, $\omega_c = 2\pi\nu_c$, of each beam. We use a double-pulse phase pattern and spectral interferometry to determine the frequency-dependent phase of each beam. Varying the delay causes the phases to vary except at the carrier frequency, allowing us to pinpoint with high accuracy the carrier frequency. We send each beam independently into the Acton spectrometer and apply a $cos(2\pi(\nu - \nu_c)t_{delay})$ phase pattern to generate a double pulse.

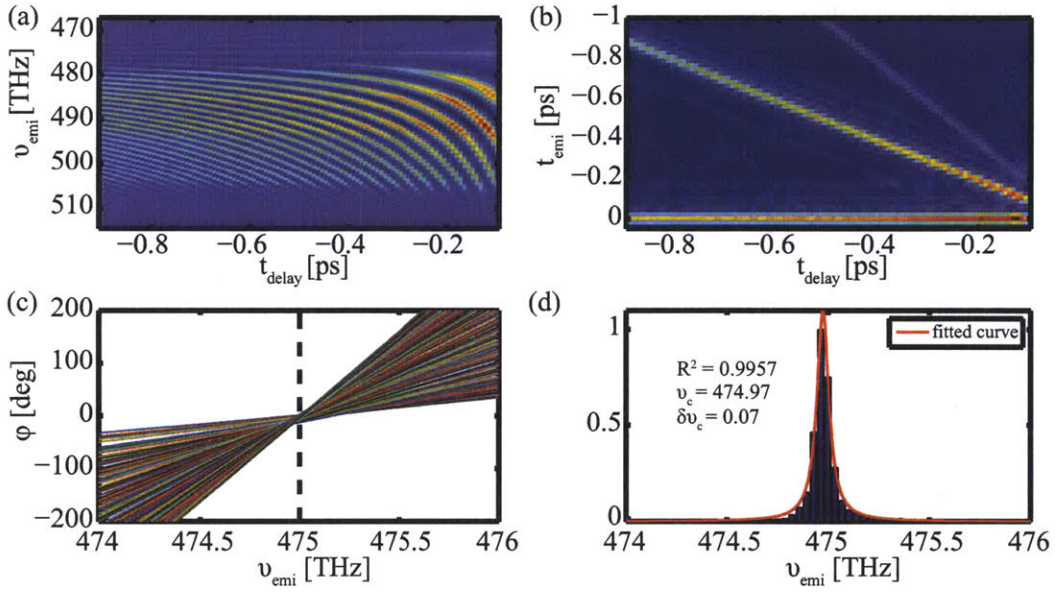

Figure 3-4: Steps in carrier frequency calibration procedure.

An example is shown in Figure 3-4 with $\nu_c = 475$ THz. The delay between the pulses, t_{delay}, is scanned, generating interference patterns in the frequency domain with varying periodicity (Figure 3-4(a)). Fourier transformation of the interference patterns leads to signals in the time-time domain, including the $t_{emi} = 0$, $t_{emi} = t_{delay}$, and spurious higher-order signals caused by imperfect pulse shaping (Figure 3-4(b)). Using spectral interferometry as described in Section 2.6.1 we extract the frequency-dependent phase ϕ for each t_{delay} (Figure 3-4(c)). The point where the phases cross is the carrier frequency. We then compose a histogram of the frequencies with the minimum distance between phases for different delays (Figure 3-4(d)) and fit the

distribution to find the center frequency and distribution width.

3.5 Transient Grating Spectroscopy

This section describes the experimental setup for transient grating spectroscopy. The NOPA output, after compression, is split into two arms by a 50/50 beamsplitter to create the pump and probe beams. The pump travels through a 25 cm translation stage allowing up to $\sim$ 1 ns delays. The beams are combined to a common path at different heights. They are focused by a 15 cm lens to a phase mask to generate the BOXCARS geometry [165, 164]. The first-order diffraction spots are collected by a 2 cm aspheric lens. One probe beam passes through an $ND = 1$ filter while the other probe beam passes through a blank ND filter to compensate for the delay. The four beams are focused by a second 2 cm aspheric lens to the sample where $\chi^{(3)}$ signal is generated. After collection by a third 2 cm aspheric lens the pump beams are blocked and the probe beams are sent to two matched photodiodes.

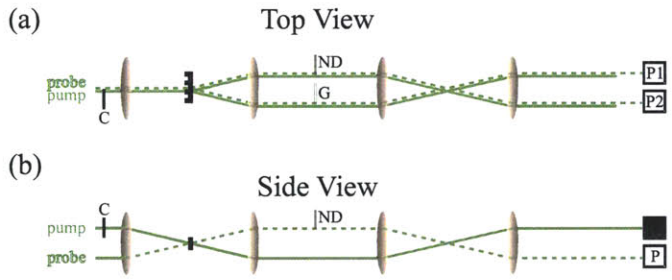

Figure 3-5: Transient grating experiment. (a) Top view of setup. Pump (chopped) and probe are focused by 15 cm lens to phase mask. The diffraction is collected by a 2 cm aspheric lens. An $ND = 1$ filter is placed in the arm of one probe beam with a blank filter G for compensation in the other probe beam. A second 2 cm aspheric lens focuses to the sample with collection by a third aspheric lens. The pump beams are blocked and the probe beams are sent to a pair of matched photodiodes for balanced detection. (b) Side view of setup.

Using these imaging optics the smallest grating spacing successfully imaged to the sample was 600 nm, nearing the diffraction limit for 600 nm light. Each probe beam undergoes diffraction and acts as the local oscillator reference for the diffraction from the other probe beam [168, 169, 170] when implementing a heterodyne detection

and balancing scheme with two photodiodes. The ND filters cause an asymmetry in the diffraction of the probe beams, allowing for recovery of both the real and imaginary components of the signal [170]. Balancing combined with chopping significantly reduces the experimental noise by increasing the detection rate and removing laser power fluctuations. However, as discussed in the Conclusions section of this thesis, the signal to noise still requires a factor of 10 improvement to study the dynamics of interest in J-aggregates due to highly efficient exciton-exciton annihilation [59, 61, 171, 172].

Chapter 4

J-Aggregates

The bulk of this thesis involves the study of supramolecular *J*-aggregates composed of hundreds to thousands of molecules tightly bound to one another [41, 40, 42]. *J*-aggregates were discovered in the 1930s when concentrated solutions of dye molecules exhibited a strong redshift, almost no Stokes' shift, band narrowing, and polarized absorption and fluorescence in a flowing solution [38, 39]. Cyanine dye molecules are the prototypical *J*-aggregating dyes, two of which are used in Chapter 5 of this thesis (Figure 4-1) and another in Chapter 6 (Figure 4-9).

J-aggregates are related to other multi-chromophoric systems, such as natural light harvesting antennae [12], and are modeled predominantly with Frenkel exciton theory [173, 19]. While electronic structure calculations are possible for very small

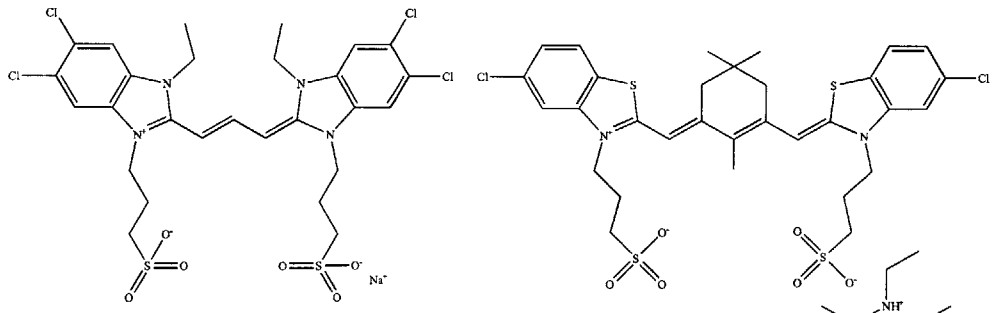

Figure 4-1: Two examples of cyanine dye molecules exhibiting *J*-aggregation under appropriate conditions.

aggregates, for larger structures they become intractable. The simpler Frenkel exciton theory captures much of the relevant physics and implications for experiments. In this chapter I introduce the two-level linear aggregate model [173] which leads to delocalized Frenkel excitons. Then, I introduce many of the properties and effects exhibited by even this simplified model. The final section of this chapter summarizes theoretical efforts in understanding tubular J-aggregates, specifically how they differ from the linear aggregate model.

4.1 Linear J-aggregate Model

4.1.1 Frenkel Exciton Hamiltonian

The simplest Frenkel excitons are formed in a dimer of two-level systems with a dipole-dipole interaction, J, between them [19, 174, 175]. The dipole-dipole coupling strength is determined by the dipole orientation and geometry,

$$J = \frac{\mu_1 \mu_2}{4\pi\epsilon_r r^3}(1 - 3\cos^2\theta), \tag{4.1}$$

with ϵ_r the relative permittivity, μ_1 and μ_2 the dipoles of molecules 1 and 2, r the distance between them, and θ the angle between them. Diagonalizing the Hamiltonian leads to two exciton states, one with the molecular wavefunctions in phase and one out of phase. The in-phase exciton will contain most of the oscillator strength because the two dipoles oscillate in phase, acting as a single enhanced dipole. The out-of-phase exciton will exhibit the opposite effect because the two dipoles oscillate out of phase and destructively interfere, leading to reduced oscillator strength for that state. As θ is tuned, J will change from positive to negative. When positive, the states with the dipoles in phase (as determined from diagonalizing the Hamiltonian) are the high energy states, leading to H-aggregates (Figure 4-2 (left)). When J is negative, the states with in-phase dipoles are the lowest energy states, leading to J-aggregates (Figure 4-2 (right)). Therefore in J-aggregates, the absorption spectrum is redshifted compared to the individual molecules (monomers).

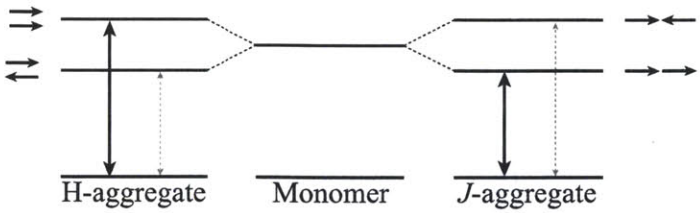

Figure 4-2: In a dimer of two-level molecules the geometrical arrangement and orientation of the dipoles determines the energetics. Dipoles arranged side-by-side lead to H-aggregates (left) while tail-to-head arrangement leads to J-aggregates (right).

Figure 4-3: Dipoles of many molecules in semi-head-to-tail geometry. Each molecule is treated as a point dipole with nearest-neighbor interaction strength J.

Extending the dimer model to include many two-level molecules (Figure 4-3), or sites, is straightforward and well-studied [173, 176, 177, 19]. For a J-aggregate, the dipoles are arranged in a semi-head-to-tail fashion, leading to interactions lowering the overall energy of the optically active states. The Frenkel exciton Hamiltonian for such an arrangement is,

$$H_0 = \sum_{n}^{N} \epsilon_n B_n^\dagger B_n + \sum_{m,n} V_{mn} B_m^\dagger B_n. \tag{4.2}$$

$B_n^\dagger$ is the creation operator for an excitation at site n and B_n is the corresponding annihilation operator with the restriction that the creation of multiple excitations on a single site is not allowed [173]. The dipole-dipole interaction between the different sites is $V_{mn} = -\frac{J}{|m-n|^3}$, with nearest-neighbor interaction strength J. The next two sections will describe the wavefunctions and dispersion properties of the Frenkel exciton Hamiltonian for idealized and disordered aggregates.

4.1.2 Idealized Many-Site Model

The simplest many-site model is homogeneous and restricted to nearest-neighbor interactions. With these constraints, the excitons are Fermions and the Hamiltonian

(Equation 4.2) can be solved exactly [178, 176]. For the following section the molecular transition energies are set to zero ($\epsilon_0 = 0$) and all energies are in reference to the nearest-neighbor interaction strength J. The eigenfunctions ($|k\rangle = \sum_n \phi_{kn}|n\rangle = \sum_n \phi_{kn} B_n^\dagger|g\rangle$), energies ($E_k$), and oscillator strengths ($F_k = (\mu_k)^2 = (\sum_n \phi_{kn})^2$) are

$$
\begin{aligned}
|k\rangle &= \sqrt{\frac{2}{N+1}} \sum_n \sin\frac{\pi k n}{N+1}|n\rangle, \\
E_k &= \epsilon_0 - 2J\cos\frac{\pi k}{N+1}, \\
F_k &= \left(\frac{1-(-1)^k}{2}\right)^2 \frac{2\mu_{mon}^2}{N+1}\cot^2\frac{\pi k}{N+1}.
\end{aligned} \tag{4.3}
$$

The eigenfunctions in Equation 4.3 are sinusoidal (Figure 4-4(a)) and resemble those from particle-in-a-box (see Table 4.1). The lowest energy state (S state) has zero nodes, with the number of nodes increasing with increasing quantum number. In addition, near the bottom of the exciton dispersion curve (Figure 4-4(b)), the dispersion follows $E \sim k^2$ (for small k, $\cos k \sim k^2$), also like particle-in-a-box. The physical intuition gained from these similarities is that the exciton, while delocalized across many molecules, is in fact localized in the aggregate and is therefore subject to quantum mechanical level repulsion and quantization. The level repulsion permits a highly sensitive probe for the size of the box, or the coherent size of the aggregate: the more localized the exciton, the larger the level splitting [179]. Expanding the dispersion relation for small k and taking the difference in energy between the lowest two states leads to

$$
\Delta = E_2 - E_1 = \frac{3J\pi^2}{(N+1)^2}. \tag{4.4}
$$

Table 4.1 lists the eigenfunctions, energies (for small k), and how the level splitting depends on the "box" size for both the idealized model and particle-in-a-box. In order to compare directly the parameters governing the dispersion and localization properties, the units must be the same. Multiplying N, the number of coupled molecules in the aggregate, by the lattice constant a gives the physical length of

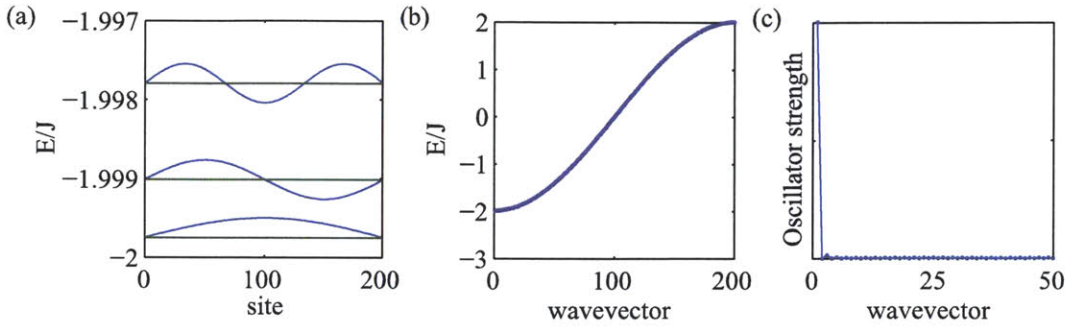

Figure 4-4: Eigenfunction properties of idealized aggregate. (a) First three eigenfunctions. (b) Dispersion relationship, energy E_k vs. wavevector k. (c) Oscillator strength vs. wavevector, demonstrating the concentration of oscillator strength in the superradiant low-wavevector (and low-energy) state.

Table 4.1: Properties of Aggregates and Particle-in-a-box

Property	Aggregate	Particle-in-a-box
Eigenfunctions	$\|k\rangle = \sqrt{\frac{2}{N+1}} \sum_n \sin \frac{\pi k n}{N+1} \|n\rangle$	$\psi_k(x) = \sqrt{\frac{2}{L}} \sin(\frac{\pi k x}{L})$
Energy	$E_k \approx -2J + \frac{J\pi^2 k^2}{(N+1)^2}$	$E_k = \frac{\hbar^2 \pi^2 k^2}{2mL^2}$
Size	$N = \pi \sqrt{\frac{3J}{\Delta}} - 1$	$L = \pi \sqrt{\frac{3\hbar^2}{2m\Delta}}$

the box. Comparing the equations for energy or for the size, we can see that the quantity aJ^2 for the aggregate plays the role of $\frac{\hbar^2}{2m}$ for the particle-in-a-box. The effective mass, m, is critical in determining excitonic properties in semiconductors, e.g. diffusion rates and dispersion. Comparing to the dispersion of the aggregate, the intermolecular coupling J plays a similar role. This intuitively makes sense as well: for stronger coupling one would expect the exciton to transfer faster between sites and exhibit faster and farther transport. This implies that possibilities for band tuning and control in semiconductors can be applied to aggregates by engineering the molecular geometry and orientation to tune the intermolecular interaction [180].

In the lowest energy eigenstate, $|k = 1\rangle$, all the dipoles are in phase. The oscillator strength for this state is $F_k = 0.81 N \mu_{mon}^2$, meaning that 81% of the aggregate's oscillator strength is held in this state (Figure 4-4(c)). Also, the factor N, the total number of coupled molecules, enhances the oscillator strength and optical properties of this state compared to the monomer, leading to superradiance and enhanced non-

linearities. States with an even quantum number, such as the P state ($k = 2$), have identically zero oscillator strength because half of the dipoles oscillate exactly out of phase with the other half. The next-highest dipole strength, for the D state ($k = 3$), is $0.09N\mu_{mon}^2$.

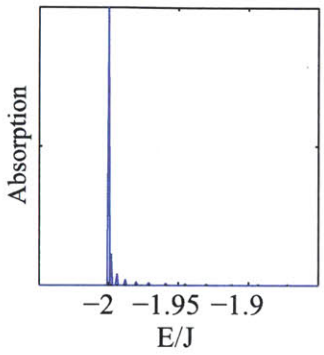

Figure 4-5: Absorption spectrum for idealized aggregate. The $|k = 1\rangle$ superradiant state is at the band edge while the other states contribute to a high-energy tail.

While the idealized aggregate model has several limitations, it readily explains many of the optical properties of J-aggregates. The optical absorption spectrum is calculated using the oscillator strength and the density of states, $A(E) = \sum_k |\mu_k|^2 \delta(E - E_k)$ (Figure 4-5). The large redshift with respect to the monomer, the asymmetric absorption spectrum with a high-energy tail, and reduced lifetimes due to superradiance are all features of the idealized model. In addition, polarized absorption and fluorescence would be expected from a linear structure because the aggregate strands would align in solution and both the absorption and fluorescence result from the same superradiant S states aligned along the length of the aggregate.

4.2 Disordered Aggregate Model

More advanced (and realistic) theories of Frenkel excitons may include additional molecular excited states, exciton-exciton interactions, all dipolar couplings, various models for inhomogeneity, and exciton-vibration coupling [41, 19, 42]. In this section I numerically simulate the properties of linear J-aggregates including all dipolar

couplings and describe how to include inhomogeneity and exciton-vibration (phonon) coupling and discuss some of the effects of their inclusion. While the main effect of including all dipolar couplings is to shift the band edge to $-2.403J$, the effects of including disorder and dephasing are non-trivial and numerous. The inhomogeneity is directly responsible for inhomogeneous dephasing. During a simulated experiment, whether it is linear absorption or a two-dimensional photon echo, the static disorder is kept constant for a single aggregate. Photon echo experiments can rephase the inhomogeneity, giving a measure of how large the distribution of disorder is. The optical response is then averaged over many different realizations of the static disorder, i.e. ensemble averaging. Exciton-phonon coupling leads to homogeneous dephasing, or dynamic disorder, and cannot be rephased. Exciton-phonon coupling further localizes the excitons as well, leading to a coherent exciton size that is smaller than that imposed by static disorder [181, 182, 183, 184]. For the following simulations I use linear chains of $N = 200$ sites with disorder $\sigma/J = 0.15$ averaged over 10,000 realizations of the disorder.

4.2.1 Static Disorder

Inhomogeneity is generally included as a Gaussian distribution of molecular excitation frequencies with a standard deviation σ, while all other parameters are held constant. For weakly-disordered J-aggregates σ/J values are typically on the order of $0.1 - 0.3$ [176, 185, 63]. This leads to excitons coherently delocalized across several to perhaps several dozen molecules. Due to disorder, some exciton states exist below the bare band edge ($-2.403J$); these excitons make up the Lifshitz tail and contain much of the oscillator strength. Therefore, these excitons produce most of the optical response of J-aggregates. Figure 4-6 displays several properties of a disordered aggregate for a single realization of the disorder. In Figure 4-6(a) the lowest energy eigenfunctions display properties similar to the idealized aggregate but localized to segments of the aggregate of size N_{coh} instead of N. Within a single localization segment, level repulsion occurs in the same manner as the idealized aggregate. Four eigenfunctions are highlighted which make up two pairs of S and P states localized on different

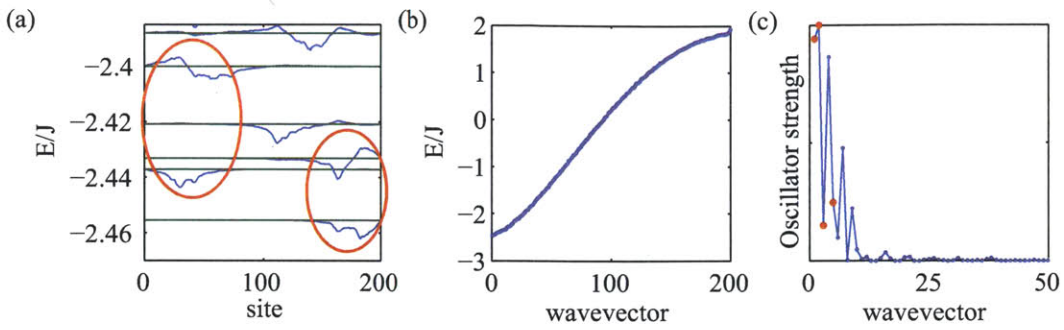

Figure 4-6: Disordered aggregate properties for a single realization of the disorder. (a) Six lowest eigenfunctions. The two pairs of highlighted eigenfunctions (red circles) exhibit a level structure similar to the homogeneous aggregate. (b) Exciton dispersion, showing similar structure to idealized aggregate. Key difference is the tail below $E/J = -2$. (c) Exciton oscillator strength. Oscillator strengths corresponding to the circled states in (a) are highlighted. Large oscillator strengths correspond to the S-like states while the low oscillator strengths correspond to the P-like states with nodes in the wavefunctions

segments of the physical aggregate; each pair of levels is split by an energy determined by the quantum confinement. The S-like states have almost all of the oscillator strength since their wavefunctions are in phase across many molecules whereas the P-like states have very small oscillator strengths (see highlighted oscillator strengths in Figure 4-6(c)). The dispersion curve (Figure 4-6(b)) is relatively unchanged compared to the idealized aggregate except for the shift of the band edge from $-2J$ to -2.403 caused by the additional intermolecular interactions and the Lifshitz tail caused by the disorder. As previously mentioned, the oscillator strength is mainly contained in the S-like states and all of the large wavevector (and high energy) excitons have essentially zero oscillator strength.

Calculation of the optical properties requires both the density of states, $\rho(E) = \langle \sum_k \delta(E - E_k) \rangle$, and the oscillator strength. These two quantities determine how many states at a particular energy have a particular oscillator strength. Due to the inhomogeneity analytical solutions are not possible and numerical averaging is required. The linear absorption is a product of the average oscillator strength and the density of states,

$$A(E) = \left\langle \sum_k |\mu_k|^2 \delta(E - E_k) \right\rangle . \tag{4.5}$$

Figure 4-7 displays the density of states (a), the oscillator strength (b), and the absorption spectrum (c). The density of states has peaks at the bottom and top of the exciton band because for small disorder the cosine dependence of the energy is relatively accurate and there are more states at the bottom and top of the band. As previously mentioned, the average oscillator strength peaks below the band edge in the Lifshitz tail at the energy corresponding to the S-like states. The absorption spectrum is peaked in the Lifshitz tail as well, with a Gaussian lineshape on the low energy side and a high-energy tail similar to the idealized model.

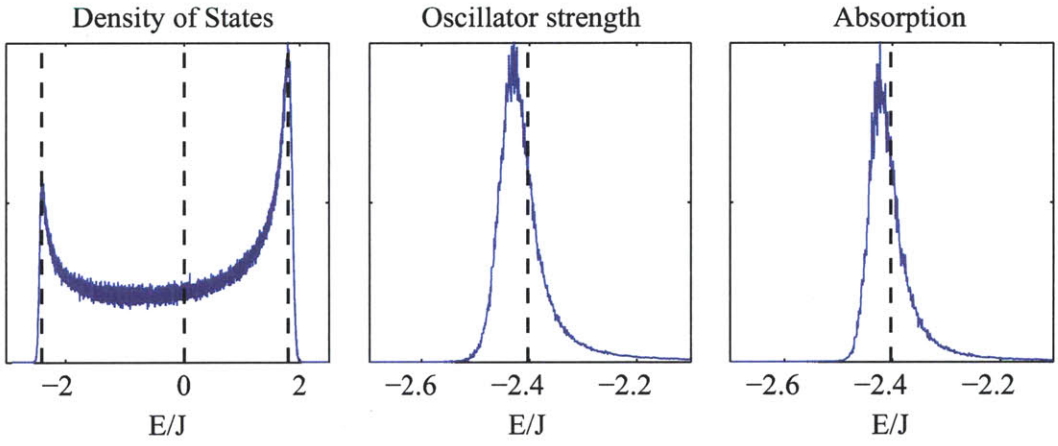

Figure 4-7: Ensemble-averaged properties. (a) Density of states, peaked at the lower band edge ($E/J = -2.403$) and upper band edge ($E/J = 1.803$). The Lifshitz tail, caused by disorder, extends below the lower band edge. (b) Exciton oscillator strength, concentrated in the Lifshitz tail. (c) Absorption spectrum, a product of the density of states and oscillator strength.

The low-energy Gaussian lineshape results from the static disorder and has a width $\sigma/\sqrt{N_{coh}}$, where N_{coh} is the average number of coherently coupled molecules in the localization segment. The reduction in width is caused by the delocalization of the exciton across many molecules, allowing it to sample and effectively average over the inhomogeneity in the transition energies [186, 176]. This is known as motional narrowing narrowing and is a well-known phenomena in spin systems [187], exciton-

polaritons [188], vibrations [189], and quantum dots [190] among others.

An additional effect caused by static disorder is Anderson localization [191, 192]. Excitons in a disordered environment are localized to segments and cannot hop between segments either coherently or incoherently, limiting exciton transport and dynamics and limiting the exciton to a single segment for the duration of its lifetime. The reason is level repulsion: when levels overlap spatially they repel each other in energy, requiring some event (phonon emission/absorption) to cause scattering. Conversely, excitons with similar energy will have non-overlapping wavefunctions, prohibiting hopping to one another without a scattering event to cause the change in momentum and energy. The next section describes how to include exciton-phonon coupling, enabling exciton transport and causing homogeneous broadening.

4.2.2 Exciton-Phonon Interactions

Theoretical modeling of transport and homogeneous dephasing requires inclusion of interactions between excitons and an environment, typically a thermal bath of phonon modes [173, 41, 193, 42]. Redfield theory is one class of theory that naturally incorporates the concepts of population transfer and dephasing and allows calculation of temperature-dependent properties such as the Stokes shift, fluorescence lifetime, absorption linewidth, and relaxation dynamics in general [194, 195, 83, 196, 197, 19]. In J-aggregates, exciton-phonon coupling is weak, as evidenced by the very small Stokes shift and lack of vibronic structure in either the absorption or fluorescence spectrum. The delocalized nature of the excitons leads to exchange narrowing (similar to motional narrowing), averaging over the dynamic fluctuations in site energies and couplings [198], reducing the effects of exciton-phonon coupling. This validates the use of a perturbative approach such as Redfield theory and leads to diagonal and off-diagonal fluctuations but does not require rediagonalization of the exciton wavefunctions, i.e. no polaron effects [199]. The Hamiltonian including exciton-phonon interactions is [200, 201, 202, 203, 204]

$$
\begin{aligned}
H &= H_0 + H_{bath} + V^{(1)} \\
H_0 &= \sum_n^N \epsilon_n B_n^\dagger B_n + \sum_{m,n} V_{mn} B_m^\dagger B_n \\
H_{bath} &= \sum_q \omega_q a_q^\dagger a_q \\
V^{(1)} &= \sum_n \sum_q V_{nq}^{(1)} B_n^\dagger B_n \left(a_q^\dagger + a_q\right).
\end{aligned} \tag{4.6}
$$

H_0 is the Frenkel exciton Hamiltonian, H_{bath} is the Hamlitonian for the bare phonon modes, and $V^{(1)}$ is the interaction potential containing a linear coupling term (only interactions where a single phonon is absorbed or emitted are included). $a_q^\dagger$ and a_q are the boson raising and lowering operators for the phonon mode with momentum q, and $V_{nq}^{(1)}$ is the coupling strength between phonon mode q and site n. The interaction potential in the exciton basis rather than the site basis is

$$
V^{(1)} = \sum_{k',k} \sum_q V_{k'kq}^{(1)} |k'\rangle\langle k| \left(a_q^\dagger + a_q\right) \tag{4.7}
$$

with

$$
V_{k'kq}^{(1)} = \sum_n V_{nq}^{(1)} \phi_{k'n} \phi_{kn}. \tag{4.8}
$$

The scattering (population transfer) rates between exciton states $|k'\rangle$ and $|k\rangle$ and initial phonon state i to the final state f can be calculated from Fermi's golden rule. Alternatively using Redfield theory, when incorporating linear system-bath coupling and using the secular approximation (no coupling between populations and coherences), the population transfer rate calculations reduce to Fermi's golden rule [83, 79].

$$
W_{k'k} = 2\pi \sum_i \sum_f \rho_i \left\langle |\langle k', f|V^{(1)}|k, i\rangle|^2 \right\rangle \delta(E_{k'} - E_k + \Omega_f - \Omega_i). \tag{4.9}
$$

Linear exciton-phonon coupling combined with Fermi's golden rule means that when excitons scatter the energy of the absorbed or emitted phonon must match the energy difference between the exciton states. In Equation 4.9 the initial phonon density matrix, ρ_i, determines which phonons modes are occupied and therefore available for scattering, the squared matrix element is the transition strength between the initial and final states, and the delta function ensures energy conservation. Assuming a stochastic bath ($\langle V_{nq}^{(1)} \rangle = 0$ and $\langle V_{mq}^{(1)} V_{nq}^{(1)*} \rangle = \delta_{mn} |V_q^{(1)}|^2$) and inserting $V_{k'kq}^{(1)}$ into Equation 4.9 leads to,

$$W_{k'k} = 2\pi \sum_n \phi_{k'n}^2 \phi_{kn}^2 \sum_q |V_q^{(1)}|^2 \left([n(\omega_q) + 1] \delta(\omega_{k'k} + \omega_q) + n(\omega_q) \delta(\omega_{k'k} - \omega_q) \right). \tag{4.10}$$

Defining the one-phonon spectral density as

$$F(\omega) = 2\pi \sum_q |V_q^{(1)}|^2 \delta(\omega - \omega_q) \tag{4.11}$$

we can re-write $W_{k'k}$ as

$$W_{k'k} = \sum_n \phi_{k'n}^2 \phi_{kn}^2 \times F(|\omega_{k'k}|) \times \begin{cases} n(\omega_{k'k}) & \omega_{k'k} > 0 \\ n(-\omega_{k'k}) + 1 & \omega_{k'k} < 0 \end{cases} \tag{4.12}$$

with the boson occupation number $n(\omega) = [\exp(\hbar\omega / k_b T) - 1]^{-1}$.

Equation 4.12 contains three components. The first component is purely excitonic and is proportional to the wavefunction overlap between the initial and final excitons. In the discussion of Anderson localization, excitons that did not overlap could not undergo energy transfer, and the same concept holds in this case. However, states with strong overlap, such as the S and P states, will undergo population transfer by emitting or absorbing photons. In addition, the localized excitons in the Lifshitz tail may transfer energy via a higher-wavevector, more delocalized state that overlaps both excitons. The second component in Equation 4.12 is the spectral density, the coupling-weighted density of states. The spectral density is essentially the product

of the exciton-phonon coupling strength multiplied by the number of states for a particular phonon, and determines which phonons are coupled to the exciton, how many of the phonon modes there are, and how strong the coupling is. The final component in Equation 4.12 is the boson occupation number which simply describes how many phonons exist in a particular mode at a particular temperature. This is the only explicitly temperature-dependent quantity and, coupled with the spectral density, determines the temperature dependence of the exciton scattering rates.

The spectral density contains all the details of the phonon bath modes and many models have been applied to J-aggregates and related photosynthetic light harvesting complexes that include host vibrations, acoustic phonons, intramolecular vibrations, and optic phonons[205, 19, 206, 193, 207]. In particular, Debye-type models with a cutoff frequency ω_c, where $F(\omega) \propto \left(\frac{\omega}{\omega_c}\right)^3 \exp(-\omega/\omega_c)$, have been used to simulate the effect of low wavelength acoustic phonon coupling to excitons [200, 201, 202, 203, 204].

Exciton scattering causes population rearrangement and relaxation within the band, contributing to homogeneous dephasing of the exciton. In general, the homogeneous dephasing rate is the sum of exciton scattering rates and the exciton lifetime, $\Gamma_k = |\mu_k|^2\Gamma_0$, where Γ_0 is the lifetime of the uncoupled monomer,

$$\gamma_k = \frac{1}{2}\sum_{k'(\neq k)} W_{k'k} + \frac{1}{2}|\mu_k|^2\Gamma_0. \tag{4.13}$$

The dephasing rates are used to calculate linear and nonlinear optical spectra (see Chapter 2). For example, the linear absorption spectrum can be calculated using Equation 4.5 or the response function approach in Chapter 2 as

$$A(E) = \left\langle \sum_k |\mu_k|^2 \frac{\gamma_k}{(E-E_k)^2+\gamma_k^2} \right\rangle. \tag{4.14}$$

The linear absorption spectra shown in Figure 4-8 include both static disorder and homogeneous dephasing with $F(\omega) = 20J\,(\omega/J)^3$. They increase in temperature from left to right, showing the increasing effect of homogeneous dephasing. For a typical J-aggregate, $J \approx 600\ \mathrm{cm}^{-1}$, giving temperatures of 17, 130, and 215 K for the calculated spectra.

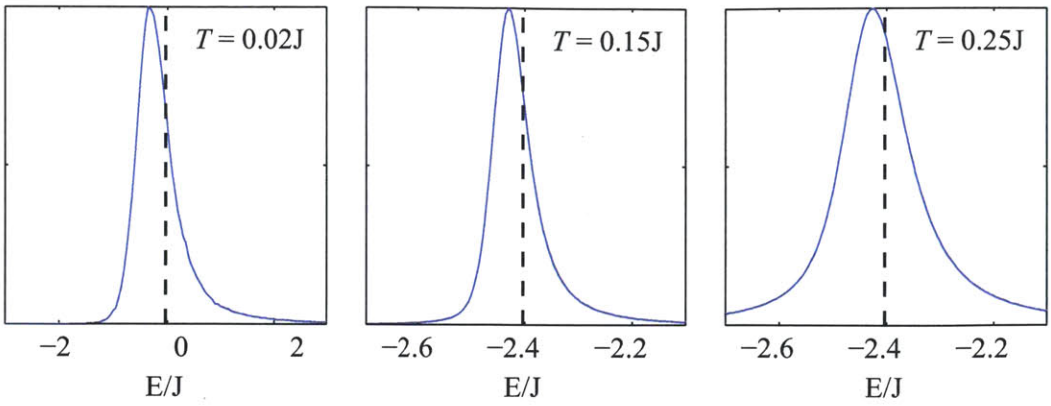

Figure 4-8: Absorption spectra for J-aggregate averaged over the ensemble, including both static disorder and homogeneous dephasing (exciton-phonon coupling). Temperature increases from left to right, demonstrating the effect of increasing homogeneous dephasing.

4.3 Two-Exciton States

The previous sections dealt with single excitons within a J-aggregate. In principle J-aggregates can support as many excitons as there are molecules, although the material would certainly degrade before being fully occupied with excitons. However, it is certainly possible to see two or three excitons per aggregate. Linear spectroscopy only depends on the one-exciton manifold of states as the two-exciton−ground state transition is dark, but nonlinear spectroscopy will have contributions from the higher manifolds of excitons [193]. Third-order ($\chi^{(3)}$) nonlinear spectroscopy in particular is sensitive to the double-excited manifold, i.e. two-exciton states, via excited-state absorption and two-quantum spectroscoy (see Chapter 2). The rest of this section will focus on the two-exciton states as they are relevant states for $\chi^{(3)}$ spectroscopy.

There are N exciton states, one for each molecule, and $N(N-1)/2$ two-exciton states (for each excited molecule can have each of the others excited). Similar to the one-exciton states, the properties of the two-exciton states can only be derived analytically for the idealized linear chain. The Fermionic nature of the idealized excitons means that the two-exciton wavefunctions are anti-symmeterized combinations of one-exciton wavefunctions, giving the two-exciton energies and one- to two-exciton transition dipole moments [208, 59],

$$|K = k_1, k_2\rangle = \sum_{n<m} (\phi_{k_1 n}\phi_{k_2 m} - \phi_{k_1 m}\phi_{k_2 n})|n, m\rangle. \tag{4.15}$$

$$E_K = E_{k_1} + E_{k_2}. \tag{4.16}$$

$$\mu_{k,K} = \mu_{mon} \sum_{n<m} (\phi^*_{kn} + \phi^*_{km}) \times (\phi_{k_1 n}\phi_{k_2 m} - \phi_{k_1 m}\phi_{k_2 n}). \tag{4.17}$$

The lowest energy two-exciton state is $|K = 1, 2\rangle$, or an SP-hybrid state. The transition between this state and the $|k = 1\rangle$ one-exciton state contains the majority of the oscillator strength for the one- to two-exciton transitions [59]. Therefore, in nonlinear spectroscopy, even for disordered non-ideal aggregates, it is possible to use the simple idea of S and P states localized to segments of the aggregate to interpret the spectra. The picture for excited-state absorption is a single exciton in the S state localized to some segment of the aggregate, and an additional excitation populates the P state localized on the same segment.

Two-exciton states are particularly sensitive to exciton-exciton interactions which lead to effects such as bound biexcitons and exciton-exciton annihilation [104, 209, 210, 211]. Perturbations to the two-exciton states lead to energetic shifts and lineshape changes similar to anharmonicity and coupling effects in vibrational systems [212, 213, 99]. For example, two-quantum spectroscopy has been used to detect directly exciton-exciton scattering to determine the interaction strength [209, 70]; and exciton-exciton annihilation has been modeled by coupling two-exciton states to high energy molecular excited states, activating a nonradiative recombination pathway for two excitons [210, 211, 214, 215].

4.4 Tubular *J*-aggregates

In Section 4.1.2 I alluded to the idea that band tuning for J-aggregates is possible by tuning the intermolecular geometry and interaction. One example in recent years has been using amphiphilic cyanine dyes to tune the morphology and the resulting

excitonic structure [43, 44, 45, 216, 46, 47, 48, 217]. Figure 4-9(a) shows the molecular structure for one such dye, C8S3. The only difference between BIC (Figure 4-1) and C8S3 is one of the side chains. The hydrophilic side chain (red highlight) is the same as BIC, however the hydrophobic carbon chain (grey highlight) is eight carbons long in C8S3 rather than two.

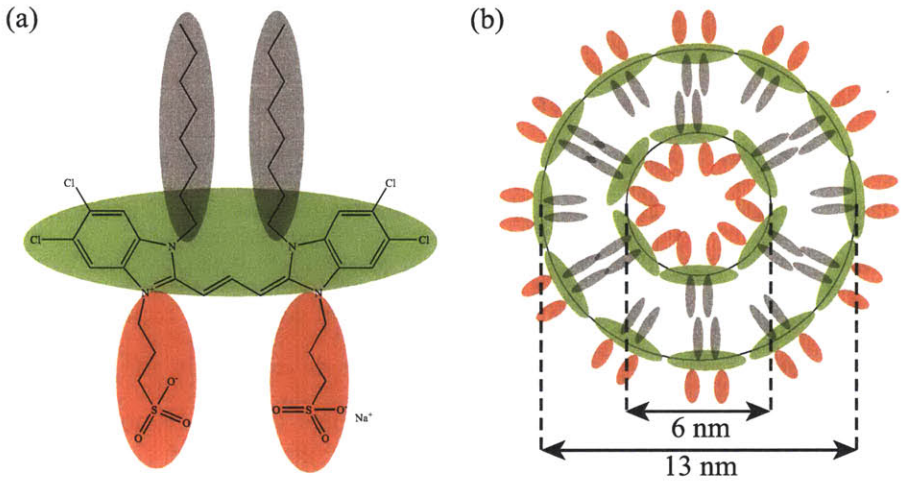

Figure 4-9: (a) Molecular structure of amphiphilic C8S3 molecule with hydrophobic (grey) and hydrophilic (red) side chains. (b) Pictorial model of tubular J-aggregate structure and morphology.

In aqueous solution the hydrophobic and hydrophilic interactions cause the C8S3 molecules to self-assemble into double-wall cylindrical nanotubes [47, 217]. Figure 4-9(b) depicts the double wall structure with the hydrophobic carbon chains in between the two walls, isolated from water molecules; the hydrophilic side chains are on the outside of the outer wall and the inside of the inner wall, promoting favorable energetic interactions and stabilizing the structure. Previous cryo-TEM studies found an inner wall diameter of 6 nm and outer wall diamter of 13 nm with nanotube lengths on the order of hundreds of nanometers [47, 217].

After self-assembly the typical signs of J-aggregation appear in the optical spectrum: a strong red shift, narrowing of the absorption lineshapes, and the disappearance of the Stokes shift. In addition, the aggregate spectrum exhibits several absorption peaks whereas the monomer has a single peak with a phonon sideband

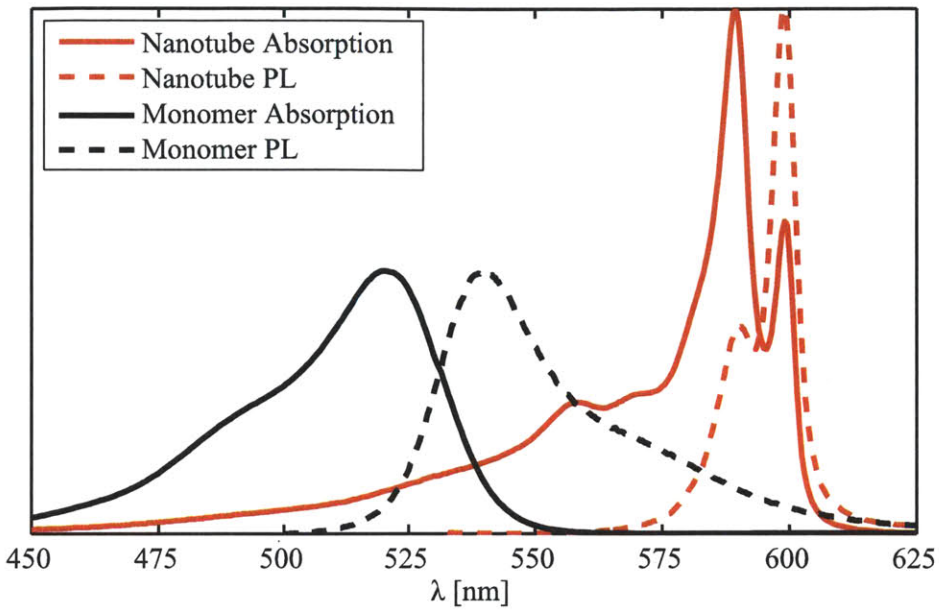

Figure 4-10: Optical spectra for C8S3 monomer (grey) and J-aggregate (red), showing the red shift, line narrowing, and reduced Stokes shift upon aggregation for the absorption spectra (solid lines) and fluorescence spectra (dashed lines).

at higher energy (see Figure 4-10). While cryo-TEM is useful for understanding the prevalent morphology, the resolution is not high enough to determine the actual molecular packing and geometry and therefore cannot give insight on the origin of the new absorption peaks. Understanding the new excitonic structure requires a new level of Frenkel exciton theory extended to multiple dimensions to account for the three-dimensional structure of the nanotube. A combination of the extended Frenkel exciton theory and optical spectroscopy has been highly successful in explaining many of the properties of tubular J-aggregates [218, 219, 220, 217]. In the following sections I give a brief overview of the theoretical foundations and some basic insights that help explain many of the properties of the optical spectra.

The Frenkel exciton Hamiltonian is the same as before except that each site (molecule) is now represented by a vector rather than a single point,

$$H_0 = \sum_{\mathbf{n}} \epsilon_{\mathbf{n}} B^{\dagger}_{\mathbf{n}} B_{\mathbf{n}} + \sum_{\mathbf{m},\mathbf{n}} V(\mathbf{m}-\mathbf{n}) B^{\dagger}_{\mathbf{m}} B_{\mathbf{n}}, \tag{4.18}$$

where $V(\mathbf{m}-\mathbf{n})$ is the dipole-dipole interaction potential and depends on the distance and relative orientation between the two interacting molecules at positions $\mathbf{m}$ and $\mathbf{n}$,

$$V(\mathbf{m}-\mathbf{n}) = \frac{\boldsymbol{\mu}_\mathbf{m} \cdot \boldsymbol{\mu}_\mathbf{n}}{|\boldsymbol{r}_\mathbf{mn}|^3} - 3\frac{(\boldsymbol{\mu}_\mathbf{m} \cdot \boldsymbol{r}_\mathbf{mn})(\boldsymbol{\mu}_\mathbf{n} \cdot \boldsymbol{r}_\mathbf{mn})}{|\boldsymbol{r}_\mathbf{mn}|^5} \tag{4.19}$$

Using Equation 4.18 the eigenfunctions, oscillator strength, and absorption spectrum are found as previously,

$$\begin{aligned} |\mathbf{k}\rangle &= \sum_\mathbf{n} \phi_\mathbf{k}(\mathbf{n}) B_\mathbf{n}^\dagger |g\rangle, \\ F_\mathbf{k} &= \sum_\mathbf{m,n} \phi_\mathbf{k}(\mathbf{m}) \phi_\mathbf{k}^*(\mathbf{n}) \left\langle (\mu_\mathbf{m} \cdot \mathbf{e})(\mu_\mathbf{n} \cdot \mathbf{e}) \right\rangle, \\ A(E) &= \sum_\mathbf{k} F_\mathbf{k} \delta(E - E_\mathbf{k}). \end{aligned} \tag{4.20}$$

Here, $\langle \ldots \rangle$ represents the average over the orientations of the nanotube molecules with respect to the excitation field polarization vector $\mathbf{e}$. The simplest microscopic model treats each molecule as a point dipole. A two-dimensional grid of molecules is rolled up into a cylinder, similar to carbon nanotubes. The intermolecular orientations and distances as well as wrapping angle determine the excitonic properties (Figure 4-11). The basis vectors $\mathbf{a}_1$ and $\mathbf{a}_2$ and the wrapping vector $\mathbf{c}$ determine the geometry of the cylinder.

In principle the molecules from different walls are coupled to one another. However, the large *inter*wall−intermolecular distances compared to *intra*wall−intermolecular distances greatly reduce the coupling strength [219]. Therefore, to a first approximation, the two walls can be treated as independent excitonic systems and the optical response for the double-wall cylinder is simply the sum of the responses from the two walls calculated independently.

In the homogeneous aggregate model for nanotubes (no disorder or dephasing), previous studies found that for periodic boundary conditions each cylinder can be separated into independent rings stacked on top of one another, each rotated with

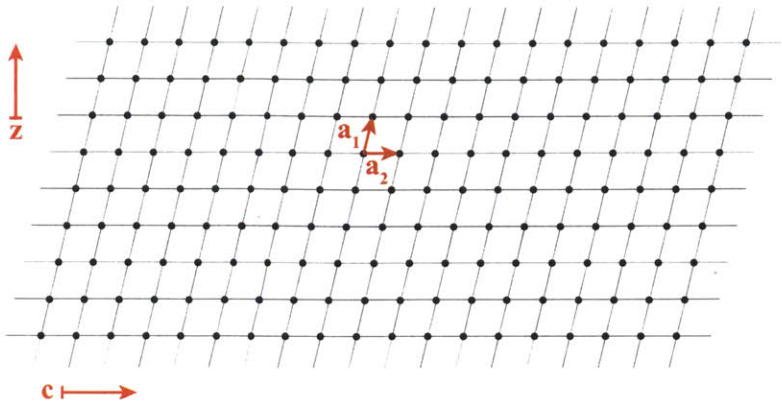

Figure 4-11: Microscopic two-dimensional sheet geometry. The vectors $\mathbf{a}_1$ and $\mathbf{a}_2$ describe the relative positions of the molecules, $\mathbf{z}$ is the longitudinal axis of the tube, and $\mathbf{c}$ is the wrapping vector along which the two-dimensional sheet is rolled to make a nanotube.

respect to the nearest-neighbor by a helical angle set by the wrapping vector [218]. The Hamiltonian separates into independent one-dimensional contributions: a longitudinal contribution of N_1 rings (oriented along $\mathbf{z}$ in Figure 4-11) that gives the same solutions as the one-dimensional chain; and a set of independent rings each with N_2 molecules rotated with respect to one another due to the wrapping angle. Each ring gives Bloch waves with wavefunctions $\sim \exp(i2\pi k_2 n_2/N_2)$ $(k_2 = 0, \pm 1, \ldots, N_2/2)$. The three-dimensional nature of the nanotube gives rise to three different exciton bands that contribute to the wavevector $\mathbf{K} = (k_1, k_2)$: the longitudinal band, characterized by the wavevector k_1, and two degenerate perpendicular bands with wavevectors $+k_2$ and $-k_2$. After isotropic averaging only three $\mathbf{K}$ states contribute to the optical spectra. The first is $\mathbf{K} = (k_1 = 0, k_2 = 0)$, a fully superradiant state polarized along the long axis of the tube (parallel to $\mathbf{z}$). The polarization is due to the fact that the molecular orientation rotates around the ring; the total contribution from the dipoles in each ring exactly cancel out. However, the dipole contribution along the length of the nanotube do not cancel out, similar to a one-dimensional exciton. The second and third states are degenerate with $\mathbf{K} = (k_1 = 0, k_2 = \pm 1)$, polarized perpendicular to $\mathbf{z}$. For these states the dipole contribution around the ring adds constructively while the contribution along the long axis cancel out, leading to per-

pendicularly polarized excitons. Therefore, we expect four excitonic transitions for double-wall nanotubes, two from each wall. The energies and exact polarization conditions for each wall depends on the molecular geometry for that wall, which is not necessarily the same.

The predictions above give a good foundation on which to interpret spectra of nanotubular J-aggregates, however there are several factors that can cause significant deviations. Discarding periodic boundary conditions and allowing for finite chain length increases the number of states contributing to the optical properties [220]. This is similar to the difference between a ring-shaped aggregate with a single state that has all the oscillator strength and the linear chain discussed in Section 4.1.2 where the oscillator strength is shared with higher energy states. Disorder also breaks the cylindrical selection rules in addition to changing the energies of the excitons [221]. This is because the excitons are localized by disorder and thus no longer wrap completely around the rings or extend fully down the long axis of the tube, giving incomplete cancelation of the perpendicular dipoles. Finally, recent studies on C8S3 double-wall J-aggregate nanotubes have suggested that one molecule per unit cell is insufficient to explain the optical properties. Two molecules per unit cell, in combination with disorder and multiple cylinders, were used to explain fully the exciton band structure in Figure 4-10 [217]. Chapter 6 of this thesis explores this system in more detail.

Chapter 5

Exciton Delocalization in Superradiant Molecular Aggregate Films

In this chapter I present results published by Arias et al., J. Phys. Chem. B 2012 [222]. Two-dimensional Fourier transform optical spectroscopy measurements of two types of molecular J-aggregate thin films show that temperature-dependent dynamical effects govern exciton delocalization at all temperatures, even in the presence of significant inhomogeneity. Our results indicate that in the tested molecular aggregates, even when the static structural disorder dominates exciton dephasing dynamics, the extent of exciton delocalization may be limited by dynamical fluctuations, mainly exciton-phonon coupling. Thus inhomogeneous dephasing may mediate the exciton coherence time while dynamical fluctuations mediate the exciton coherence length.

5.1 Motivation and Background

Naturally occurring light harvesting complexes are nanoscale systems optimized for light collection and energy transfer efficiency. Extensive study of these complexes has been aimed at understanding the underlying physical phenomena, including excitonic coherence and transport [5, 12, 223, 21, 20], that may be exploited for the develop-

ment of new nano-photonic technologies. It has been of particular interest to fabricate and characterize thin films of molecular aggregates [51], as they may enable many of the features of light harvesting complexes to be adapted for selective applications and they may be integrated into active optoelectronic structures [73, 52, 224]. Fabrication has recently been accomplished by forming thin films of J-aggregated polar molecules, a class of molecular aggregates that are related to natural antenna complexes and that are synthetically tractable [38, 41]. The optical responses of various J-aggregate morphologies are well correlated to specific synthesis routes, providing a method for tuning the excitonic properties of the aggregates for future applications [48, 47, 46, 43]. In J-aggregates, the number of molecules over which an exciton is delocalized mediates the linear and nonlinear optical responses such as absorption and superradiance [225, 184] as well as coherent and incoherent exciton transport [226, 227, 228, 229, 172, 230]. Several device architectures incorporating J-aggregate films take advantage of the excitons' enhanced optical responses [56, 55, 231, 73, 36]. However, the relationships between exciton coherence and J-aggregate film morphology, structure, and environmental effects are not well understood. There are multiple mechanisms that limit exciton delocalization or coherence length N_{coh} (given in terms of the number of chromophores), including static disorder in the chromophore positions, energies, and orientations, and dynamic fluctuations caused primarily by exciton-phonon scattering [225, 184, 181, 201, 203]. At low temperature T, exciton-phonon scattering should be infrequent and the delocalization could be limited to a value N_{del}^{s} due to static disorder, e.g. due to grain boundaries within the J-aggregated thin film (Figure 5-1(a), left). At high T, exciton-phonon scattering will localize the exciton further (Figure 5-1(a), right) to a dynamically limited length $N_{del}^{d}(T)$. In spectroscopic measurements, static disorder manifests as inhomogeneous dephasing and dynamic disorder as homogeneous dephasing, offering prospects for determination of the amount and type of disorder present in a system if the two types of dephasing can be distinguished.

5.2 Nonlinear Spectroscopy Applied to J-aggregates

Homogeneous and inhomogeneous dephasing are convolved in the lineshapes obtained in one-dimensional linear optical spectra. We used two-dimensional Fourier transform optical (2D FTOPT) spectroscopy, which spreads spectral lines over two frequency axes, to separate the contributions to dephasing and to assess their effects on exciton delocalization. 2D FTOPT spectra were obtained for thin films of J-aggregating cyanine dyes and recorded over a range of temperatures. From the 2D spectra we extracted energy-dependent exciton coherence lengths by comparing ground-state and excited-state absorption frequencies whose difference depends on exciton size as discussed further below. While exciton coherence dynamics have been investigated using 2D FTOPT spectroscopy in various nanostructured materials including J-aggregates [110, 106, 223, 21, 20, 232, 185, 68, 69], a systematic temperature-dependent study has not been reported that correlates energy-dependent exciton delocalization directly to both homogeneous and inhomogeneous dephasing.

In our 2D FTOPT measurements the first field, E_1, excites exciton coherences and, after an "absorption" time delay τ_{abs}, the second field, E_2, generates a spatially varying grating pattern of exciton population. After a waiting time delay equivalent to the pump-probe delay time, the third field, E_3, creates third-order coherences between the exciton state and either the ground state or higher lying, doubly excited states. After an "emission" time delay, τ_{emi}, the associated polarizations radiate the signal field, E_{sig}, superposed in the phase-matched direction with the reference field, E_{LO}, spectrally dispersed, and measured interferometrically to yield the complex signal. The (emission) frequency-resolved measurement is conducted as a function of the absorption time delay with respect to which Fourier transformation gives the 2D FTOPT spectrum whose peaks reveal the absorption and emission coherence frequencies.

With the time-ordering of femtosecond pulses illustrated in Figure 5-1(b), we measure 2D rephasing or photon echo (PE) spectra whose linewidths along the anti-diagonal and diagonal frequency directions respectively yield the homogeneous and

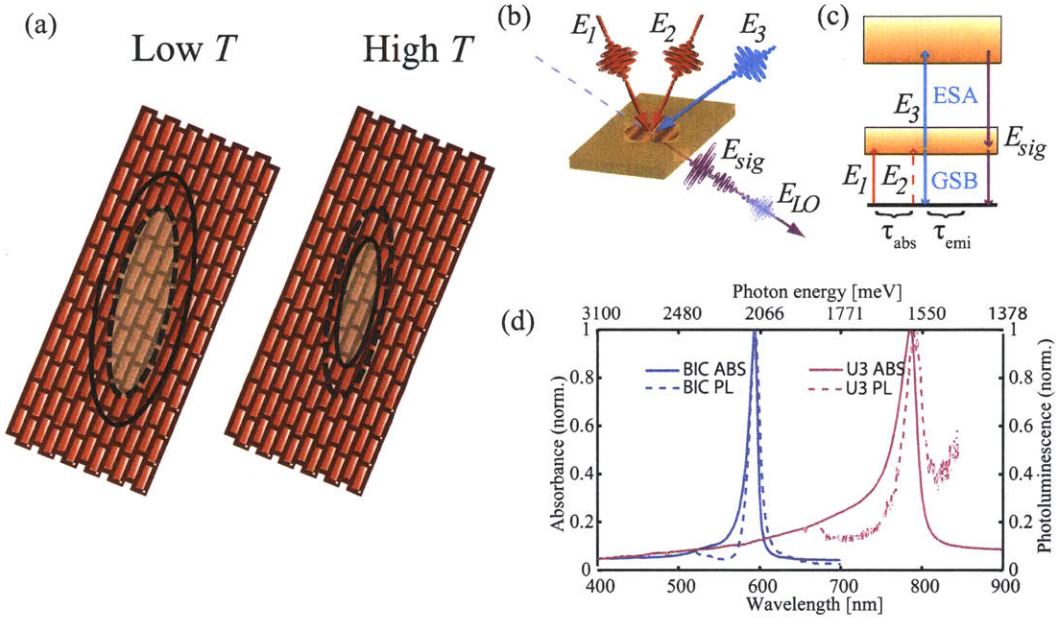

Figure 5-1: (a) Schematic illustration of J-aggregate molecular brickwork structure overlaid by pseudo-1D delocalized excitons (shaded in white). The dashed and solid ovals represent the exciton delocalization size limits imposed by static inhomogeneiety (T-independent N^s_{del}) and by dynamic fluctuations ($N^d_{del}(T)$), respectively. In this illustration the exciton size N_{coh} is limited by N^s_{del} at low T and $N^d_{del}(T)$ at high T. (b) Experimental geometry for 2D FTOPT spectroscopy of J-aggregate thin films. (c) Bands of one-exciton and two-exciton states and pulse interaction sequence for 2D FTOPT experiments, with the ground-state bleach (GSB) and excited-state absorption (ESA) signals indicated. (d) Room temperature linear absorption (ABS) and fluorescence (PL) for BIC and U3 J-aggregate thin films.

inhomogeneous dephasing rates [233, 234]. With the time-ordering of fields E_1 and E_2 reversed, we measure 2D non-rephasing spectra. Adding the rephasing and non-rephasing spectra, resulting in correlation spectra (CS), eliminates phase-twisted line-shapes that appear in the 2D PE spectra due to mixing of absorptive and dispersive contributions to the nonlinear signal. The resulting line shapes can be interpreted as purely absorptive and dispersive signals [122]. The absorptive signal can be directly compared to a pump-probe spectrum where the frequency resolution of the pump is given by Fourier transform relationships while femtosecond time resolution is maintained. Like a pump-probe spectrum, a 2D CS can be used to obtain the exciton coherence size, N_{coh} [63]. However a broadband spectrally resolved pump-probe (SRPP) experiment will report only an averaged value because there is no selective excitation within the inhomogeneous exciton absorption spectrum [177, 235]. For a pump-probe experiment using narrowband pulses, it is possible to determine both the absorption and emission frequencies, and therefore which excitons are excited. However, narrowband pulses are inherently long in duration and if exciton relaxation occurs during the pulse it is no longer clear that the probed exciton is the same as the initially excited exciton. Using short pulses in 2D FTOPT spectroscopy circumvents this limitation by frequency resolving the excitation energy through Fourier transformation and resolving the emission via a spectrometer, resulting in both high time and frequency resolution.

5.3 Experimental Details

The two J-aggregates studied were formed by cyanine dye molecules 1,1'-diethyl-3,3'-bis(sulfopropyl)-5,5',6,6'-tetrachlorobenzimidacarbo-cyanine (CAS No. 28272-54-0) and (3-[(2Z)-5-chloro-2-[((3E)-3-[5-chloro-3-(3-triethylammonium-sulfonatopropyl)-1,3-benzothiazol-3-ium-2-yl]methylene]-1,3-benzothiazol-3(2H)-yl] propane-1-sulfonate) (CAS No. 202135-09-9), which we refer to as BIC and U3, respectively. Both aggregates were deposited as thin film structures on sapphire substrates. BIC J-aggregates were formed via a layer-by-layer deposition method and consisted of 4.5 alternating lay-

ers, each 1.7 nm thick, of a cationic polymer and the anionic J-aggregating molecule to form a 7.7 nm thick film[51]. U3 J-aggregates were prepared by spin-casting a thin film at 2000 rpm from a 2,2,2-trifluoroethanol solution (2 mg/mL) onto the substrate that had been cleaned as described previously [51, 55]. Atomic force micrographs indicated that the U3 film was 20 nm thick, with an RMS roughness of 0.8 nm. Sample deposition and preparation were performed in nitrogen atmosphere. Optical measurements were performed in a Janis ST100 cold-finger cryostat. For 2D FTOPT measurements on BIC J-aggregates, a Coherent Libra Ti:Sapphire amplifier pumped a non-collinear parametric amplifier with 100 fs, 40 μJ pulses at 10 kHz to give pulses tuned to the absorption maximum of 595 nm and compressed to 50 fs with a time-bandwidth product near 0.6 by a UV fused silica prism pair. A KM Labs Ti:Sapphire oscillator with transform-limited 35 fs pulses at 92.5 MHz was tuned to an emission wavelength of 785 nm for measurements of the U3 J-aggregate film. In both experiments, the laser beam was focused to a 2D phase mask patterned to give efficient first-order diffraction at the appropriate wavelength. The four first-order diffracted beams composing the BOXCARS geometry were isolated and directed into a diffraction-based pulse shaper consisting of a grating and cylindrical lens that spectrally dispersed and focused the beams onto a 2D liquid crystal spatial light modulator (Hamamatsu X8267 for U3 experiments, Hamamatsu X7550 for BIC), giving full control of the spectral phase profile of each beam. This setup allowed control of optical delays and phases while maintaining full phase stability among the beams [136, 110, 106]. About 100 pJ/pulse was used during all experiments to minimize exciton-exciton annihilation effects. We used a procedure outlined by Siemens et al [234] to extract dephasing rates from the diagonal and anti-diagonal lineshapes of the 2D photon echo spectra.

The experimental procedures followed that of Turner et al. [136] Briefly, the laser beam first entered a beam shaper consisting of a 1:1 telescope around a two-dimensional binary phase mask pattern of 20 μm period. The four first-order diffraction spots were isolated and sent into a 4f-pulse shaper for diffraction-based pulse shaping. The beams were spectrally dispersed by diffraction from a grating (typi-

cally around 1000 lines/mm). The dispersed frequency components were focused by a cylindrical lens onto a two-dimensional spatial light modulator (SLM). Each dispersed beam occupied a different horizontal stripe of the SLM, where independent frequency-dependent phase patterns were applied to control the relative phases and temporal delays of the pulses in the beams. The longest delay in the experiments was 2.5 picoseconds, well within the capabilities of the pulse shaper. Control over the phase of each spectral component in each dispersed beam was achieved by a sawtooth diffraction pattern in the vertical dimension of the SLM. The amplitude and phase of the first-order diffracted spot were controlled by the amplitude and spatial phase of the diffraction pattern. The first-order diffraction spots for all the beams were reflected by a pick-off mirror in the Fourier plane, isolated spatially, and collimated by the exit lens of the pulse shaper. The four beams were focused by a final 15 cm lens onto the sample, and the signal and reference beams were collected by another 15 cm lens and sent to a spectrometer. Due to the pixelated nature of the pulse shaping SLMs, there is a decrease of light intensity as a pulse is delayed [236]. This leads to a decrease in signal as a function of time delay, and thus to an apparent increase in dephasing rate. However, the intensity roll-off is approximately exponential, allowing a simple correction for determination of the experimental dephasing rates.

5.4 Theoretical Description

Excitons in J-aggregating cyanine dyes are well described by the Frenkel model for interacting molecular excitations [181, 201, 203]. The molecules can be assumed to be arranged in a one-dimensional chain, but it is straightforward to extend to higher dimensions as in the case of cylindrical aggregates [220, 219, 237, 69].

5.4.1 Excitons in One Dimension

The analysis and interpretation of the experimental data in this chapter is carried out using the formalism for one-dimensional Frenkel excitons. For one-dimensional Frenkel excitons the Hamiltonian is

$$H = \sum_{\mathbf{n}} \epsilon_{\mathbf{n}} B_{\mathbf{n}}^{\dagger} B_{\mathbf{n}} + \sum_{\mathbf{m} \neq \mathbf{n}} J(\mathbf{m} - \mathbf{n}) B_{\mathbf{m}}^{\dagger} B_{\mathbf{n}}. \tag{5.1}$$

The molecules are labeled by the index $\mathbf{n}$ while $B_{\mathbf{n}}^{\dagger}$ creates an electronic excitation on molecule $\mathbf{n}$. The intermolecular coupling, $J(\mathbf{m} - \mathbf{n})$, is treated as dipole-dipole mediated transfer, thus $J(\mathbf{m} - \mathbf{n}) = \frac{-J}{|\mathbf{m}-\mathbf{n}|^3}$. Static disorder is introduced through a distribution of site energies, $\epsilon_{\mathbf{n}}$, centered around the average site energy ϵ_0. Diagonalization of the disordered exciton Hamiltonian yields exciton wavefunctions localized on sections of the aggregate. Dynamic disorder is typically introduced after diagonalization as exciton-phonon perturbations, leading to population relaxation and dephasing. Additionally, there are several energetically separated manifolds of states where each successive manifold consists of states with an additional excitation present. When the disorder is small compared to the intermolecular coupling, as in J-aggregates, the lowest energy states behave like those of a homogeneous aggregate delocalized over a reduced area of the full aggregate [238, 183]; these states resemble those of a particle confined in an infinite potential well. The lowest energy exciton state typically exhibits a wavefunction with no nodes, an S state; all the dipoles oscillate in phase, leading to superradiance [225]. The next highest energy state delocalized over the same molecules often contains one node (a P state) [239]. For a particle in an infinite potential well the energy difference between the S and P states reflects the size of the box. For a J-aggregate, this average energy difference, $\Delta = E_P - E_S$, reflects the average delocalization size of the exciton. The dominant optical transition from the one- to two-exciton manifold is typically from an S one-exciton state to an (approximately) SP-hybrid two-exciton state with the energy $E_P + E_S$. Third-order nonlinear spectroscopic techniques are interpreted using these lowest two manifolds of states, depicted in 5-1(c). Spectrally resolved measurements are dominated by a ground state bleach at the energy E_S corresponding to the ground state to S transition and by a blue-shifted excited-state absorption feature at the S to SP transition energy E_P. The difference in energy between these features is Δ.

The approximation that localized excitons retain properties similar to homoge-

neous, fully delocalized excitons is applicable to both one and two-dimensional J-aggregates [220]. Since we expect quasi-1D excitons in our system due to anisotropy in the intermolecular coupling, we analyze our results using a 1D model, noting that the trends we find would hold for either 1D or 2D systems (see appendix for relationships for a 2D square lattice model). The exciton energy in a homogeneous linear J-aggregate restricted to nearest-neighbor coupling is $E_k = \epsilon_0 - 2Jcos(\frac{\pi k}{N+1})$, where ϵ_0 is the uncoupled excited-state energy, J is the coupling strength, N is the total number of molecules in the aggregate, and the integer k is used to denote the (unitless) wavevector $K = \frac{\pi k}{N+1}$. Taking the energy difference between the P state ($k = 2$) and the S state ($k = 1$) and replacing the total number of molecules in the aggregate N with the effective coherence length N_{coh} leads to[63]

$$N_{coh}(E_{abs}) = \pi\sqrt{\frac{3J}{\Delta(E_{abs})}} - 1. \tag{5.2}$$

In a 2D correlation spectrum, the absorption frequency is fully resolved, allowing us to deduce the delocalization length as a function of the S exciton absorption energy, E_{abs} (5.2). A caveat is that the preceding interpretation of J-aggregate wavefunctions in terms of S and P states only holds in the low-energy tail of the density of states and that this picture does not hold for high-energy excitons.

The localization of the exciton wavefunction due to dynamical fluctuations and inhomogeneity leads to uncertainty in the exciton wavevector, and thus to uncertainty in the energy of the exciton. Expanding the homogeneous J-aggregate energy-wavevector dispersion relation above for small wavevectors K leads to a parabolic dispersion relation $E \approx \epsilon_0 - 2J + JK^2$, similar to that of a quantum-mechanical particle in a box. The uncertainty in wavevector, δK, caused by localization gives rise to uncertainty in energy $\delta E \approx 2JK(\delta K) + J(\delta K)^2$ [203]. The exciton wavevector depends on the exciton coherence length, N_{coh}. The uncertainty in the exciton wavevector depends on exciton-phonon scattering and thus on the delocalization length given by dynamic disorder, N_{del}^d. There are two temperature regimes of interest, illustrated in 5-1(a). At low temperatures, associated with infrequent dynamic scattering events,

static disorder dominates and the exciton momentum is a good quantum number such that $K \gg \delta K$. In this case N_{del}^{d} plays no role since it is much longer than the temperature-independent delocalization length controlled by static disorder, N_{del}^{s}, i.e. $N_{coh} = N_{del}^{s}$. At higher temperatures, dynamic exciton scattering events lead to localization within a smaller size, i.e. $N_{coh} = N_{del}^{d} < N_{del}^{s}$. In the high-temperature limit, the exciton momentum is no longer a good quantum number because the fluctuations in K within any region are large, i.e., $\delta K \sim K$, and $\delta E \sim |J|/(N_{coh})^2$. Identifying the high-$T$ energy uncertainty with the homogeneous linewidth of the exciton absorption spectrum, γ_{hom}, leads to

$$N_{coh} = \begin{cases} N_{del}^{s} & \text{Low } T \\ N_{del}^{d} \propto \left(\frac{|J|}{\gamma_{hom}}\right)^{\frac{1}{2}} & \text{High } T \end{cases} \tag{5.3}$$

In the model, the exciton coherence length increases as the temperature is reduced until the static delocalization length is reached, at which point N_{coh} becomes T-independent.

5.4.2 Excitons in Two Dimensions

The Frenkel exciton analysis carried out in the previous section for one dimension is easily extended to two dimensions. In the case of a rectangular lattice where each molecule lies on a grid of evenly spaced points in both dimensions with isotropic intermolecular coupling, the Hamiltonian is separable into two one-dimensional contributions, each identical to the one-dimensional Frenkel exciton Hamiltonian. This Hamiltonian becomes immediately solvable, with the wavefunctions

$$|k_1, k_2\rangle \propto \sum_{n,m} \sin\frac{\pi k_1 n}{L+1} \sin\frac{\pi k_2 m}{L+1} |n, m\rangle \tag{5.4}$$

with corresponding energies

$$E_{k_1 k_2} = \omega_0 - 2J\left(\cos\frac{\pi k_1}{L+1} + \cos\frac{\pi k_2}{L+1}\right). \tag{5.5}$$

Near the bottom of the band (small wavevector), we can make a Taylor expansion of the energies, giving

$$E_{k_1 k_2} = \omega_0 - 4J + \frac{\pi^2 J}{(L+1)^2}\left(k_1^2 + k_2^2\right). \tag{5.6}$$

The lowest energy state is the superradiant state with energy E_{11}, while the lowest energy two-exciton state is the state with energy E_{12} or E_{21}. The energy difference between these states, Δ, is determined in the 2D FTOPT experiments.

$$\Delta = \frac{3\pi^2 J}{(L+1)^2}. \tag{5.7}$$

However, in the case of a 2D lattice, the number of molecules, N_{coh}, participating in the coherence now scales with L^2 and is proportional to an area. Thus, we write

$$N_{coh} \propto \left(\pi\sqrt{\frac{3J}{\Delta}} - 1\right)^2. \tag{5.8}$$

To relate N_{coh} in 2D to the dynamic dephasing we follow the same logic as before. Using $K^2 = k_1^2 + k_2^2$ we rewrite 5.6 as

$$E_K = \omega_0 - 4J + \frac{\pi^2 J}{(L+1)^2}K^2. \tag{5.9}$$

Allowing uncertainty in the momentum, $K \to K + \delta K$, gives $\delta E \approx J(2K(\delta K) + (\delta K)^2)$, as in the 1D case. Equating δE with γ_{hom} and taking the high T limit where localization is governed by dynamic disorder results in $N \propto \frac{3J}{\gamma_{hom}}$.

5.5 Exciton Coherence Lengths and Dephasing

The thin film samples exhibited strong red-shifted and narrowed linear absorption spectra compared to the isolated dye molecules, archetypal signs of J-aggregation (Figure 5-1(d)). Representative 2D CS for BIC and U3 J-aggregate films at 9 K, 100 K and 250 with zero waiting time are shown in Figure 5-2.

The spectra for BIC (top) and U3 (bottom) show similar features, with no spectra

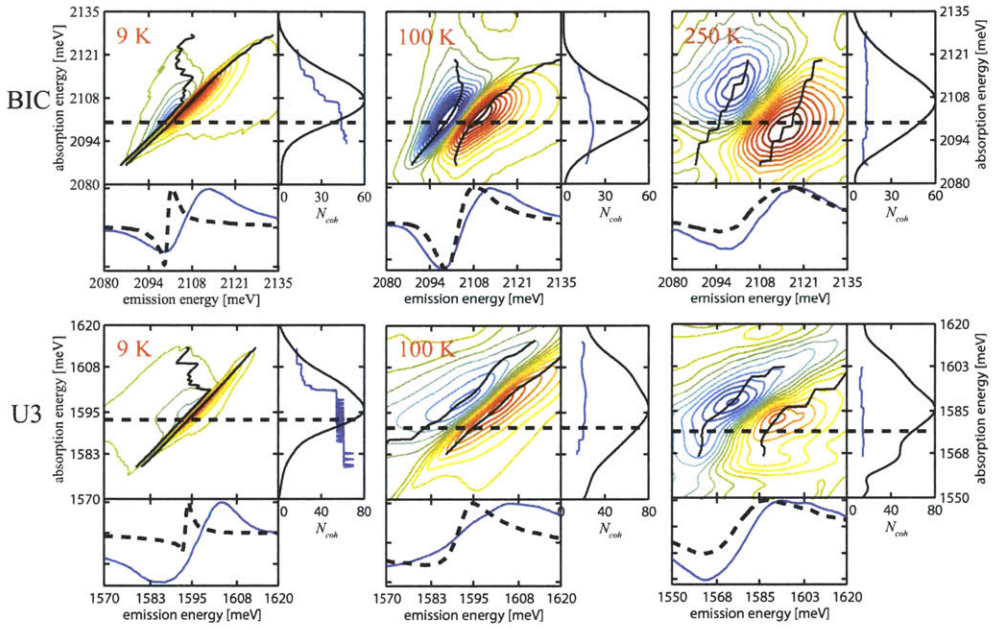

Figure 5-2: 2D CS for BIC (top row) and U3 (bottom row) J-aggregate thin films for several temperatures. Each panel presents a 2D CS with the ESA and GSB maxima as a function of energy shown and, based on the differences between them, $N_{coh}(E_{abs})$ indicated by the blue traces in the panels on the right. The heavy dashed lines indicate an exciton energy in the range used to determine the average value of N_{coh} at each T. The emission spectrum for this absorption energy is shown in the lower panel (black dashed line). Also shown are the signal projections to the emission energy axis (blue lines in lower panels) and the projection of the signal magnitude onto the absorption energy axis (black lines, right panels).

showing significant changes within the first few hundred femtoseconds of waiting time except for an overall lowering of the signal strength. The spectra blue-shifted and narrowed as temperature was decreased, similar to the temperature-dependent trends of other J-aggregates [203]. Each 2D correlation spectrum exhibits positive (red contours) and negative (blue contours) features resulting from excited-state absorption and ground-state bleach, respectively. Solid black lines on the 2D CS show the points of minimum and maximum signal used to determine the energy offset, Δ, from which the coherence length is calculated. The 1D model yielded nearest-neighbor intermolecular coupling constants of 153 meV for BIC and 212 meV for U3, estimated from the shift of the J-aggregate absorption compared to the monomer [176]. Spectrally resolved pump-probe (SRPP) spectra in Figure 5-2 (lower panels, blue lines) are given by the projection of the 2D CS onto the emission energy axis. However, at low T, the SRPP do not reflect the narrow low-temperature homogeneous linewidths. Instead, the peaks are broadened by the inhomogeneity of the films, thereby increasing the apparent separation between the bleach and excited-state absorption features and leading to an artificially decreased value for the exciton coherence length. Cuts of the 2D CS spectra at specific absorption energies (black dotted lines in Figure 5-2) demonstrate the narrow linewidths for a single exciton energy. As the temperature increases and the total lineshape becomes more homogeneous, the spectral features of excitons at different energies broaden until there is almost no difference between their linewidths and those of the SRPP spectra.

Using 5.2 for the 1D model we extracted the coherence lengths and then averaged around the red edge of the absorption peak to find a coherence length representative of the average exciton. The coherence length temperature-dependencies from 9 K to 250 K for both J-aggregate films are shown in Figure 5-3. Contrary to the expectation of the model described above, we found that the coherence length decreases monotonically over the entire temperature range.

Temperature-dependent 2D PE spectra (Figure 5-4) of both U3 and BIC J-aggregates demonstrate the changing relative contributions of inhomogeneous and homogeneous broadening to the spectral line shapes. Using a fitting procedure [234]

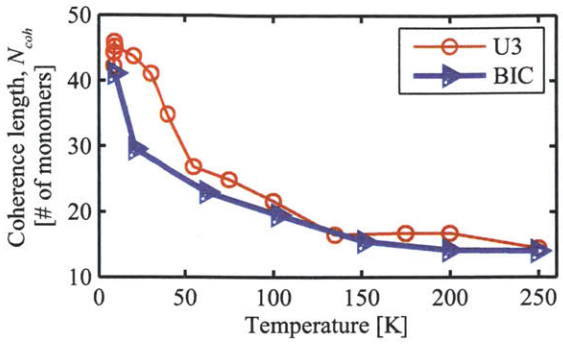

Figure 5-3: 1D model exciton coherence length as a function of temperature. The coherence length decreases monotonically for all T.

we extracted the two dephasing rates for all temperatures.

Figure 5-5 shows that for both J-aggregates, the inhomogeneous contributions are significantly larger than the homogeneous contributions at low T, while the rates become more comparable at higher T. The homogeneous linewidths for both U3 and BIC scale linearly with temperature (Figure 5-5 (bottom)), which would be expected from dephasing through single-phonon interactions with a sub-linear spectral density [202, 240]. Even though the inhomogeneous broadening σ is greater than the homogeneous broadening γ for most temperatures, N_{coh} tracks the homogeneous dephasing rate across all temperatures.

Fitting N_{coh} versus J/γ reveals that localization is controlled by dynamic scattering as described by 5.3 even down to temperatures as low as 9 K (Figure 5-6). According to 5.3, it is clear that as T is reduced the data show no transition from dynamic to static disorder-controlled delocalization length, as would be evidenced by a change in slope from -0.5 to 0 at low T where N_{coh} would become T-independent. The 2D correlation spectra shown in Figure 5-2 and collected at other temperatures, which clearly show that the difference between ESA and GSB transition energies continues to decrease with T even at the lowest temperatures, already make it clear that N_{coh} never reaches a T-independent value limited by inhomogeneity.

It is expected that the brickwork lattice has properties somewhere between the fully 1D and 2D cases due to anisotropic intermolecular coupling. The results shown in Figure 5-6 suggest primarily 1D exciton delocalization, but even a relatively small

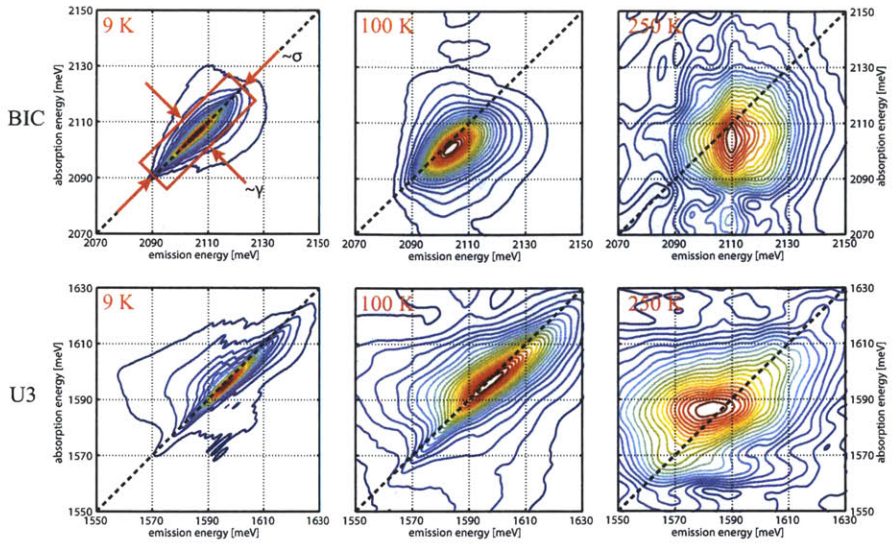

Figure 5-4: 2D PE spectra for BIC (top row) and U3 (bottom row) J-aggregates. The elongation along the diagonal indicate a large inhomogeneous dephasing rate, σ. The narrow anti-diagonal indicates a comparatively small homogeneous dephasing rate, γ. As the temperature increases from 9 K (left column) to 250 K (right column) the homogeneous dephasing rate increases, as evidenced by the increasing anti-diagonal linewidth.

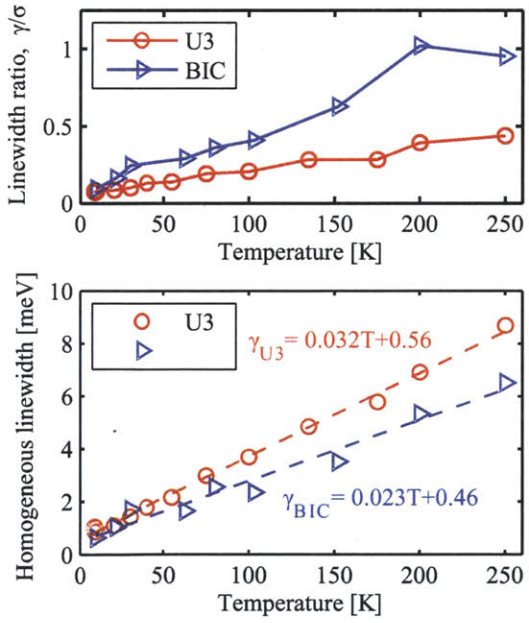

Figure 5-5: Homogeneous linewidth temperature-dependence for BIC and U3 J-aggregates. (Top) Ratio of homogeneous linewidth (γ) to inhomogeneous linewidth (σ). (Bottom) Homogeneous linewidth versus T.

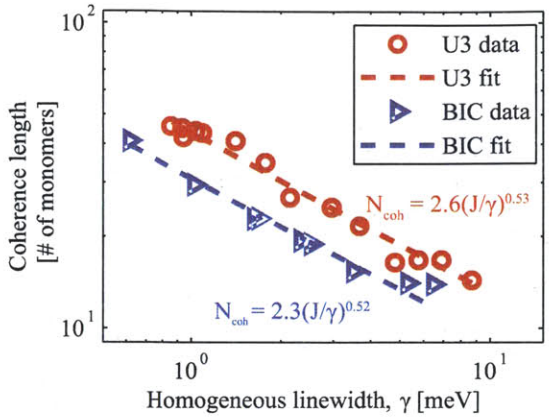

Figure 5-6: Log-log plot of coherence length versus homogeneous line width for BIC and U3 J-aggregates. The data throughout their ranges are fit well by the high temperature expression in 5.3, implying that dynamic disorder controls localization to temperatures as low as 9 K.

amount of interaction in a second dimension could significantly circumvent localization due to static inhomogeneity that is characteristic of purely 1D behavior [184]. Thus 2D electronic interactions may play a role in the absence of static disorder-induced exciton localization even at the lowest temperatures.

5.6 Conclusions

In summary, we measured and compared homogeneous and inhomogeneous linewidths and coherence lengths for two different nanostructured J-aggregate thin films using the unique capabilities of 2D FTOPT spectroscopy. We found that dynamic disorder dictates the coherent size of the excitons at all temperatures measured, down to 9 K, even in the presence of inhomogeneous dephasing that is an order of magnitude faster than the homogeneous dephasing. Thus dynamic disorder may control the exciton coherence length while static disorder controls the exciton coherence time. This is in contrast to previous reports that found a crossover temperature of $\sim$ 40 K [225, 203] below which static disorder limited the exciton coherence size. Our results suggest that if synthetic systems such as J-aggregate films with selected morphologies can be engineered with controlled exciton-phonon coupling and dimensionality

(i.e. anisotropy) of intermolecular electronic interactions, then the exciton coherence lengths may be increased accordingly, even in the presence of inhomogeneity.

Chapter 6

Morphology and Excitonics in Supramolecular Nanotubes

Highly efficient photosynthetic light harvesting antennae are ubiquitous in nature. The morphology of these pigment-protein complexes often consists of a repeated supramolecular building block whose structure determines how energy is sequestered and transported in the form of excitons. However, identification, isolation, and characterization of the building block remains a challenge due to the complexity of the natural environment. This chapter elucidates the correlation between morphology and excitonics for the supramolecular building block of artificial self-assembling nanotubes (NTs) in two hierarchical structures. Transmission electron microscopy (TEM) determined that the morphological transformation from double-wall NTs to bundles of NTs maintains the structure of the inner wall NTs, which become the repeat unit in the bundles. Linear and nonlinear spectroscopy further corroborate this conclusion by showing that the excitonic spatial orientations and correlations for the building block are relatively unperturbed by the morphological change. In addition, a microscopic model for the NT building block only requires very minor changes to reproduce the linear optical spectral changes. This insight into the relationship between morphology and excitonics is critical to future design of artificial light harvesting devices based on self-assembling nanotube systems.

The work presented in this chapter is the result of a collaboration between several

research groups. The electron microscopy was performed at Brandeis University by Xiaofeng Fu and Dörthe Eisele; the linear dichroism and nonlinear spectroscopy data was taken by myself and Colby Steiner at MIT; the oxidation chemistry results were obtained by Dörthe Eisele at MIT; and the theoretical modeling was performed by Eric Bloemsma in the Knoester group at the University of Groningen in the Netherlands.

6.1 Introduction

Natural light harvesting complexes have been studied as models for light harvesting applications due to their high efficiency in transporting solar energy in the form of excitons from absorbing antennae to reaction centers [19, 23, 20, 5, 21, 241, 31, 30, 242, 223, 13, 12, 243, 244]. The antennae and energy transportation architecture can be organized into a series of networked hierarchies [16]. At the lowest and most fundamental level are individual absorbing molecules. These chromophores are often coupled to form a supramolecular antenna complex, containing from several chromophores in, e.g. the Fenna-Matthews-Olson antenna complex [17], to hundreds of thousands of chromophores as in the chlorosomes of green sulfur bacteria [18]. The antenna complexes are further packed into networked arrays and connected to reaction centers where charge separation may occur. Each level in the hierarchy depends critically on the geometry and structure of the subunits as well as the environmental conditions, all of which determine the inter-subunit interactions and energy transfer (exciton transport) properties.

A large effort has been devoted to developing artificial light harvesting systems related to the natural complexes but reduced in complexity to allow clear elucidation of the relationships between the geometrical structure, the morphology, and the electronic (excitonic) band structure [40, 9, 14, 245, 217]. In particular, many studies have focused on different morphologies of self-assembling J-aggregates based on amphiphilic cyanine dyes [43, 44, 45, 47, 48, 40, 217]. Varying the molecular structure of the dye, the preparation conditions, and the environmental conditions lend

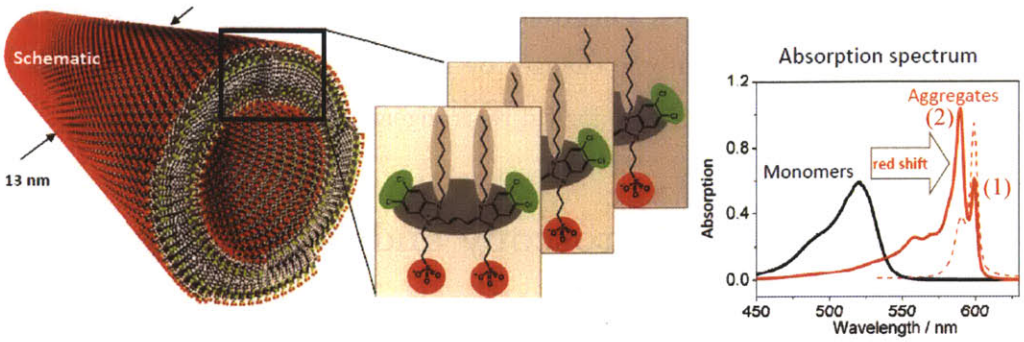

Figure 6-1: Diagram showing the structure of C8S3 nanotubes (left) composed of amphiphilic cyanine dye molecules (middle). The linear optical properties (right) show typical signs of J-aggregation, e.g. red-shifted and narrowed absorption (solid red curve) and no Stokes shift in fluorescence (dashed red curve).

a great degree of control over the aggregation process and the eventual morphology, typically imaged via cryogenic TEM (cryo-TEM) [43, 44, 45, 246]. In addition, optical spectroscopy experiments [247, 237, 248, 68, 67, 70] and microscopic modeling [218, 219, 220, 249, 221] have provided great insight into the microscopic structures of the dye aggregates and the nature of the excitons.

Here we study J-aggregates formed from 3,3'-bis(2-sulfopropyl)-5,5',6,6'-tetrachloro-1,1'-dioctylbenzimidacarbocyanine18 (C8S3) molecules. Our preparation method leads to double-wall nanotubes (NTs) (Figure 6-1) [250, 48, 217]. A qualitative structural model for the nanotubular aggregates is shown in Figure 6-1 (left), composed of the cyanine dye molecules C8S3 (middle). Hydrophobic carbon chains (light grey) and hydrophilic sulfate groups (red) drive self-assembly of a double-wall NT morphology. The transition dipoles oriented along the molecules' conjugated backbone (dark grey) arrange head-to-tail, leading to spectral signatures of J-aggregation: red-shift and line narrowing. However, unlike the J-aggregates studied in Chapter 5, here we see the appearance of multiple exciton bands. In the following sections I describe cryo-TEM experiments used to study the morphology of the double-wall NTs as well as higher-order structures composed of many NTs. A combination of linear and nonlinear spectroscopy, in conjunction with the cryo-TEM results, gives insight into the nature of the morphological and excitonic changes between the double-wall NTs and

the higher-order structures. Finally, a microscopic model for the NTs is able to qualitatively explain the excitonic changes by incorporating slight perturbations to the NTs to account for the morphological rearrangement.

6.2 Electron Microscopy and Linear Spectroscopy

We used cryo-TEM to study the morphology of the different NTs. Electron tomography (ET) cryo-TEM gave further insight to the three-dimensional structure of the higher-order morphology. We directly correlated each morphology with a specific absorption spectrum to study the optical properties of the two morphologies independently.

6.2.1 TEM of Supramolecular Nanotubes

Cryo-TEM for double-wall NTs (Figure 6-2(a)) matches previous results [48] with inner wall diameters of 6 nm, outer wall diameters of 13 nm, and interwall separation of 3-4 nm consistent with the lengths of the C8S3 carbon side chains. The bundled morphology (Figure 6-2(b)) is more disordered than the isolated NTs in that there are differences between bundles. Anywhere from 6-12 nanotubes make up a bundle, and some bundles are twisted (at different twisting angles) or exhibit curvature along the length of the bundles. Cryo-TEM is insufficient to determine the three-dimensional structure of the bundles because it is a two-dimensional projection technique. However, a series of cryo-TEM images taken at different angles between the electron beam and the sample plane allows reconstruction of the 3D structure; this procedure is known as electron tomography (ET). Figure 6-2(c) shows the reconstructed ET cryo-TEM image of bundled nanotubes, showing a straight and twisted morphology (left and right, respectively). Figure 6-2(d) shows a slice taken from the ET cryo-TEM showing the end-on perspective. The resolution is not high enough to resolve individual walls, but the average center-to-center distance of 9 ± 1 nm is not consistent with bundles of 13 nm double-wall NTs. However, the center-to-center distance *is* consistent with solely inner walls packed together. A qualitative schematic

illustration of this morphology is shown in (e). The carbon side chains on each C8S3 (light gray) effectively separate the conjugated backbone of the chromophores by 3-4 nm.

An outer wall layer (not pictured) is still required to protect the outermost NTs' carbon side chains from the surrounding aqueous solution. However, due to the inhomogeneity between bundles, it is clear that the outer wall layer will be highly inhomogeneous as well. This would break up the intermolecular interactions driving the coherent optical response, including the large red-shift and line narrowing. Therefore, we expect the outer wall contribution to the optical properties to be a broad, low intensity, higher energy feature that does not necessarily resemble a typical J-band because of the high degree of disorder.

Double-wall NTs give the isotropic absorption spectrum in Figure 6-2(f) in red, with five labeled exciton bands. Peaks (1) and (2) were previously assigned to the inner and outer wall, respectively, while peaks (3)-(5) have significant contributions from the inner wall and possibly from the outer wall as well [217]. The bundled NT optical spectrum (Figure 6-2(f), blue) consists of two peaks (I) and (II). Peak (I) is red-shifted compared to (1) in double-wall NTs, and (II) is slightly blue-shifted compared to (3) of the double-wall NTs. Because each morphology gives rise to a distinct absorption spectrum, we can use the optical properties as sensitive probes of not only the presence of each morphology but also the excitonic band structure of each morphology.

6.2.2 Polarized Linear Spectroscopy

We investigated the excitonic band structure in more detail using linear dichroism spectroscopy. Due to the small diameter and large length (hundreds of nm) of the NTs, when a solution containing the NTs flows through a narrow cuvette ($0.05 - 0.20mm$) the NTs align with the long axis pointed along the direction of flow [250]. Polarized light will preferentially absorb either parallel (H) or perpendicular (V) to the the flow axis, according to the excitonic selection rules (see Chapter 4). Ideal NTs have perfect dipolar alignment either parallel or perpendicular to the longitudinal axis.

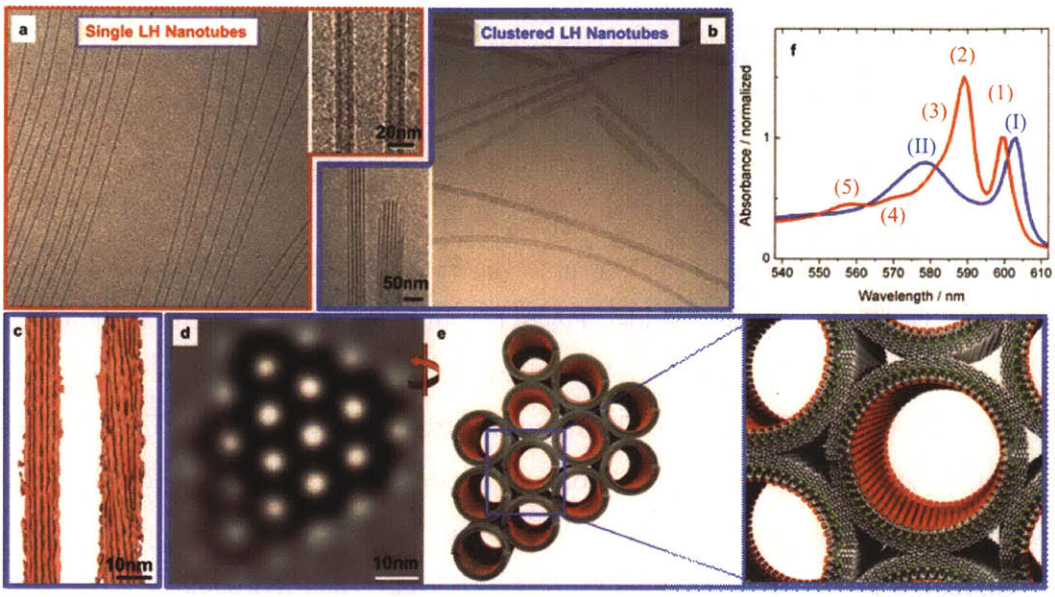

Figure 6-2: (a) Double-wall LHNs cryo-TEM. (b) Bundled NTs cryo-TEM. Several different structures exist with different twisting angles and curve angles. (c) ET cryo-TEM allows reconstruction of structure for straight (left) and twisted (right) bundles. (d) Slice taken from ET for average twisted NT. (e) Qualitative schematic of bundled morphology, with inner wall providing the building block for bundle. The surrounding outer wall layer is not pictured. (f) Isotropic linear absorption spectra for double-wall NTs (red) and bundled NTs (blue).

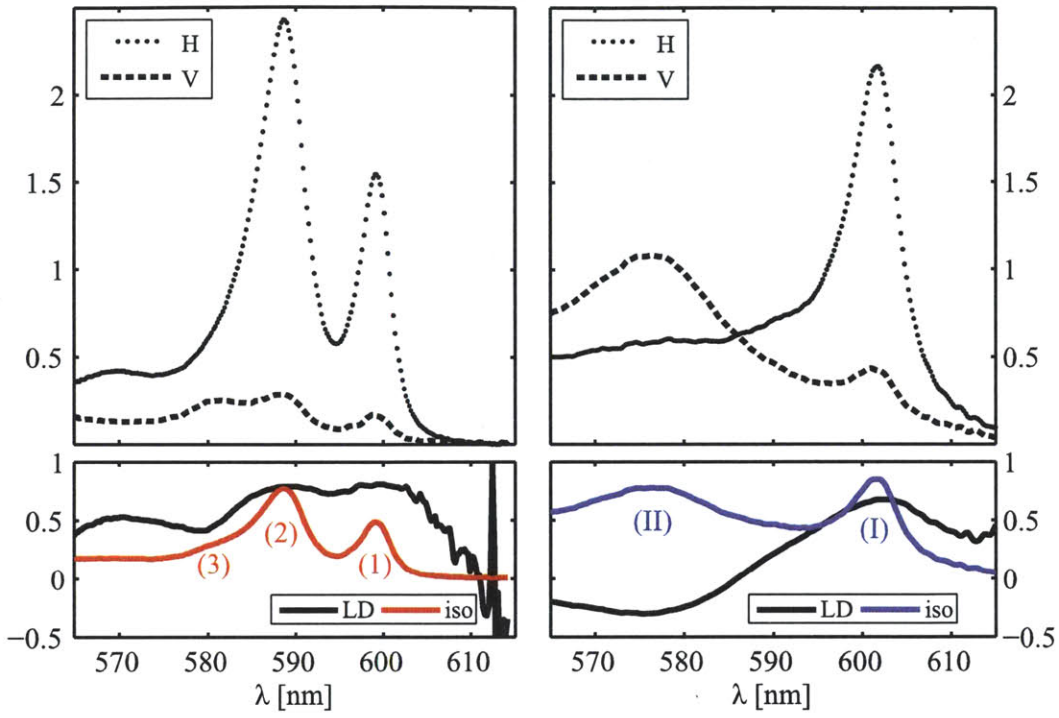

Figure 6-3: Linear dichroism for double-wall NTs (left) and bundled NTs (right). Top panels show absorption polarized parallel (H) and perpendicular (V) to the flow direction while bottom panels show the reduced linear dichroism (Equation 6.1) and isotropic linear absorption.

However, due to disorder these optical selection rules are relaxed [221]. In addition, there is no guarantee experimentally that the longitudinal NT axis is pointed exactly along the flow direction. The degree of orientation is given by the reduced linear dichroism, LD_r, defined as the difference between the H-polarized absorption A_H and the V-polarized absorption A_V divided by their sum,

$$LD_r = \frac{A_H - A_V}{A_H + A_V}. \tag{6.1}$$

According to Equation 6.1, LD_r is $+1$ when the transition is perfectly aligned along the flow direction, -1 when exactly perpendicular to the flow direction, and 0 when the transition is either isotropic or polarized at 45 degrees with respect to the flow direction.

Even with disorder and imperfect NT alignment, the exciton transitions are still

highly aligned along the flow direction (Figure 6-3). Peaks (1) and (2) of the double-wall NTs, previously assigned to the inner and outer walls, respectively, are both oriented parallel to the long axis of the NT. In the vicinity of peak (3), which has a strong contribution from the inner wall, the LD_r experiences a dip only to recover at lower wavelength. This could indicate that peak (3) is somewhat perpendicularly polarized but the LD_r is affected by the surrounding peaks in this region. Peak (3) could then be the perpendicular peak predicted by the theory in Chapter 4 for the inner wall.

The bundled NT LD_r exhibits a highly polarized peak (I), similar to (1) of isolated tubes. Peak (II) is clearly polarized perpendicular to nanotube axis, following the theory laid out in Chapter 4 with parallel and perpendicular peaks. Considering peaks (1) and (3) from the inner wall in double-wall NTs and comparing to the bundled NTs peaks (I) and (II) there is a similarity in terms of relative absorption amplitudes and relative peak positions. This suggests that the bundled NTs spectrum is derived predominantly from single-walled NTs, specifically the inner wall from the double-wall NTs. This corroborates the analysis of interwall distances from the ET cryo-TEM data.

However, linear dichroism spectroscopy does not provide direct insight about the relationships between different excitons. For example, there is no definitive evidence that exciton (3) in the double-wall NTs is from the inner or outer wall. However, two-dimensional electronic spectroscopy experiments will be able to correlate directly exciton (3) with either excitons (1) or (2), whose supramolecular origins were previously assigned. Therefore, these experiments will determine the supramolecular origin of exciton (3).

6.3 2D Spectroscopy of Nanotubes

Two-dimensional electronic spectroscopy (2D ES) has been used to elucidate interactions and dynamics in both natural light harvesting complexes [20, 21, 30, 223, 242, 251, 252, 253, 254, 255, 256, 244, 243, 257] and J-aggregate complexes similar

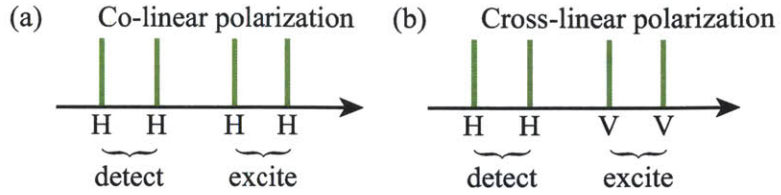

Figure 6-4: (a) Co-linear (HHHH) excitation and detection scheme. Excitation and detection pulses (green) are H polarized. (b) Cross-linear (HHVV) excitation and detection scheme. Excitation pulses are V polarized while detection pulses are H polarized.

to those studied here [185, 248, 66, 65, 64, 68, 67, 69, 70, 222]. In this section, 2D ES experiments report directly and straightforwardly on the excitonic coupling and coherence in both NT morphologies, and on a solution containing both species. The linear dichroism results discussed in the previous section revealed important polarization selection rules, allowing discrimination between different excitons and their interactions. In addition to the selection rules, NT alignment in a flowing solution offers a significant advantage over typical polarization-controlled 2D ES experiments [258, 119, 244]. Isotropic averaging, as is the case in most sample solutions, obfuscates 2D ES signals, requiring complicated polarization schemes for the excitation pulses to extract relevant information. In our aligned samples, simple and straightforward H and V polarizations for the excitation pulses offered an intuitive method to reveal the excitonic couplings of interest.

Two polarization schemes were used. Co-linear excitation (HHHH, Figure 6-4(a)) focuses on H-polarized excitons and reveals excitonic coherence between excitons (1) and (2) in the double-wall NTs, i.e. the interwall coupling. However, co-linear excitation does not report on the coupling strength to peak (3) because it is V polarized. Similarly in the bundled NTs, HHHH does not report on the coupling between excitons (I) and (II) as they are perpendicularly polarized with respect to one another. A cross-linear excitation scheme HHVV (Figure 6-4(b)) directly reveals coherences between perpendicular excitons because a V polarized exciton is initially excited and an H polarized exciton is probed. HHVV 2D ES experiments report on the coupling strength between excitons (I) and (II) in the bundled NTs and between exciton (3)

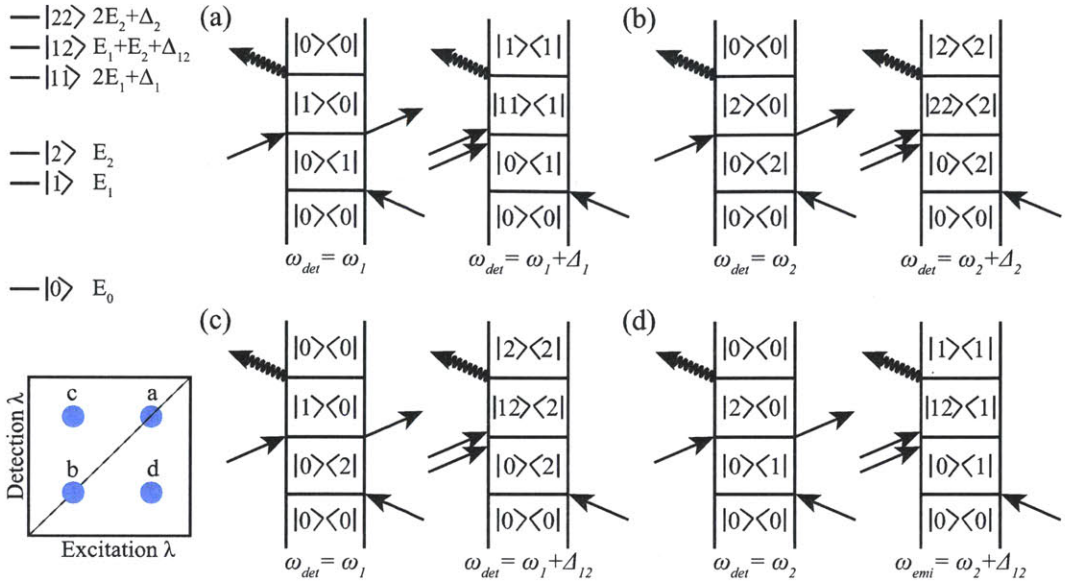

Figure 6-5: Energy level diagram (upper left), Feynman diagrams (excluding ground state bleach) (a)-(d), and schematic illustration of expected HHHH 2D ES photon echo signal for double-wall nanotubes (lower left). Each peak in the 2D ES experiment contains signals from the corresponding Feynman pathways due to stimulated emission and excited-state absorption.

and either (1) or (2) in the double-wall NTs.

The contributing photon echo signals to the different polarization experiments are more clearly enumerated in Figures 6-5, 6-6, and 6-7. The nonrephasing contributions show similar features and are not displayed. The 2D ES photon echo Feynman diagrams for the double-wall HHHH experiment (Figure 6-5) contribute to four expected peaks, two along the diagonal and two cross peaks indicating excitonic coupling. Each peak has two contributions, a stimulated emission (and ground state bleach, Feynman diagrams not shown) and excited-state absorption at slightly blue-shifted detection energy, due to the blue-shifting of the double-excited states in J-aggregates [259, 260, 261]. Exciton (3) does not contribute to this spectrum because its contribution is negligible for H excitation and detection polarization conditions.

The Feynman diagrams and expected signals for the double-wall HHVV 2D ES experiment are shown in Figure 6-6, assuming that exciton (3) is coupled to both excitons (1) and (2). Exciton (3) *does* contribute to this set of signals, leading to

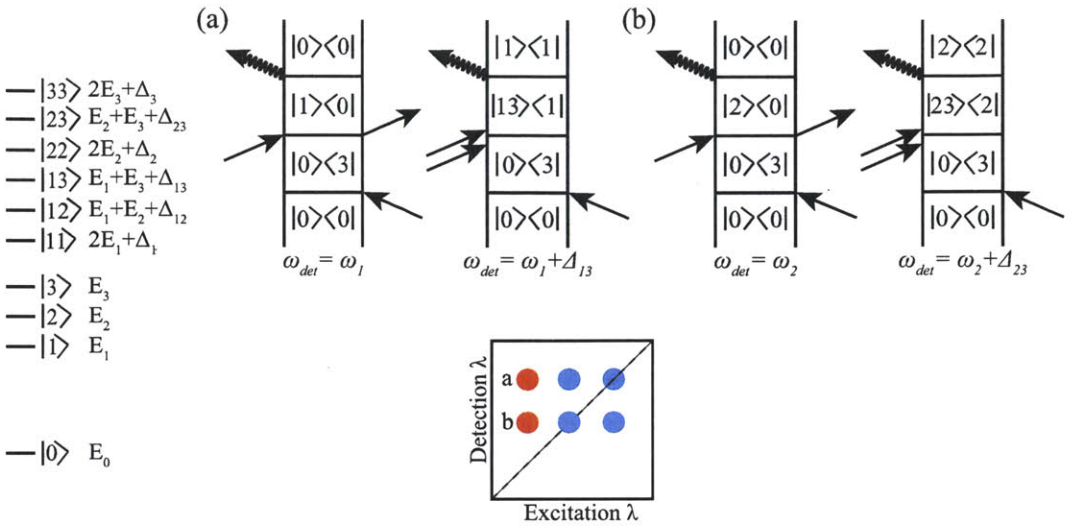

Figure 6-6: Energy level diagram (left), additional Feynman diagrams (excluding ground state bleach) (a) and (b), and schematic illustration of expected HHVV 2D ES photon echo signal (bottom). Illustrated are the four previous peaks (blue), and two new peaks (red) that are highly sensitive to exciton coupling between exciton (3) and excitons (1) and (2).

four additional pathways in addition to the eight illustrated in Figure 6-5. The other pathways associated with exciton (3), e.g. its diagonal peak, are excluded because of the polarization conditions discriminating against detecting emission from exciton (3). The new pathways are highly sensitive to exciton coupling between excitons (1) and (2) and exciton (3), and are enhanced with this polarization scheme compared to VVVV.

Figure 6-8 displays the polarization-controlled 2D ES results (magnitude, top, and real part, bottom) for HHHH and HHVV excitation conditions, with the excitation wavelength along the horizontal axis and detection wavelength along the vertical axis. Each spectrum is constructed from the addition of the photon echo and nonrephasing signals, giving signals with purely absorptive and dispersive real and imaginary components, respectively [122]. Additionally, the relevant linear absorption spectrum (H or V polarized) is displayed, depending on the excitation and detection polarizations. HHHH for double-wall LHNs is displayed in the left-hand column. Similar to the H polarized linear dichroism, peaks (1) and (2) are the dominant contributors to the

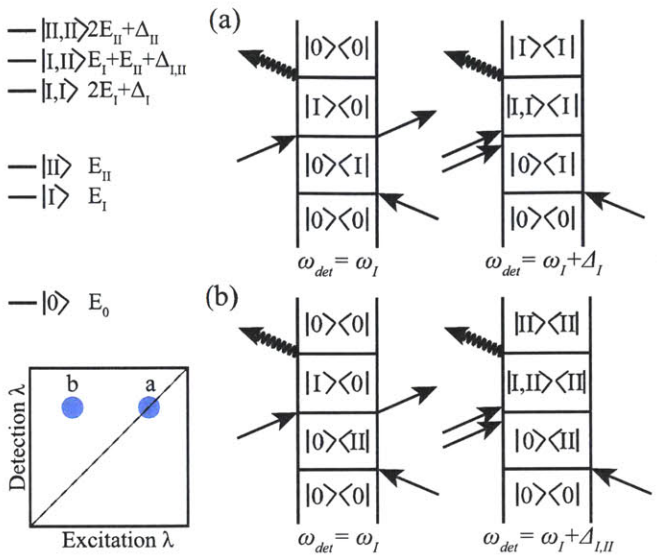

Figure 6-7: Energy level diagram (upper left), additional Feynman diagrams (excluding ground state bleach) (a) and (b), and schematic illustration of expected HHVV 2D ES photon echo signal (lower left). Illustrated are the four previous peaks (blue), and two new peaks (red) that are highly sensitive to exciton coupling between exciton (3) and excitons (1) and (2).

optical properties. In the magnitude spectrum there are three clear peaks: two diagonal peaks for (1) and (2) and a small cross peak between (1) and (2). The small cross peak signifies weak interwall coupling, which is consistent with the large interwall distances of 3-4 nm. In the real part, ground state bleach and stimulated emission (SE) are evident in both diagonal peaks with negative amplitude, interfering with excited-state absorption (ESA), which has a positive amplitude. The ESA peaks are blue-shifted with respect to the SE peaks, consistent with other J-aggregate nonlinear spectra [259, 260, 261]. The ESA and SE contributions lead to destructive interference at the location of the second expected cross peak, causing it to have significantly reduced intensity compared to the first cross peak.

The HHVV 2D ES result for double-wall NTs (middle column) shows similar diagonal features as HHHH. While excitons (1) and (2) are strongly H polarized, their relative V-polarized absorption is similar to exciton (3). Exciton (3) does not contribute a diagonal peak because the detection conditions are still for H polarized transitions,

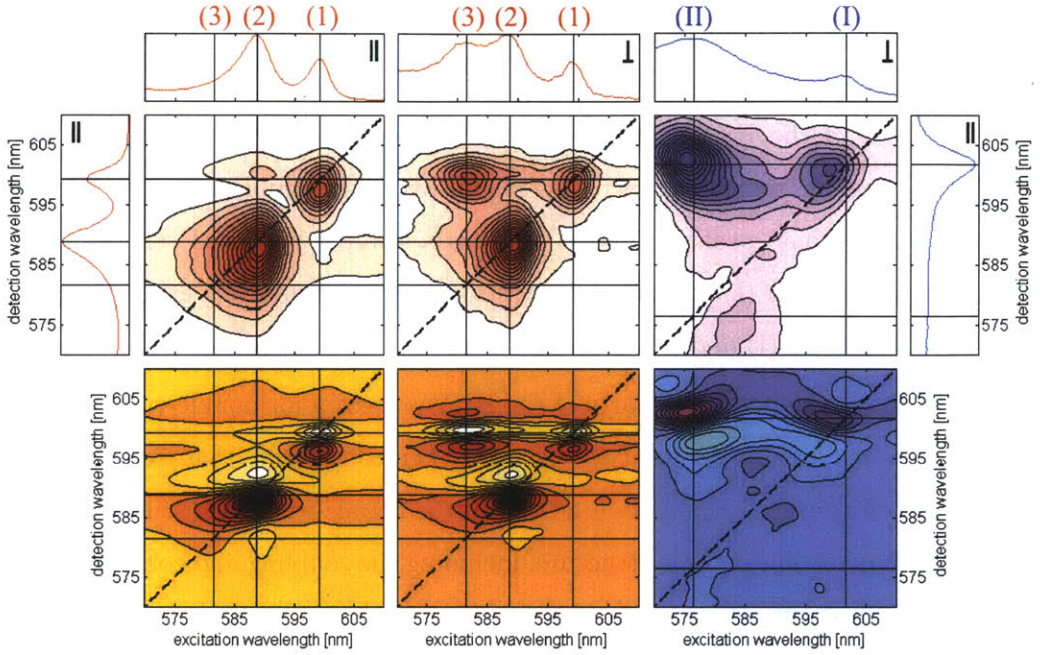

Figure 6-8: 2D ES of nanotubular aggregates with magnitude (top) and real parts (bottom). Left column shows HHHH spectrum of double-wall NTs, with the corresponding H polarized absorption spectra for excitation and detection. The middle column shows the HHVV spectrum for double-wall NTs, with the corresponding V polarized absorption for excitation. The appearance of a strong cross peak indicates excitonic coherence. The right column shows the HHVV spectrum for bundled NTs, which shows a remarkable similarity to the structure of the spectrum for peaks (1) and (3) from the double-wall NTs.

discriminating against emission from exciton (3). A new intense cross peak between excitons (1) and (3) demonstrates that those excitons are indeed strongly coupled and part of a single excitonic system. This is strongly indicative that those excitons emanate from the same molecules composing the inner wall of the double-wall NTs. In the real part of the HHVV spectrum, the (1)−(3) cross peak exhibits both SE and ESA, indicating a shared double-excited state for excitons (1) and (3). This double-excited state indicates the presence of a correlation when excitons (1) and (3) are simultaneously excited.

Analysis of the HHVV spectrum for excitons (I) and (II) in the bundled NTs follows a similar logic as for excitons (1) and (3) in the double-wall NTs. Exciton (I) exhibits a diagonal peak because it still has a small V polarized contribution. The cross peak between (I) and (II) is very strong, indicating strong excitonic coherence and that excitons (I) and (II) originate from the same molecules.

The magnitude and real parts of the HHVV spectra for double-wall and bundled NTs show remarkable similarity, especially when considering that exciton (2) comes from the effectively decoupled outer wall of the double-wall NTs. This demonstrates that the inner wall excitonic structure, including the coupling and coherence, remains relatively unperturbed upon the change in morphology.

The final experiment discussed in this section is 2D photon echo spectroscopy of a mixed solution containing both double-wall and bundled NTs. The linear absorption spectrum (Figure 6-9(a)) shows the typical bundled spectrum as well as a small yet not insignificant contribution from double-wall NTs. Peak (1) is hidden under the envelope of the dominant peak (I) contribution. The 2D ES experiment had co-linear excitation at an angle between V and H allowing a strong contribution from all the excitons. The diagonal peaks for excitons (I), (2), and (II) are clearly evident, as well as the cross peak between (I) and (II). However, there are no indications of cross peaks between exciton (2) and either excitons (I) and (II), demonstrating that they are decoupled electronic systems. This should also hold for exciton (1), inner wall excitons, because they are even further separated and screened by the outer wall from potential interactions with the bundled NTs. This shows that the two morphologies

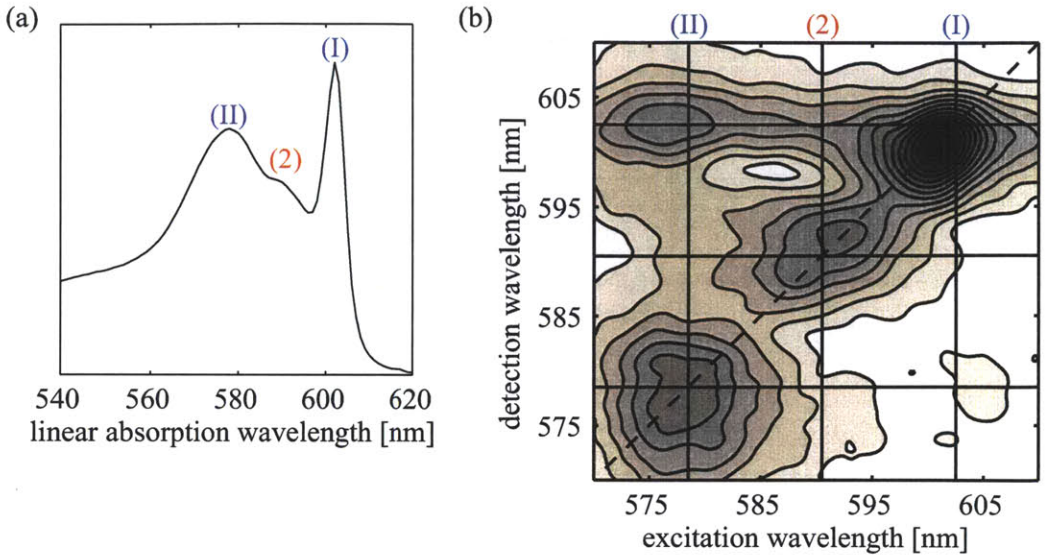

Figure 6-9: (a) Linear absorption of mixed sample. (b) Magnitude 2D ES of mixed sample.

in solution exist as electronically (and excitonically) independent systems, and that as far as we can determine with optical spectroscopy, there is no metastable intermediate state.

6.4 Microscopic Model for Isolated Inner Wall

Having identified the inner wall as an essential building block in both the double-wall and bundled NTs, it is useful to isolate its contribution to the optical properties. The addition of silver nitrate to a solution of either double-wall or bundled NTs selectively oxidizes the outer wall layer, leaving the inner wall relatively intact both morphologically and excitonically [48]. Immediately after adding silver nitrate the absorption spectra reveal the decrease of the oscillator strength for the NTs. For the double-wall NTs, peak (2) decreased much more quickly than the other exciton peaks. The remaining spectrum (Figure 6-10(a), dark green), which continued to decrease in amplitude but not change in shape, is the spectrum of the inner wall. When the bundled NTs are oxidized there is no change in shape in the absorption spectrum, just a monotonic decrease in amplitude, implying a single species is responsible for

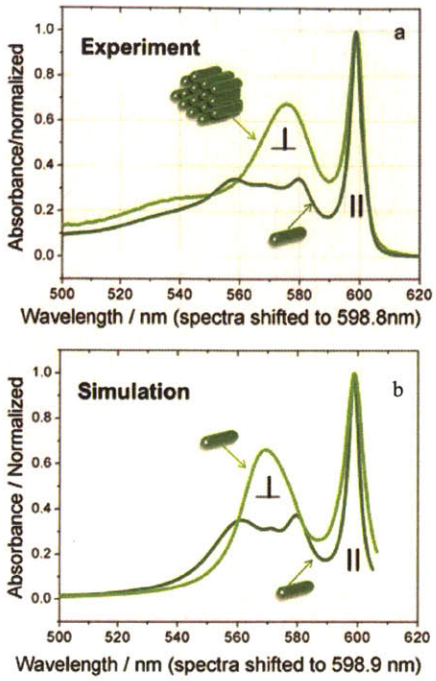

Figure 6-10: (a) Oxidation of outer-wall layer leads to spectrum for double-wall nanotubes without peak (2) (dark green) while clustered spectrum remains relatively unchanged (light green). (b) Extended herringbone model reproduces the experimental absorption spectra using only slight changes to molecular geometry.

the optical properties (Figure 6-10(b), light green).

Microscopic modeling utilizing an extension of the model introduced in Chapter 4 [217] successfully explains the qualitative spectral differences between the isolated inner wall of the double-wall NTs and the bundled NTs. The so-called extended herringbone model treats each molecule as an extended dipole rather than point dipole and has two molecules per unit cell instead of one. The calculated isolated inner wall absorption spectrum in the presence of the oxidized outer wall is shown in Figure 6-10(b), dark green. By slightly perturbing the intermolecular angles and distances in the extended herringbone model without altering the size or dipole of each molecule or altering the overall shape and size of the nanotube, the bundled NT absorption spectrum can be successfully reproduced. This demonstrates that the same morphology, with minor microscopic changes, can explain the observed excitonic properties and relationships.

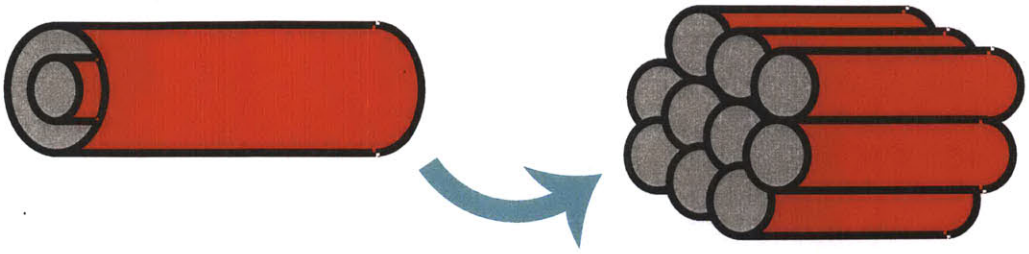

Figure 6-11: Proposed transformation for nanotubular J-aggregates studied in this thesis chapter. The double-wall NTs turn into bundles of the inner wall NT surrounded by an inhomogeneous, ill-defined outer wall (not pictured).

6.5 Conclusions

In this chapter I showed that by using a combination of electron microscopy and linear and nonlinear spectroscopy we followed the evolution of excitonic band structure upon a seemingly fundamental change in morphology. A detailed analysis of the microscopy and spectroscopy data revealed that a singular building block, a light harvesting nanotube of diameter 6 nm, exists in both morphologies and in fact remains relatively intact both geometrically and excitonically after the morphological rearrangement.

Additional analysis of the 2D ES data is underway, including modeling the excitonic system using a coupled anharmonic oscillator model [65] for the excitons. It also may be possible to extract the exciton delocalization size using a similar procedure to Chapter 5. However, several assumptions must be made about the nature of the excitons regarding the dimensionality and helicity of the wavefunctions.

Chapter 7

Quantum Process Tomography of Supramolecular Excitons

Multi-chromophoric systems such as those discussed in the previous chapters are inherently *quantum* systems featuring non-trivial interactions not only with one another but among underlying subunits which interact with one another and with the surrounding environment. The interplay of intra-system, inter-system, and system-environment interactions demands non-trivial interpretation of dynamical nonlinear spectroscopy experiments, making it difficult to gain insight into coherent and dissipative electronic energy processes. Even in multi-dimensional spectroscopy experiments, each peak in a spectrum may have various interfering contributions from, e.g., population relaxation, coherence transfer, and wavepacket propagation.

The general approach for understanding nonlinear spectroscopy experiments typically involves quantum-mechanically modeling the system, the environment, and the system-environment interactions that lead to the dynamics of interest [25]. While highly successful, this approach has drawbacks when the system and environment and their interactions become complicated and congested, as is the case for most multi-chromophoric systems. It can be difficult to separate cleanly the system from environment degrees of freedom, and to assess which approximations are appropriate when modeling the system-environment couplings. This opens the possibly of model-dependent dynamics extracted from the experiment which may risk misinterpretation

of dynamics.

A different approach to understanding quantum processes comes from the quantum information field: quantum process tomography (QPT) [262, 263, 264]. In QPT, experiments are designed to reveal distinct signatures of any quantum process by full determination of the quantum state of the system over time, i.e. the time-dependent density matrix $\rho(t)$. There is no possibility of model-dependent dynamics because the dynamics are extracted unambiguously from experiments. Using an appropriate model for the system, obtained from, e.g. the linear absorption, the time-dependent effects of system-environment interactions on the quantum state of the system are directly determined, unlike spectroscopy experiments that have overlapping signatures of the interactions. This has been accomplished for various systems, including spins, qubits, and ions [265, 266, 267], revealing key information about quantum processes in these systems. However, QPT has never been performed on molecular or supramolecular systems. This chapter details results on the application of QPT to supramolecular double-wall light harvesting nanotubes (DW-LHNs), clearly revealing excitonic relaxation and dissipation processes.

7.1 Quantum Process Tomography Methodology

In this section I introduce the general QPT methodology and work through a specific example for a two-level system modeled with Redfield theory. Next I analyze signal contributions for a coupled exciton model and describe how typical nonlinear spectroscopy approaches offer congested dynamical signals while the QPT methodology is able to separate the different processes.

7.1.1 Basic Method

The QPT methodology completely determines the time-dependent quantum state i.e. $\rho(t)$, completely independent of a model for the system-environment interactions that result in dynamics such as energy transfer or relaxation; only a model for the system is required. All dynamical information is contained in a process matrix $\chi(t)$, which

describes how $\rho(t)$ evolves over time in an intuitive and straightforward manner. $\chi(t)$ is unrelated to the nonlinear susceptibility described in Chapter 2, and only has a single time variable with no dependence on any light fields. The evolution of ρ is determined by a linear transformation acting on the initial quantum state [262],

$$\rho(t) = \chi(t)\rho(0). \tag{7.1}$$

$\chi(t)$ contains all the dynamical information about Hamitonian and system-bath interaction. In the basis of the states of the system, Equation 7.1 reads

$$\rho_{ab}(t) = \sum_{c,d} \chi_{abcd}(t)\rho_{cd}(0). \tag{7.2}$$

Each element of χ represents the time-dependent probability that a quantum state cd has amplitude transferred to another quantum state ab. For example, the element χ_{aaaa} is proportional to the population in state a and χ_{abab} is proportional to the coherence ab. Population transfer, i.e. energy transfer, between an initial state i and final state f is proportional to the elements χ_{ffii}.

A two-level system (low-energy state b, high-energy state a) at zero temperature analyzed with Redfield theory provides a simple example of what the elements of the process matrix represent. With the Markov and secular approximations, Redfield theory only describes dephasing and population transfer between states a and b. The Redfield equations for the density matrix are

$$\begin{aligned} \dot{\rho_{ab}}(t) &= -i\omega_{ab}\rho_{ab}(t) - R_{ab,ab}\rho_{ab}(t) \\ \dot{\rho_{aa}}(t) &= \sum_{b} \Big(R_{aabb}\rho_{bb}(t) - R_{bbaa}\rho_{aa}(t) \Big). \end{aligned} \tag{7.3}$$

The first line in Equation 7.3 governs the time-dependence of coherence between a and b while the second governs the time-dependence of the populations. Assuming initial population in a and integrating Equations 7.3 leads to the non-zero elements of $\chi(t)$,

$$\chi_{aaaa}(t) = e^{-(\sum_b R_{bbaa})t}$$

$$\chi_{bbaa}(t) = 1 - e^{-R_{bbaa}t}$$

$$\chi_{abab}(t) = e^{-i\omega_{ab}t - R_{abab}t}. \tag{7.4}$$

$$\tag{7.5}$$

χ_{aaaa} is proportional the probability that population in state a remains in state a and contains a sum over the Redfield tensor elements R_{bbaa}, which are the transfer rates from a to b. Therefore, $\sum_b R_{bbaa}$ is the total population transfer rate out of state a and the probability of remaining in a (χ_{aaaa}) depends exponentially on this total rate. $\chi_{bbaa}(t)$ is the probability that population has transferred from a to b. At $t = 0$, $\chi_{bbaa}(t)$ is zero because there has not been any time for population transfer to occur; however, as time increases eventually all the population transfers from a to b and $\chi_{bbaa} = 1$, meaning that the probability is 100% that population transferred from a to b. This model neglects all other population loss properties, including relaxation to the ground state, requiring all the population to eventually end up in the lowest energy state, b. The third line in Equation 7.5 governs dephasing of the ab coherence and has an oscillatory component whose frequency is given by the energy difference between a and b. The rate of decay of the amplitude of $\chi_{abab}(t)$ is the dephasing rate.

Experimental implementation of QPT requires a method to prepare selectively states of a system (either coherences or populations) and then detect subsequent states after a controlled transfer time. Previous work proposed using third-order nonlinear spectroscopy to implement QPT specifically for excitonic systems [268, 269, 270, 264]. Figure 7-1 shows the relevant third-order spectroscopy Feynman diagrams for a generic set of excitons I and O with double-excited states f; the model system will be elaborated in the following section. Using narrowband femtosecond pulses ($\sim$ 100 fs) gives frequency selectivity when preparing specific states while maintaining reasonably high time resolution. In the transient grating measurements of interest here, the first two crossed, time-coincident pulses prepare the initially excited state

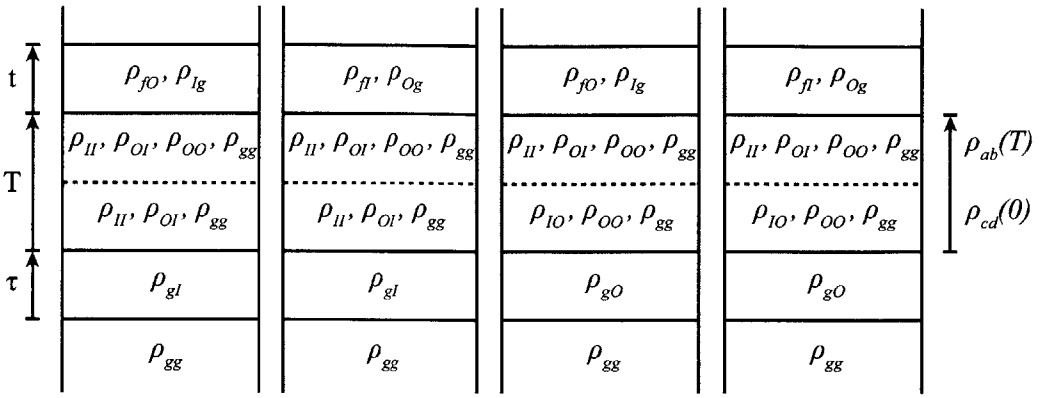

Figure 7-1: Relevant Feynman diagrams for QPT-designed transient grating experiments. The initially prepared state ρ_{cd} is prepared by the action of the first two fields. During the time between the second and third fields, T, this state may evolve to a subsequent state ρ_{ab}. The final state is detected and characterized via a combination of the third (probe) field and the emission.

through their action on the bra and ket of the equilibrium density matrix. The prepared state freely evolves during the time interval T under the influence of the system-environment interactions. Transfer processes such as dephasing, intraband population transfer, radiative and non-radiative decay, and coherence transfer all occur during the free evolution, producing subsequent states. These states are converted to emissive coherences by the third (probe) pulse. The photon energy of the third pulse determines the emission energy of the diffracted signal and therefore which final state is detected.

However, each pulse sequence on its own is insufficient to separate fully elements of χ. Process matrix elements such as χ_{OOOO} and χ_{IIOO} both contribute to experiments that prepare the initial state ρ_{OO}. The detection stage may be unable to discriminate between Feynman diagrams where the population did not change and those where it did. The solution is to use a combination of experiments to extract the process matrix. The next section demonstrates this procedure using a specific "V-level" model.

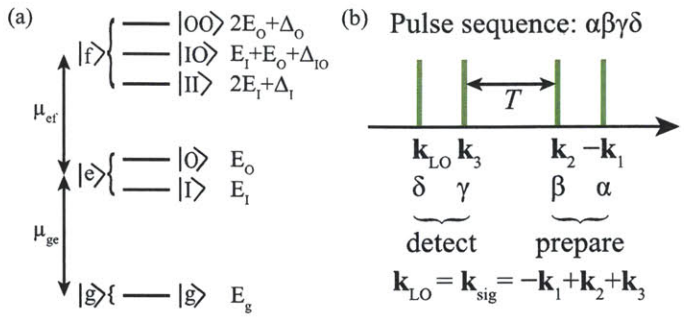

Figure 7-2: (a) Energetic scheme for V-level excitonic system. Radiation couples the ground state $|g\rangle$ to single excitons $|e\rangle$, which are also coupled to double-excitons $|f\rangle$. Energies are listed to the right of the corresponding eigenstates. (b) General QPT pulse sequence illustrating the labeling scheme.

7.1.2 Example V-Level Excitonic System

The "V-level" energy diagram is shown in Figure 7-2. There are a ground state, two single-exciton states $|I\rangle$ and $|O\rangle$, and three combination double-exciton states $|II\rangle$, $|IO\rangle$, and $|OO\rangle$. The interaction strengths between single excitons are reflected in the binding energies Δ of the double-exciton states, similar to anharmonicities in vibrational spectroscopy [212, 213].

As long as Δ is small compared to the bandgap there are only two transition energy ranges of interest, near $E_I - E_g$ and $E_O - E_g$. Each pulse can be resonant with either energy, and with four total pulses this gives sixteen possible experiments: $IIII$, $IIIO$, $IIOI$, etc. Each pulse is labeled with I or O, corresponding to its center wavelength (see Figure 7-2). In the nonlinear experiments we set $\tau = 0$ so that the prepared state is unambiguously set to $\rho_{\alpha\beta}(= \rho_{II}, \rho_{IO}, \rho_{OI}, \rho_{OO})$ by the resonant interactions with the first two fields. We leave the local oscillator pulse broadband in order to detect the emission via spectral interferometry (see Chapter 2). This has the additional advantage of collecting $\alpha\beta\gamma I$ and $\alpha\beta\gamma O$ simultaneously as the broadband local oscillator allows collection of emissions from both experiments. Therefore, the number of required experiments is halved to eight. This does not affect the QPT pulse sequences because the local oscillator is simply a reference pulse used to collect the nonlinear signal and does not play a role in *generating* the signal. Using a broadband

pulse for any of the three excitation pulses would lead to ambiguous state preparation and detection. In the following sections the pulse sequence labels are shortened to $\alpha\beta\gamma$.

The sixteen independent nonlinear signals (eight experiments) match the number of matrix elements contained in χ_{abcd}, with $a, b, c, d \in I, O$. Each signal is composed of a linearly independent combination of χ elements which means conversely that each χ element is a linear combination of experimental signals. To demonstrate this I focus the rest of this section on two of the eight experiments, designed to look specifically for coherent dynamics and population relaxation, OIO and OOI, respectively. Figure 7-3 shows relevant Feynman diagrams for OIO and OOI if there are no transfer events during the waiting time. The full set of Feynman diagrams for all eight experiments can be found in Appendix A. The first two pulses in OIO prepare an excitonic coherence that freely propagates during the waiting time T. The third pulse either stimulates emission, leading to emission at E_I, or promotes a transition to the combination band state $|IO\rangle$, with emission energy $E_I + \Delta_{IO}$. These are the only two possibilities for emission for OIO if the coherence $|I\rangle\langle O|$ does not transfer to another element. The Feynman diagrams for OOI are shown in Figure 7-3(b). A population in O leads to excited-state absorption into the combination band state $|IO\rangle$ with no stimulated emission because the third pulse is not resonant with O. The other two diagrams for OOI are due to ground state bleach with emission at E_I.

Figure 7-4 shows the Feynman diagrams for OIO (a) and OOI (b) that involve amplitude transfer from the prepared state to another state. For example, the coherence $|I\rangle\langle O|$ can change into population in I (far left diagram). If this occurs, excited-state absorption is the only transition resonant with the third pulse. Therefore, this diagram features emission near E_O. The element χ_{IIIO} can be extracted from the time dependence of the signal appearing at the energy $E_O + \Delta_{IO}$. If there is excitonic coherence transfer, e.g. χ_{OIIO} (diagram second from left), then excited-state absorption is again the only possible pathway. In this case the emission energy is highly blue-shifted to $2E_O - E_I + \Delta_O$, and the time-dependent probability of coherence

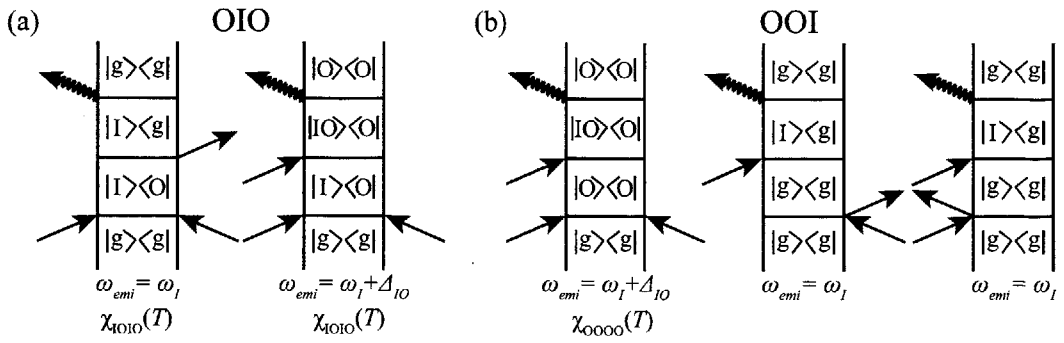

Figure 7-3: Example diagrams for two QPT pulse sequences. Underneath each diagram is the emission frequency and contributing element of χ. (a) Diagrams for the OIO experiment which evolves in a coherence $|I\rangle\langle O|$ during T. (b) OOI diagrams, evolving with a population during T.

transfer can be extracted by monitoring this emission.

The Feynman diagrams for OOI in Figure 7-4 show how population transfer and population-to-coherence transfer manifest in the experiment. For population transfer, the population in O should proceed downhill in energy to I. The third field can then stimulate emission or induce absorption to the double-excited state $|II\rangle$. The emission energies in this case overlap with the emission energies without population relaxation. These inherently overlapping nonlinear signals are specifically what QPT is designed to separate. If the population in O transfers to a coherence then the emission energy is well separated from the emission energy without transfer. Therefore, monitoring the emission energies reports directly on the separate probabilities of these transfers occurring.

Analysis of the full set of Feynman diagrams (see Appendix A) for all eight experiments reveals the non-trivial fact that any coherence-to-population transfers or coherence transfers, i.e. nonsecular transfers in Redfield theory, lead to emission at separate energies compared to other transfer events such as intra-exciton population relaxation, radiative or non-radiative recombination, and coherence dephasing. Therefore, any nonsecular transfers are immediately evident upon inspection of the raw experimental data and are straightforward to characterize. The full set of diagrams are shown in Appendix A.

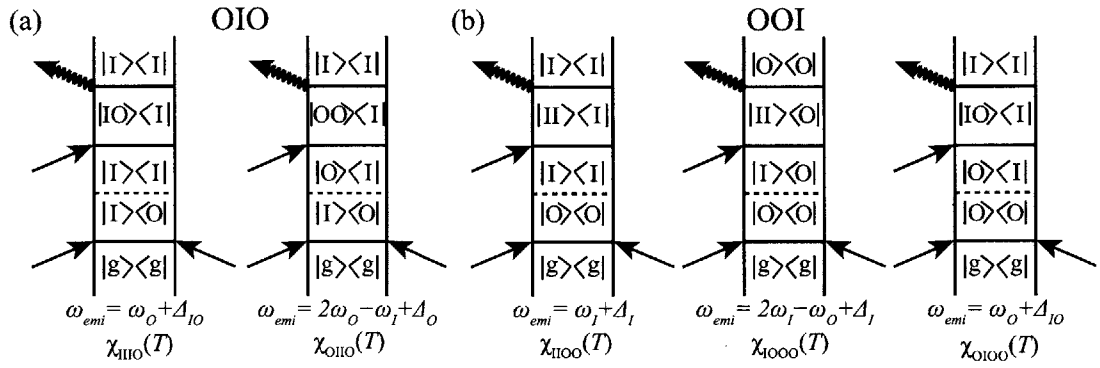

Figure 7-4: Example diagrams for transfer processes for OIO and OOI. (a) Diagrams for OIO which involve nonsecular transfers. (b) OOI diagrams showing population transfer and nonsecular transfers.

The two experiments *OIO* and *OOI* demonstrate the salient features of the QPT methodology as applied to nonlinear spectroscopy: some types of transfer processes are cleanly separated, i.e. nonsecular transfers, while others remain congested and overlapping. However, using QPT it is possible to write each nonlinear signal as a linear combination of process matrix elements, and it is therefore possible to invert this relationship, giving the process matrix elements in terms of experimental signals (see Refs. [269] and [264]). In the next subsection I give an explicit example of this procedure for the V-level system.

Secular QPT Example

In this subsection I use the V-level system to show that the nonlinear experiments can be described as linear combinations of χ elements, and that these relationships can be inverted to give the elements of χ. Each Feynman diagram gives a contribution proportional to the dipoles of the transitions, a single χ element, and an exponential factor at the emission energy with a phenomenological dephasing rate γ. I use the secular approximation (only dephasing and population transfer are allowed), no uphill energy transfer (reasonable for the nanotubular system under study in the next section), and slow ground state bleach (g.s.b.) recovery compared to the interband relaxation and coherence dephasing (reasonable for the nanotubular system [261]).

Under the secular approximation, each of the coherence experiments (exciting either IO or OI) is directly proportional to a single element of χ. For example, the nonlinear signals for IOI and OIO are

$$\begin{aligned} IOI(T,t) &= |\mu_I|^2|\mu_O|^2\, \chi_{OIOI}(T)\, e^{-i\omega_O t-\gamma_O t}, \\ OIO(T,t) &= |\mu_I|^2|\mu_O|^2\, \chi_{IOIO}(T)\, e^{-i\omega_I t-\gamma_I t}. \end{aligned} \tag{7.6}$$

Our experiments are detected in the frequency domain via spectral interferometry. We therefore integrate over emission frequency which, according to Fourier transform relationships, is the same as setting the emission time $t = 0$. This leads directly to $IOI(T, t = 0) \propto \chi_{OIOI}(T)$ and $OIO(T, t = 0) \propto \chi_{IOIO}(T)$. III and IIO only depend on a single process matrix element, χ_{IIII}, because there are only ground state bleach terms while the only allowed transfer process is uphill energy transfer, which is energetically unfavorable at room temperature. Therefore, $III(T, t = 0) \propto \chi_{IIII}(T)$ and $IIO(T, t = 0) \propto \chi_{IIII}(T)$.

The experiments OOO and OOI are more complicated because of population relaxation from O to I. The nonlinear signal for OOO is

$$\begin{aligned} OOO(T,t) =& |\mu_O|^2|\mu_{OO,O}|^2\, \chi_{OOOO}(T)\, e^{-i(\omega_O+\Delta_O)t-\gamma_{OO,O}t} \\ &-|\mu_O|^4\, \chi_{OOOO}(T)\, e^{-i\omega_O t-\gamma_O t} \\ &+|\mu_O|^2|\mu_{IO,I}|^2\, \chi_{IIOO}(T)\, e^{-i(\omega_O+\Delta_{IO})t-\gamma_{IO,I}t} \\ &-2|\mu_O|^4\, e^{-\Gamma T}\, e^{-i\omega_O t-\gamma_O t}. \end{aligned} \tag{7.7}$$

The nonlinear signal for OOI is

$$
\begin{aligned}
OOI(T,t) =& |\mu_O|^2 |\mu_{IO,O}|^2 \, \chi_{OOOO}(T) \, e^{-i(\omega_I+\Delta_{IO})t-\gamma_{IO,O}t} \\
&+|\mu_O|^2 |\mu_{II,I}|^2 \, \chi_{IIOO}(T) \, e^{-i(\omega_I+\Delta_I)t-\gamma_{II,I}t} \\
&-|\mu_O|^2 |\mu_I|^2 \, \chi_{IIOO}(T) \, e^{-i\omega_I t-\gamma_I t} \\
&-2|\mu_O|^2 |\mu_I|^2 \, e^{-\Gamma T} \, e^{-i\omega_I t-\gamma_I t}. \qquad (7.8)
\end{aligned}
$$

From Equations 7.7 and 7.8 it is clear that each nonlinear signal is a linear combination of χ elements. The last two terms for each nonlinear signal are the ground state bleach (g.s.b.), which depend on how long it takes for the electronic excitation to relax back to the ground state. This timescale, $1/\Gamma$, is typically tens of picoseconds, well beyond the timescale of excitonic population redistribution and coherent dynamics. Therefore, in the following we treat the g.s.b. as a constant and subtract it. The following manipulations invert this relationship to re-write the χ elements as linear combinations of nonlinear signals. First, I define the following coefficients to allow easier manipulation of the equations,

$$
\begin{aligned}
c_1 &= |\mu_O|^2 |\mu_{OO,O}|^2 e^{-i(\omega_O+\Delta_O)t-\gamma_{OO,O}t} \\
c_2 &= |\mu_O|^4 e^{-i\omega_O t-\gamma_O t} \\
c_3 &= |\mu_O|^2 |\mu_{IO,I}|^2 e^{-i(\omega_O+\Delta_{IO})t-\gamma_{IO,I}t} \\
c_4 &= |\mu_O|^2 |\mu_{IO,O}|^2 e^{-i(\omega_I+\Delta_{IO})t-\gamma_{IO,O}t} \\
c_5 &= |\mu_O|^2 |\mu_{II,I}|^2 e^{-i(\omega_I+\Delta_I)t-\gamma_{II,I}t} \\
c_6 &= |\mu_O|^2 |\mu_I|^2 e^{-i\omega_I t-\gamma_I t}. \qquad (7.9)
\end{aligned}
$$

Using this shorthand and making t implicit, as it will eventually be set to zero, Equations 7.7 and 7.8 become

$$OOO(T) = (c_1 - c_2)\chi_{OOOO}(T) + c_3\chi_{IIOO}(T) + g.s.b.$$
$$OOI(T) = c_4\chi_{OOOO}(T) + (c_5 - c_6)\chi_{IIOO}(T) + g.s.b. \tag{7.10}$$

Using the condition $\chi_{ijqp}(0) = \delta_{iq}\delta_{jp}$, which ensures that at $T = 0$ no transfers have occurred, and the approximation that the g.s.b. recovery is a constant background gives

$$OOO(T = 0) = (c_1 - c_2) + g.s.b.$$
$$OOI(T = 0) = c_4 + g.s.b. \tag{7.11}$$

Subtracting the $T = 0$ contribution from each time-dependent experiment gives a signal free of g.s.b.

$$OOO_c(T) = OOO(T) - OOO(T = 0) = (c_1 - c_2)\chi_{OOOO}(T) - (c_1 - c_2) + c_3\chi_{IIOO}(T)$$
$$OOI_c(T) = OOI(T) - OOI(T = 0) = c_4\chi_{OOOO}(T) - c_4 + (c_5 - c_6)\chi_{IIOO}(T). \tag{7.12}$$

Re-arranging the first line of Equation 7.12 leads to

$$\chi_{OOOO}(T) = \frac{OOO_c(T) - c_3\chi_{IIOO}(T)}{c_1 - c_2} + 1. \tag{7.13}$$

Substituting Equation 7.13 into the second line in Equation 7.12 and solving for $\chi_{IIOO}(T)$ gives an equation for $\chi_{IIOO}(T)$ in terms of the nonlinear signals,

$$\chi_{IIOO}(T) = \frac{\frac{c_4}{c_1 - c_2}OOO_c(T) - OOI_c(T)}{\frac{c_3 c_4}{c_1 - c_2} - c_5 + c_6}. \tag{7.14}$$

Substituting $\chi_{IIOO}(T)$ into Equation 7.13 gives an equation for $\chi_{OOOO}(T)$ in terms of nonlinear signals,

$$\chi_{OOOO}(T) = \frac{OOO_c(T) - \frac{\frac{c_3 c_4}{c_1 - c_2} OOO_c(T) - c_3 OOI_c(T)}{\frac{c_3 c_4}{c_1 - c_2} - c_5 + c_6}}{c_1 - c_2} + 1. \tag{7.15}$$

This derivation demonstrates that in order to calculate χ all that is required are the experimental data and the coefficients, $c_1 - c_6$. The coefficients are combinations of transition dipole moments and complex exponentials, which is why QPT does in fact require a model for the system that includes transition energies, transition dipoles, and at the very least phenomenological dephasing rates. However, the complete dynamics of the excitonic system can be calculated, for any given initial conditions, without a model for the excitonic dynamics. This can help with the design of, for example, coherent control experiments that may require specific initial conditions.

An additional approximation that significantly reduces the complexity of retrieving χ, both theoretically and experimentally, is to neglect the combination state $|IO\rangle$. This would be possible if the excitonic coupling were extremely weak, leading to a weak transition dipole moment to $|IO\rangle$ from either $|I\rangle$ or $|O\rangle$, or if the pulses used for excitation were not resonant with the transitions between the single-exciton states and $|IO\rangle$. The neglect of this state makes the coefficients c_3 and c_4 zero, leading to simplification for $\chi_{OOOO}(T)$ and $\chi_{IIOO}(T)$ in terms of nonlinear signals,

$$\chi_{OOOO}(T) = \frac{OOO_c(T)}{c_1 - c_2} \tag{7.16}$$

and

$$\chi_{IIOO}(T) = \frac{OOI_c(T)}{c_5 - c_6}. \tag{7.17}$$

Under this additional approximation, each element of χ is directly proportional to a single experiment (and vice versa), vastly simplifying the analysis. Integrating each experiment over emission frequency (setting $t = 0$) gives a single element of χ directly.

7.2 QPT of Nanotubular Excitons

In this section I describe the experimental realization of QPT as applied to *J*-aggregate light harvesting nanotubes. I first describe the system and experimental setup. Next, I show experimental results for the same OIO and OOI pulse sequences described in the previous section. Finally, I present QPT results for the process matrix, demonstrating the extraction of dephasing and energy transfer dynamics between the inner and outer walls of the nanotubes.

7.2.1 Experimental Parameters

Previous work assigned the two lowest energy exciton bands to the inner and outer walls of the complex [217]. Here, we approximate each band as a single exciton so we can apply the previously developed methodology and use H polarized laser pulses centered on each band to study the interactions, dynamics, and coherence between them (see Figure 7-5(a)). The requirement of eight pulse sequences, with changing center frequencies for each pulse, makes two-dimensional pulse shaping a highly attractive option for the experiment. Computer control of independent amplitude and phase profiles allows relatively facile implementation of the QPT methodology, and even allows switching between standard 2D ES measurements and QPT transient grating measurements.

In the experiment the excitation power was ~ 0.5 nJ/pulse. In the data analysis, each of the eight experiments is weighted by the strength of the excitation fields, calculated from the pulse energies and spectra. In addition, the optical density (OD) of the solution slightly decreased over the course of the experiments (Figure 7-5(b)). Linear absorption spectra taken before each experiment provided a scaling factor proportional to the OD.

7.2.2 Transient Grating Results

The two example experiments OIO and OOI are shown in Figure 7-6, left and right columns, respectively. The OIO signal emits near 600 nm, as expected based on the

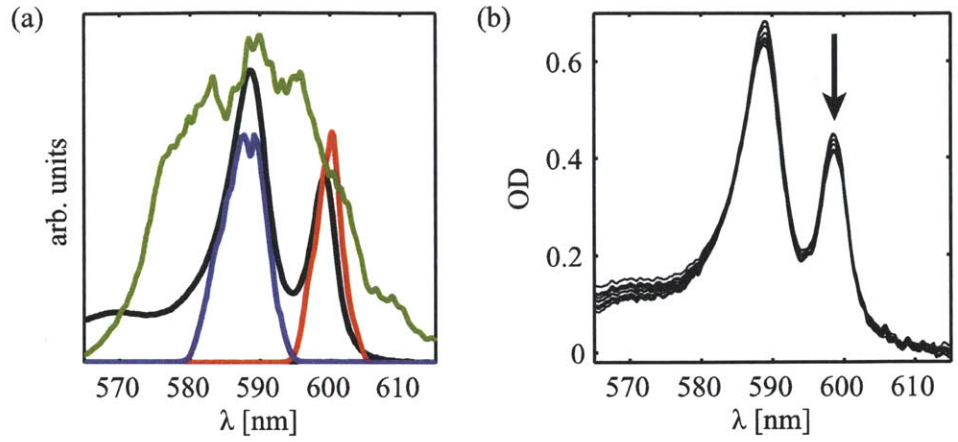

Figure 7-5: (a)H polarized linear absorption (black) for J-aggregate nanotubes shows two excitons of interest: O at 590 nm and I at 600 nm. Pulse shaping enables frequency-selective excitation pulses O (blue) and I (red) by applying amplitude filters to a broadband pulse (dashed green). (b) Optical density decreased during acquisition of experiments over $\sim$ 2 hours.

Feynman diagrams in Figure 7-3(a). The signal exhibits oscillations at the difference frequency between states $|O\rangle$ and $|I\rangle$ in the real (and imaginary) components, demonstrating coherence between the walls. The lack of additional peaks means that no coherence transfer or coherence-to-population transfer processes occurred, i.e. nonsecular processes did not occur. In fact, there were no nonsecular processes detected (which would be evidenced by the appearance of emission at different frequencies as previously discussed) in any of the eight experiments. Therefore the OIO scan is directly proportional to χ_{OIOI} because the amplitude in ρ_{OI} does not transfer to any other density matrix element but rather decays (dephases) (see Feynman diagrams in Figure 7-3(a)).

The OOI experiment shown in Figure 7-6 (right) also emits where predicted by the Feynman diagrams (Figure 7-3(b)) without nonsecular element transfer. The first two pulses create a population. If there is no population transfer, the third pulse I induces absorption and creates the coherence $|IO\rangle\langle O|$, which emits near E_I at 600 nm. If there is population transfer, the third pulse can stimulate emission to the ground state or induce absorption to $|II\rangle\langle I|$, both of which feature emission at or near E_I. The real (and imaginary) parts of OOI can be used to separate some of these different

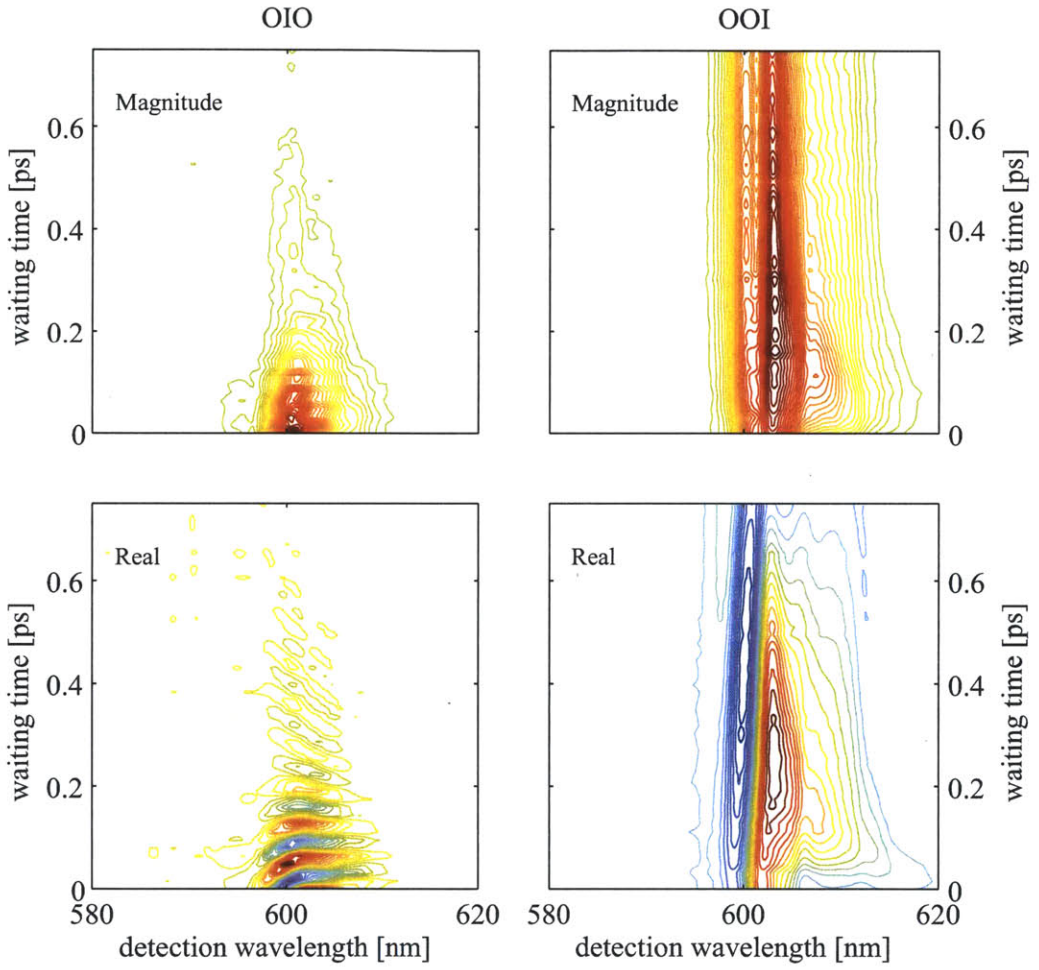

Figure 7-6: Raw data showing coherence scan OIO (left) and population scan OOI (right).

pathways because the optically active transitions between J-aggregate two-exciton states and one-exciton states are slightly blue-shifted with respect to the ground-state−one-exciton transition energy [259, 261]. However, this does not separate the pathways lacking population transfer from those including it. The additional QPT experiments are required to fully separate these components.

The lack of emission at the frequencies expected after nonsecular transfer processes (see Figure 7-4) is direct evidence that the process matrix elements χ_{IIIO}, χ_{IIOI}, χ_{IOII}, χ_{OIII}, χ_{IOOI}, χ_{OOOI}, χ_{OOIO}, χ_{OIOO}, χ_{IOOO}, and χ_{OIIO} are close to zero. Only six elements of χ remain: population decay χ_{IIII} and χ_{OOOO}; population transfer χ_{IIOO} and χ_{OOII}; and coherence decay (dephasing) χ_{IOIO} and χ_{OIOI}. This greatly simplifies the analysis and complete extraction of the process matrix, described in the following section (for complete details see Refs. [269] and [264]).

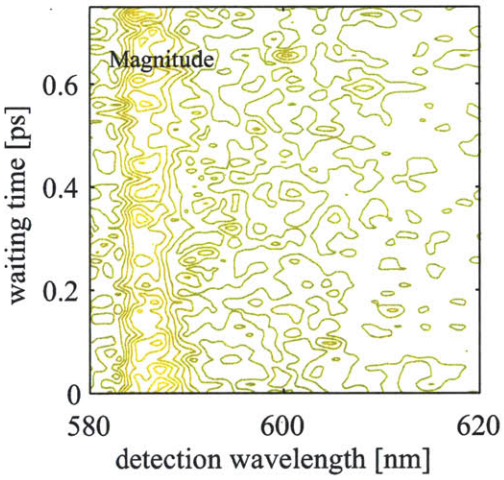

Figure 7-7: Absolute value transient grating data for IIO pulse sequence.

The excited-state lifetime of C8S3 DW-LHNs is tens of picoseconds [261] implying that the ground state recovery time is well beyond the timescale of this measurement. Therefore, we treat the ground state bleaching terms as constant factors that can be subtracted from the measurements, isolating the excited state dynamics and further simplifying the QPT analysis. In addition, the scan IIO had nearly zero amplitude (see Figure 7-7) and was close the signal to noise limit of the experiment. This justifies the approximation that the combination state $|IO\rangle$ does not contribute significantly

to the nonlinear signals.

7.2.3 QPT Results

The transient grating data was analyzed in a series of steps. The first was correction of the data for experimental differences between scans, such as the excitation field intensities and decreasing optical density. In addition, each scan was corrected for the roll-off caused by femtosecond pulse shaping. The next step assumes the state $|IO\rangle$ does not significantly contribute to the experiments because the excitonic coupling is very weak [217]. This approximation is critical and assumes that the transition dipoles follow the inequality $\mu_{IO,I}, \mu_{IO,O} \ll \mu_{II,I}, \mu_{OO,O}, \mu_{I,g}, \mu_{O,g}$; or that the excitation pulses are not resonant with the $|IO\rangle \leftrightarrow |O\rangle$ or $|IO\rangle \leftrightarrow |I\rangle$ transition energies. Next, the nonlinear emission spectra were divided by the $T = 0$ spectra to correct for the relatively unchanging ground state bleach terms, leaving only the time-dependence of the populations (see Section 7.1.2). The coherence pulse sequences OIO, OII, IOI, and IOO did not have have this correction applied as there is no ground state bleach term. Exploiting the normalization condition that $\chi_{ijqp}(0) = \delta_{iq}\delta_{jp}$ allows integration over the emission frequency for each experiment, directly yielding elements of χ according to Equations 7.16 and 7.17. The next step utilizes semi-definite programming [271] to ensure $\chi(T)$ transforms physical density matrices (e.g. Hermitian, trace preserving, positive population probabilities) to other physical density matrices.

Results of the QPT analysis are shown in Figure 7-8. In the left panel are shown population decay χ_{OOOO} and population transfer from $|O\rangle$ to $|I\rangle$, χ_{IIOO}. The population in $|O\rangle$ decreases very quickly due to ultrafast downhill energy transfer to the inner wall. The overall signal decay is accelerated further by intensity roll-off caused by pulse shaping. χ_{OOOO} decays in 370 fs, indicating that all of the population has left state $|O\rangle$ by this time. The onset of $|O\rangle$ to $|I\rangle$ transfer is almost immediate with a transfer time of 160 fs, evidenced by the quick rise in χ_{IIOO}. However, unlike the Redfield model in Section 7.1.1, the transfer probability does not increase to 1. This could be due to unobserved optically dark states that accept population from the outer wall

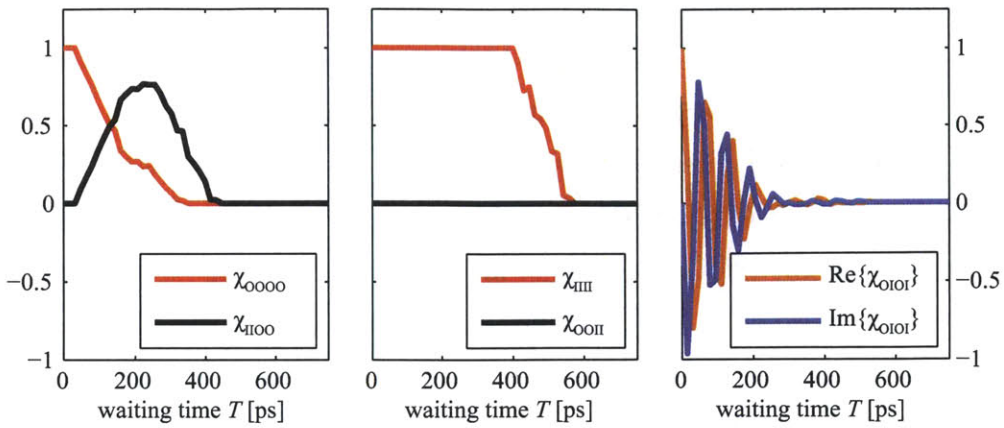

Figure 7-8: Process matrix elements. (Left) Population decay in outer wall $|O\rangle$ and population transfer from the outer to inner wall. (Middle) Inner wall population decay and inner wall to outer wall population transfer. (Right) Dephasing of coherence $|O\rangle\langle I|$.

and are not included in the simple two-level model, leading to an equilibrium population distributed amongst both bright and dark states. At the pulse energies used in this experiment, an additional complicating factor is exciton-exciton annihilation, which provides a very fast, highly efficient non-radiative relaxation pathway for the excitons. This would cause the exciton population to not be conserved and recovery of the ground state as well. Another way to see this is that the total transfer probability out of the outer wall is less than one, i.e. $\chi_{OOOO}(T) + \chi_{IIOO}(T) \leq 1$. This inequality means that the population initialized in the outer wall is not conserved within the observable system, implying the existence of dark states or possibly a very fast, very efficient nonradiative decay mechanism. However, complete radiationless relaxation to the ground state is unlikely as the excitons exhibit fluorescence from each wall and the lifetimes measured in previous studies are on the order of tens of picoseconds [261].

The middle plot in Figure 7-8 shows the decay of population in $|I\rangle$ with a decay time of 720 fs. The initial resistance of the inner wall excitons to decay is probably due to the influx of population from the outer wall. The transfer probability from the inner wall to the outer wall is negligble because the energy transfer would be uphill by 13 THz, or 430 cm^{-1}, whereas thermal energy at room temperature is closer to

200 cm^{-1} which is insufficient to drive the uphill transition.

The coherent dynamics are shown in the right plot in Figure 7-8. The oscillations in the real and imaginary components occur at the difference frequency 13 THz, indicating creation of a coherence between inner and outer wall excitons (see Figure 7-5). Only the data for $|O\rangle\langle I|$ are shown as those for $|I\rangle\langle O|$ are quantitatively very similar, as expected. The excitonic coherence implies that even though the coupling is weak between the two walls [217], wavefunction delocalization is still possible even over several nanometers of separation. This result is in agreement with the 2D electronic spectroscopy results presented in Chapter 6 in which the 2D spectrum exhibited a small yet measurable crosspeak (see Figure 6-8, left panels), indicating weak excitonic coupling. Exciton-exciton annihilation would not affect the coherent dynamics because no exciton populations are created, only a coherent state is excited.

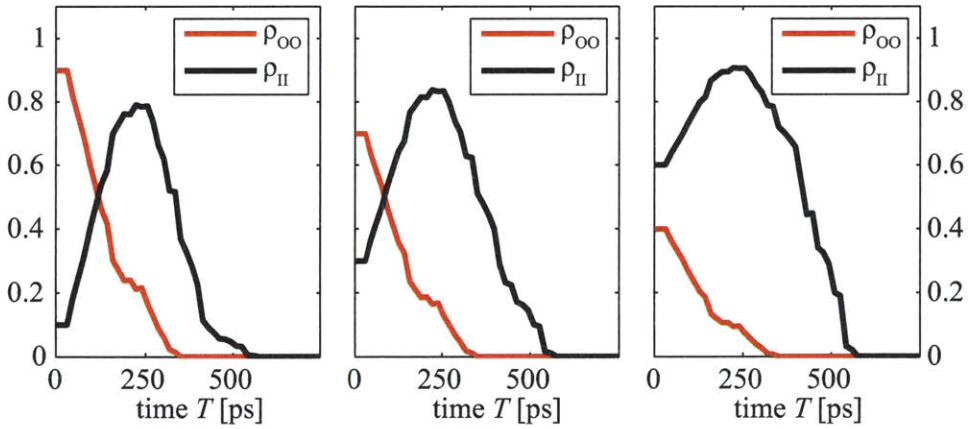

Figure 7-9: Nanotube populations calculated using the process matrix for three different initial populations.

It is straightforward to calculate exciton dynamics using the process matrix using Equation 7.2. As an example, the population elements are

$$\begin{aligned}\rho_{II}(t) &= \chi_{IIII}(t)\rho_{II}(0) + \chi_{IIOO}(t)\rho_{OO}(0) \\ \rho_{OO}(t) &= \chi_{OOOO}(t)\rho_{OO}(0) + \chi_{OOII}(t)\rho_{II}(0).\end{aligned} \tag{7.18}$$

Figure 7-9 shows dynamics for three initial populations, with the condition that the initial populations satisfy the condition $\rho_{II}(0) + \rho_{OO}(0) = 1$. ρ_{OO} simply decays because uphill population transfer from ρ_{II} is energetically unfavorable, evidenced by the fact that χ_{OOII} is negligible. ρ_{II} continually gains population from ρ_{OO} until ρ_{OO} is depleted; ρ_{II} then decays fully.

The complete decay of the excited states implies either the existence of lower energy dark states not probed in the experiments or the full recovery of the ground state during the experimental time window. Dark states are improbable to be responsible because the lowest energy excitons in J-aggregates are the optically bright $k = 0$ excitons, which also emit fluorescence with negligible Stokes shift. Ground state recovery is possible, however it is difficult to measure directly in our experimental setup because of the complicating factor of the pulse shaper intensity roll-off: the signal amplitude decay is mostly due to the roll-off and due to actual dynamics of the excitonic system. Additional effects such as exciton-exciton annihilation may cause some ground state recovery during the experiment as well. Fast recovery of ground state population during the experiment would lead to invalidation of one of the approximations used to calculate the process matrix elements. In addition, it is possible that the $|IO\rangle$ combination state does have a non-negligible contribution to the experiments, thus affecting the current analysis.

The spectrally-resolved pump-probe experiments in Ref. [261] show population transfer and excited state decay timescales, however the experiments are unable to separate the contributions from the $|IO\rangle$ state and the $|II\rangle$ or $|OO\rangle$ states, and could not unambiguously isolate the population dynamics of I and O. The 2D spectra shown in the previous chapter can separate some of the overlapping signal contributions into diagonal and crosspeaks, however any dynamics of the system, e.g. downhill energy transfer, would have created overlapping signals at the crosspeak frequency coordinates. Narrowband pump-probe measurements would separate population from coherent dynamics, but could not uniquely determine relaxation from one state to another versus relaxation to the ground state. The results presented in this section demonstrate clear separation of population from coherent dynamics, and further still

the separation of population dynamics for different excitons.

7.3 Conclusions

In this chapter I have shown results demonstrating the potential for quantum process tomography to provide a methodical approach to nonlinear spectroscopy for separating coherence dynamics from population relaxation dynamics. Using two-color transient grating spectroscopy, QPT was performed for supramolecular light harvesting nanotubes and determined that population transfer from the outer wall to the inner wall of the nanotube occurs on a 160 fs timescale. In addition, pulse sequences designed for sensitivity to coherence revealed coherent dynamics between the two nanotube walls with a coherence decay time of 250 fs. The QPT methodology developed and applied in this chapter has great potential not only in the design and analysis of nonlinear spectroscopy measurements but also in their optimization for extracting maximal information content about the systems under study.

Chapter 8

Many-Body Effects in Quantum Wells

This chapter details efforts to understand correlations and interactions between many excitons, a critical concept for device physics such as optical gain via multi-exciton generation [272, 273, 274]. We study semiconductor excitons in Gallium Arsenide (GaAs) quantum wells as a model system for investigating these many-body interactions. Studies have shown that many-body interactions among semiconductor excitons can produce distinct features in two-dimensional optical spectra. However, the dynamics of the many-body interactions have never been measured in 2D spectroscopy studies. Here we measure 2D spectra of GaAs quantum wells at many different 'waiting' times and study the time dependence of the spectral features. Characteristic signatures of exciton polarization correlations manifest in the diagonal peaks decay at the exciton dephasing rate, consistent with theoretical predictions. Other many-body interactions manifest in off-diagonal features decay much more slowly. These persistent off-diagonal features must be due to many-body interactions involving exciton populations, and their persistence cannot be predicted by theoretical descriptions restricted to the coherent limit.

8.1 Semiconductor Quantum Wells

In many scientific disciplines, groups of objects can interact to produce startling emergent phenomena, that is, "more is different" [275]. In condensed-matter physics, many-body interactions often occur due to the attractions and repulsions among charged particles. These collective effects are difficult to calculate from first principles, making experimental measurements essential to guide our understanding and to motivate and direct theoretical efforts [276, 88, 85, 84, 277]. Semiconductors and their nanostructures offer extraordinary prospects for incisive experimental study of many-body effects because of the following properties: the optically generated excitons are delocalized and weakly bound, enabling Coulomb interactions among their charged electron and hole constituents; the nanostructure dimensionality and dimensions can be designed to confine the excitons so that they must interact; the exciton density can be easily controlled by incident light intensities; and exciton coherences as well as populations can be manipulated by coherent light sources, providing additional avenues for control over many-body interactions and exquisite sensitivity to them in the signals of coherent nonlinear spectroscopy measurements.

GaAs quantum wells were studied extensively [276, 88, 85, 84, 277, 278, 279, 280, 281, 282, 283, 284, 285, 286, 86, 287, 288, 289, 290, 291, 292, 293, 294, 295, 296, 297, 298, 299, 300, 301, 302, 90] throughout the 1980s and 1990s, primarily through four-wave mixing measurements, resulting in new insights about phenomena such as quantum beats, exciton dephasing times and mechanisms, disorder, and many-body interactions. The application of another four-wave mixing technique known as two-dimensional (2D) Fourier-transform optical spectroscopy heralded a new era of investigation [303, 304, 305, 306, 307, 308, 106, 108, 107, 110, 117, 136]. To date, these nonlinear spectroscopy experiments have been understood using theoretical treatments at varying levels of sophistication. Our results show that one of the approximations commonly used in the first-principles treatments is not generally valid.

In 2D spectroscopy, we introduce a variable time delay between the two pump pulses, τ_1, which allows us to record and correlate the spectrum of states excited and

emitted, $S(\omega_{excite}, \tau_2, \omega_{emit})$. The excitation and emission dimensions are produced by Fourier transformation of coherent optical polarizations during the respective time periods. The delay time τ_2 (the 'waiting' time) is varied parametrically, and, similar to pump-probe measurements, the changes in spectral features as a function of τ_2 are typically related to incoherent excited-state dynamics. An important feature of 2D spectroscopy is that the phase and amplitude of the emitted signal are sensitive to the phase and amplitude of the coherent excitations produced in the sample by the excitation fields. This *coherence* requirement means that spectral features are sensitive to exciton phases. As shown through phenomenological models [90, 304, 136], many-body interactions can influence the amplitudes and phases of exciton coherences in a variety of ways, and these changes modify the frequency-dependent emission signals that originate with excitation at any of the exciton frequencies. Therefore all of the peaks in a 2D spectrum are sensitive to the presence and the detailed nature of many-body interactions. As previously mentioned in Section 2.4.1, the many-body interactions cannot be described using Feynman diagrams. This is because many-body interactions do not produce new eigenstates but rather dynamical effects such as polarization-polarization scattering and coupling between excitons and unbound electron-hole states. Previous studies focused on unexpected features produced by many-body interactions in the 2D spectra at $\tau_2 = 0$. Here we vary τ_2 and measure changes to the unexpected features.

2D spectral features and the many-body interactions that produce them have been treated through explicit first-principles theoretical calculations of the Coulomb correlations among electrons and holes, performed in the site basis [85, 309, 310] or momentum basis [311, 277, 312]. The results yielded mean-field polarization-polarization scattering terms that influence the phases of diagonal peaks and, going beyond the Hartree-Fock approximation, four-particle (meaning two-exciton) correlations that give rise to otherwise unexpected off-diagonal spectral features [305]. Although the theoretical predictions are in reasonable agreement with experiments [304, 305, 108, 307, 107, 110, 136], neither theoretical nor prior experimental studies have addressed the time-dependent changes to any of the spectral features during τ_2.

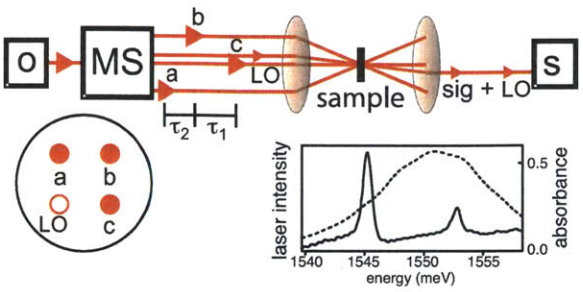

Figure 8-1: Experimental setup for 2D spectroscopy of GaAs quantum wells. A Ti:sapphire oscillator (o) creates femtosecond pulses in a single beam. The multi-dimensional spectrometer (MS) transforms this beam into four beams arranged on the corners of a square (inset) and sets the pulse delay times. The beams are then focused to the sample. In the nonrephasing scan (shown), field $\mathbf{E}_c$ interacts first, followed first by field $\mathbf{E}_b$ after time delay τ_1 and then field $\mathbf{E}_a$ after time delay τ_2. The fields generate a phase-matched signal in the $\mathbf{k}_{sig} = \mathbf{k}_a - \mathbf{k}_b + \mathbf{k}_c$ direction. In a rephasing or photon echo scan (not shown), the time ordering of fields $\mathbf{E}_c$ and $\mathbf{E}_b$ are exchanged. In both cases, the resulting signal is overlapped with a weak reference field called a local oscillator (LO) and is heterodyne detected by the spectrometer (s). The 2D spectra displayed in this work are the sum of the rephasing and nonrephasing signals. The absorbance of the sample (solid line) and the spectrum of the laser pulse (dashed line) are also shown.

Moreover, all of the microscopic theoretical approaches assumed the *coherent limit* in which the exciton polarization dephasing rate is linked to the exciton population decay rate. In other words, in this limit, effects due to exciton populations cannot be separated from effects due to exciton coherences. 2D spectroscopy measurements conducted at waiting times long enough that exciton polarizations have decayed should allow separation of the two kinds of interactions.

8.2 Experimental Details

We performed 2D spectroscopy measurements using two experimental apparatuses—the COLBERT spectrometer [136] and the JILA-MONSTR [123]—that produced the four coherent fields in the beam geometry illustrated in Figure 8-1. Briefly, each instrument used a Ti:sapphire oscillator to produce pulses of about 100 fs duration with pulse energies of a few nJ. The spectral bandwidth covered both the heavy-hole

exciton (H) and light-hole exciton (L) resonances at 1545 meV and 1553 meV, respectively. The H exciton linewidth indicates a dephasing time of about 10 ps. Experiments at MIT (JILA) were conducted with an excitation density of about 3×10^{10} excitons/cm^2/well (4.5×10^9 excitons/cm^2/well) in a sample that consisted of ten (four) layers of 10 nm thick GaAs, separated by 10 nm thick $Al_{0.3}Ga_{0.7}As$ barriers. The exciton population lifetimes are on the order of a hundred picoseconds at these densities. In all measurements, the sample was cooled to 10 K and the laser fields were co-circularly polarized. The spectra were phased using the established procedure for each apparatus [136, 313]. We present data taken with the JILA-MONSTR; the qualitative features were reproduced in the data taken with the COLBERT spectrometer on a different sample. The difference between the data sets was the decay time of the features. In the MIT measurements, the decay time of the symmetry factor (see below) was faster than 3 ps; this was due to the delay-dependent amplitude modulation of the COLBERT spectrometer [136]. The similarity of the observations confirms that they are not due to experimental issues, such as phase drift in the spectrometer, and that they are not unique to one sample.

8.3 2D Spectra and Analysis

8.3.1 2D Correlation Spectra

Rephasing (nonrephasing) spectra were collected when field E_b (E_c) interacted first, followed after time period τ_1 by field E_c (E_b), for each value of τ_2. The rephasing and nonrephasing spectra were measured independently and then summed to create the 2D spectra displayed in Figure 8-2. Rephasing or nonrephasing spectra alone are not sufficient to extract true lineshapes because the individual spectra have wings due to 'phase twist'; taking the sum of the two spectra removes the mixing between the absorptive and dispersive characters [314, 122]. An absorptive lineshape is typically Lorentizan in character, while a dispersive lineshape is typically similar to the derivative of a Lorentzian. In a 2D spectrum of a simple system, peaks will have absorptive

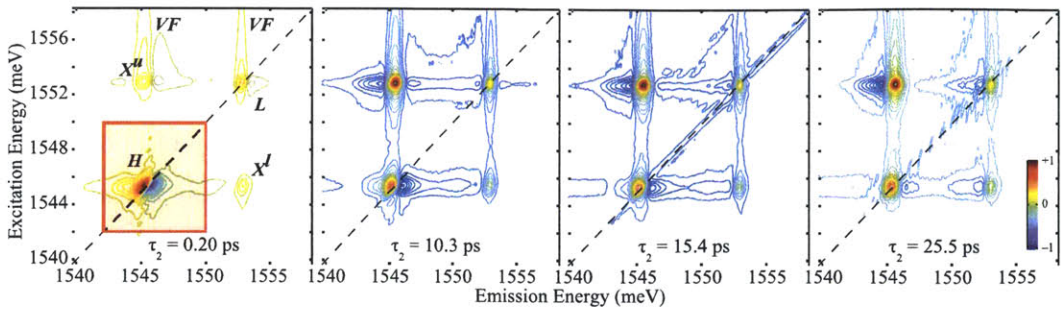

Figure 8-2: The real part of the 2D spectra under co-circular polarization measured at the indicated waiting times (τ_2). The dashed line indicates the diagonal, $E_{excite} = E_{emit}$, and the red box highlights the H diagonal peak. Cross peaks between the H and L features are not expected in this polarization configuration in the absence of many-body interactions because the two excitons do not share a common conduction band. Coulomb correlations couple the two states, leading to cross peaks labeled X^u and X^l. Vertical features (VF) are due to exciton–free-carrier scattering.

lineshapes, cross peaks will only appear between coupled transitions, excited-state-absorption pathways will lead to negative-amplitude peaks, and additional features are not observed. The shape of a peak indicates the relative contributions of homogeneous and inhomogeneous dephasing mechanisms. We extracted a homogeneous dephasing time of 5.0±0.1 ps from the amplitude of the rephasing signal of the H diagonal peak using a fit procedure described previously [234].

We display only the real parts of the complex-valued spectra in Figure 8-2 for selected values of τ_2. With co-circularly polarized pulses, cross peaks are not expected because the H and L excitons have electrons which reside in different conduction bands [84] and therefore the transitions that generate the two excitons are not coupled through a common spectroscopic ground state. However, as shown in Figure 8-2, cross peaks labeled X^u and X^l do appear. Strong vertical features, also previously observed [303], are due to scattering between excitons and free carriers. The cross peaks and vertical features have been reproduced in microscopic theories by including four-particle interaction terms into the equations of motion [305]. Below we show that since these spectral features persist at long τ_2 times, this assignment was incomplete.

The strongest peak in Figure 8-2—the H diagonal peak highlighted in the red square—has a dispersive lineshape at small values of τ_2, in agreement with previous

rephasing measurements [304, 307, 107]. As τ_2 increases, the positive part becomes stronger than the negative part and shifts toward the diagonal line. At very long τ_2 times, the peak has an absorptive lineshape and is centered on the diagonal line. During this transition from dispersive to absorptive, the nodal line tilts from being parallel to the diagonal line to being completely vertical, indicating a loss of correlation [314] among multiple excitons.

8.3.2 Lineshape Analysis

To understand better the lineshape change, we project the H diagonal peak onto the emission axis and plot the projections in Figure 8-3(a) for selected values of τ_2. The lineshape changes systematically from an antisymmetric shape to a symmetric shape. Since the peak symmetry reflects how dispersive the lineshape is, we define a *symmetry factor* (η) given by

$$\eta(\tau_2) = \frac{\int p(\tau_2, \omega_{emit}) \mathrm{d}\omega_{emit}}{\int |p(\tau_2, \omega_{emit})| \mathrm{d}\omega_{emit}}, \tag{8.1}$$

where $p(\tau_2, \omega_{emit})$ is the projection of the signal inside the red square as a function of emission energy at a particular waiting time. Using this equation, a purely dispersive lineshape corresponds to $\eta = 0$ and a purely absorptive lineshape with a positive (negative) amplitude corresponds to $\eta = 1$ ($\eta = -1$). The symmetry factors retrieved from the 2D spectra at eleven τ_2 values are shown in Figure 8-3(b). Initially, $\eta = 0$; it then increases and saturates at $\eta = 1$ by about 20 ps. As mentioned above, rephasing or nonrephasing spectra alone are not sufficient to extract the data presented in Figure 8-3.

The normalized amplitudes of the H and X^l peaks during τ_2 are shown in Figure 8-3(b). The data were created by integrating over a square that covered each peak in the amplitude (not real part) of the 2D spectra to account for any changes to the shape of the peaks. Due to the projection-slice theorem, it should be possible, at least in principle, to measure the data presented in Figure 8-3 using a narrowband, frequency-resolved pump-probe measurement, but it would be difficult to draw conclusions

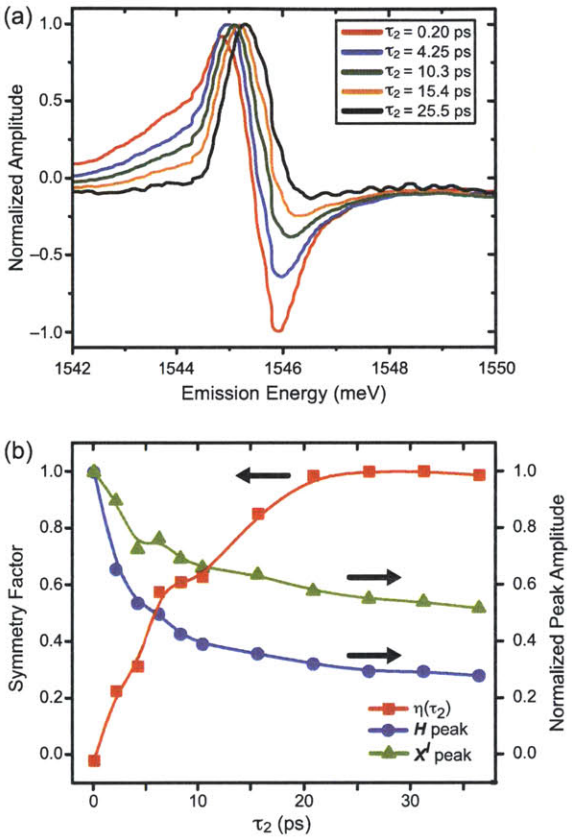

Figure 8-3: Peak and lineshape dynamics extracted from the 2D spectra. (a) Projections of the H diagonal peak onto the emission axis for the indicated τ_2 values. (b) Extracted symmetry factor and the normalized amplitudes of the H diagonal peak and the X^l cross peak at several τ_2 values. Lines are guides to the eye. The decay of the symmetry factor reflects the decay of the polarization-polarization scattering terms. Both H and X^l retain nonzero amplitudes at 35 ps.

about many-body interactions since the cross peaks and vertical features would not be visible.

8.4 Excitonic Many-Body Interactions

The measurements reveal a key new insight about many-body interactions in GaAs quantum wells. The dispersive lineshape of the H diagonal peak is characteristic of many-body interactions, whereas the absorptive lineshape is more characteristic of the case without many-body interactions, for example, including only simple Pauli-blocking terms [305] which account for the reduction of allowed transitions for fermions due to the Pauli exclusion principle. The fact that the cross peaks and vertical features do not disappear at long waiting times means that the many-body terms have not vanished. In principle, incoherent population relaxation from high-energy states (unbound electron-hole pairs and L excitons) to H could be responsible for the continued presence of X^u and the vertical features. However, as shown in Figure 8-3(b), the X^l peak—which cannot be due to incoherent relaxation—has only decayed to about half its original amplitude at 35 ps. Thus we conclude that the evolution of the spectra must reflect evolution of the many-body state. Specifically, we suggest that the dispersive lineshape is due to polarization-polarization scattering, and the polarizations decay on picosecond time-scales, while many-body interactions involving exciton populations persist, leading to the unanticipated spectral features at long τ_2 times.

In the momentum basis, the polarization scattering effect can be understood in the following manner. First, the light generates an excitonic polarization with $\mathbf{k}_{\mathrm{cm}} = 0$ (arrow 1 in Figure 8-4). Due to carrier-carrier scattering and carrier-phonon scattering, this initial excitonic polarizaton is scattered to excitonic polarizations and populations at larger $\mathbf{k}_{\mathrm{cm}}$ (arrows 2A, the arrow represents scattering into both polarization and populations states). The excitonic polarization can also scatter into unbound electron-hole states, which form a continuum (arrows 2B), but at the low excitation densities used here this process is less important. These processes happen

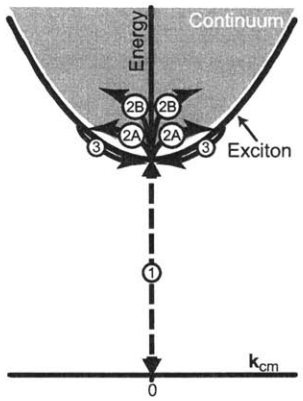

Figure 8-4: Schematic showing the energy versus center-of-mass momentum ($\mathbf{k}_{cm}$) for electron-hole pairs bound into excitons (bold line) and unbound pairs that form a continuum (grey area). Excitation by light (1) produces an excitonic polarization at $\mathbf{k}_{cm} = 0$ that rapidly scatters to excitonic polarization and populations at $|\mathbf{k}_{cm}| > 0$ (2A) and to unbound pairs (2B) in the continuum. The resulting many-body configuration then evolves (3) as the polarizations decay and the populations relax back toward $\mathbf{k}_{cm} = 0$.

very rapidly, but the subsequent evolution of the many-body configuration as carriers scatter towards a thermal distribution (arrows 3) is slower. A true thermal equilibrium is not achieved within the time window of our experiments because of radiative recombination of excitons within the light-cone (close to $\mathbf{k}_{cm} = 0$) [see Figure 38 in Ref. [311]]. Careful comparison between experiment and theory have shown that the excitonic lineshape in linear absorption spectra can be used to estimate the many-body configuration [312]. Thus, at short delay the presence of excitonic polarizations results in a very different lineshape than for longer delays where the excitonic polarizations have decayed and only populations remain. Our results use the evolution of the 2D lineshape to monitor the dynamics of the many-body states as they evolve from a mixture of polarizations and populations to being purely populations.

In our experiments, the behavior shown in Figure 8-3 depends strongly on the sample position. The rise time, which is about 20 ps in the presented case, varies over a wide range under identical conditions except for a change in sample position. In some cases, the rise time is so long that $\eta = 0$ for almost the entire window of nearly 40 ps. This spatial inhomogeneity could be caused by stress due to differences

in thermal expansion since the sample is mounted on a sapphire disk. A comparison of the absorption spectra at different spots on the sample showed frequency shifts (but no linewidth changes) for the the H and L resonances. A larger frequency shift corresponded to a longer rise time in η. However, an explanation of the detailed mechanism requires further investigation.

8.5 Conclusions

We have measured 2D optical spectra of excitons in GaAs quantum wells using co-circularly polarized beams for waiting times out to nearly 40 ps. Our results provide unique insight into the evolution of the optically induced many-body state and show that the effect of polarization-polarization scattering decays on picosecond time scales, but several spectral features that were previously attributed to coherent four-particle interactions persist. We attribute those features to many-body interactions involving exciton populations. This observation means that new theoretical models are needed that do not assume the coherent limit [305, 85, 309], where the signal decay is governed solely by exciton dephasing. Additionally, since calculations of many-body states [312] have not included dynamics, our observations should motivate the development of a dynamical many-body theory for optically excited semiconductors.

Chapter 9

Conclusions and Outlook

In this thesis I have presented the results from nonlinear spectroscopy experiments designed to look for coherence and coherent dynamics in several nanostructured systems. These experiments have revealed the nature and extent of excitonic coherence in both organic and inorganic semiconductor materials, J-aggregates and GaAs quantum wells, respectively.

Several additional projects have begun that utilize the multi-dimensional spectrometer to continue these investigations in a broader range of systems. We are beginning to explore singlet fission in tetracene and pentacene, materials used in organic solar cells and organic light emitting diodes that offer the possibility for creating multiple electrons from each photo-generated exciton. In addition, studies of quantum dot excitons are underway to fully understand the effects of quantum confinement on the excitonic band structure. Finally, collaborations have begun with the goal of understanding interactions between inorganic and organic excitons, particularly in complexes made from J-aggregates coupled to quantum dots and other inorganic semiconductors. Multi-dimensional spectroscopy will prove particularly adept at revealing not only the kinetics of energy transfer between these materials but also the nature of the transfer, e.g. if it is coherent or incoherent.

In addition to the aforementioned projects, a large effort has been underway to study exciton transport using transient grating spectroscopy. The experiments have focused on J-aggregates, which are thought to have diffusion lengths on the order of

100 nm. However, experiments using the transient grating setup described in Chapter 3 have proven difficult due to highly efficient exciton-exciton annihilation, even at the lowest excitation intensities. This is encouraging because it means excitons are able to move some distance to find each other to annihilate. However, it makes the analysis and interpretation of the transient grating data nearly impossible for all practical purposes as the effects of excited state lifetime, annihilation, and transport are all superposed in the collected time traces.

Several improvements could be made to the experiments to increase the signal to noise, thereby allowing for lower excitation densities and removing the complicating effects of annihilation. The simplest is to use the U3 J-aggregates described in Chapter 5, which would allow the use of the KMLabs oscillator. The 8000-fold increase in laser repetition rate would allow much lower excitation densities while maintaining high signal to noise. Another technique would be to image the fluorescence from the grating directly, allowing reduction of the excitation intensity through highly sensitive fluorescence detection techniques. In addition, fluorescence in these systems, which have a reasonably high quantum yield, may yield greater emission intensities than nonlinear signals. Imaging the fluorescent grating onto, e.g. a streak camera, would spatially and temporally resolve exciton diffusion as it occurred between the peaks and nulls of the grating. In the Fourier plane, the fluorescence would emerge as two spatially separated beams of light. As the grating pattern in the near field is filled via exciton transport, the spatially separated beams would become more diffuse and eventually merge into a single diffuse spot. Therefore, the contrast ratio between the initially localized beams and a dark spot, e.g. directly between the two beams, would provide a highly accurate measure of the transport dynamics.

The results in this thesis and the new projects promise to elucidate the nature of excitons in both organic and inorganic semiconductors currently used in optoelectronic applications. The insights will prove beneficial to improving current optoelectronic devices as well as design of devices using novel architectures or materials. I am confident that the science and techniques presented in this thesis will play a significant role in the elucidation of the physics that may affect the emergence of these

new technologies.

Appendix A

Additional QPT Feynman Diagrams

This appendix enumerates the Feynman diagrams for the six experiments not shown explicitly in Chapter 7. Figure A-1 shows the diagrams for experiments exciting a population, OOO, III, and IIO; while Figure A-2 shows the diagrams for experiments exciting a coherence, IOI, IOO, and OII. Included in both figures are diagrams without density matrix element transfers and those with the most likely transfers, i.e. downhill in energy.

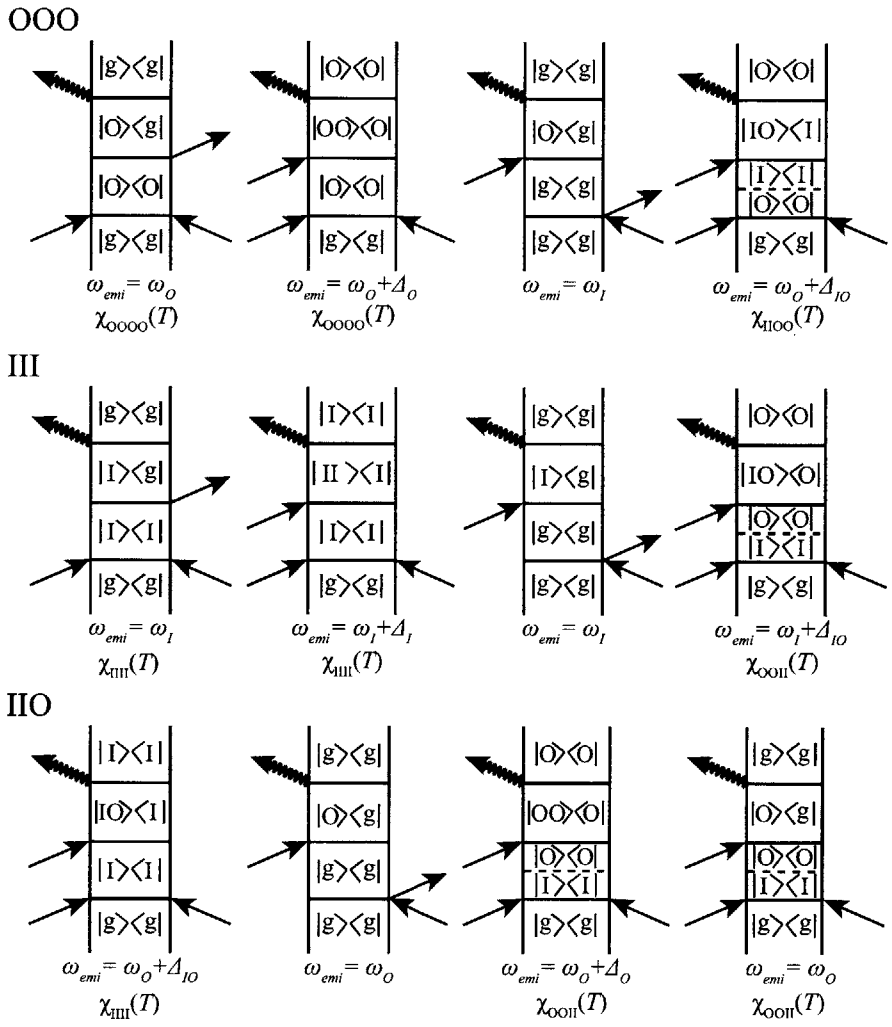

Figure A-1: Feynman diagrams for pulse sequences pumping a population.

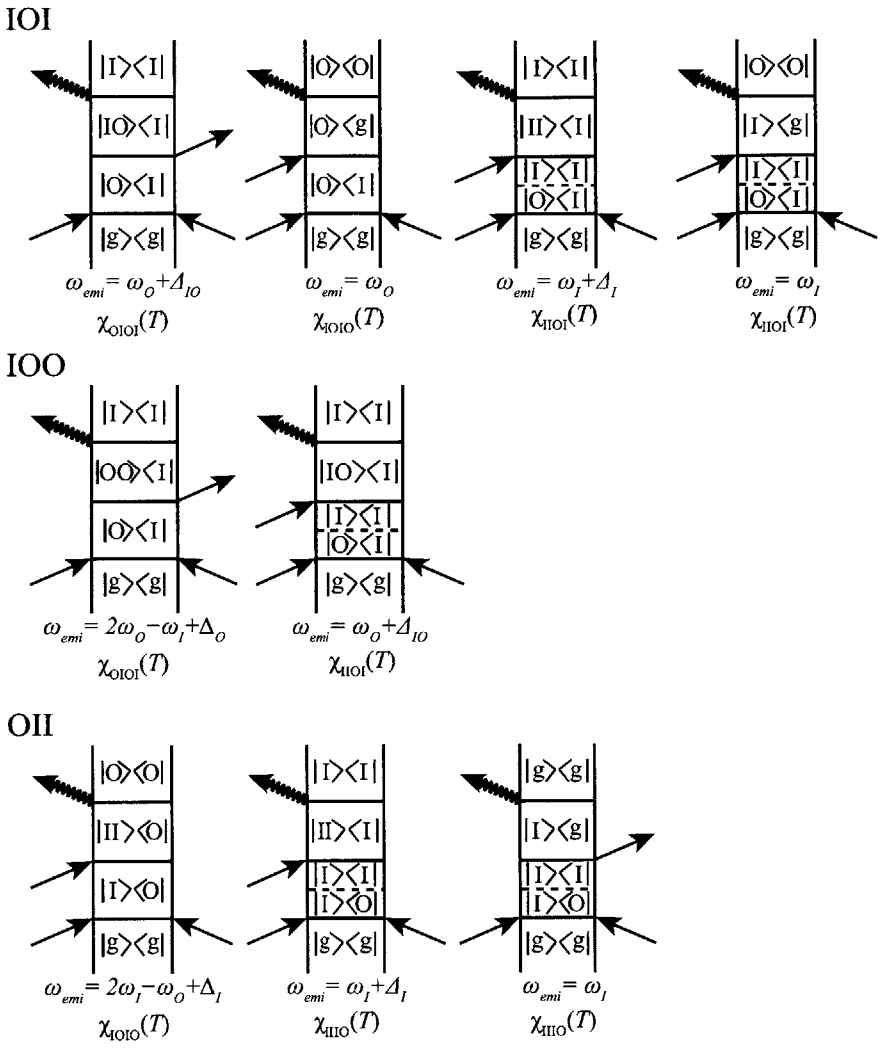

Figure A-2: Feynman diagrams for pulse sequences pumping a coherence.

Bibliography

[1] K.E. Drexler. *Nanosystems: Molecular Machinery, Manufacturing, and Computation.* John Wiley and Sons, New York, 1992.

[2] J. Bisquert. Nano-Enabled Photovoltaics. Progress in Materials and Methodologies. *The Journal of Physical Chemistry Letters*, 4:1051–1052, 2013.

[3] J. Frenkel. On the transformation of light into heat in solids. I. *Physical Review*, 37(1):17–44, 1931.

[4] J. Frenkel. On the transformation of light into heat in solids. II. *Physical Review*, 37(1):1276, 1931.

[5] G.D. Scholes and G. Rumbles. Excitons in nanoscale systems. *Nature Materials*, 5(9):683–696, 2006.

[6] S.W. Koch, M. Kira, G. Khitrova, and H.M. Gibbs. Semiconductor excitons in new light. *Nature Materials*, 5(7):523–531, 2006.

[7] V. Percec, M. Glodde, T.K. Bera, Y. Miura, I. Shiyanovskaya, K.D. Singer, V.S.K. Balagurusamy, P.A. Heiney, I. Schnell, A. Rapp, H.-W. Spiess, S.D. Hudson, and H. Duan. Self-organization of supramolecular helical dendrimers into complex electronic materials. *Nature*, 419(6905):384–387, September 2002.

[8] W. Zhang, W. Jin, T. Fukushima, A. Saeki, S. Seki, and T. Aida. Supramolecular Linear Heterojunction Composed of Graphite-Like Semiconducting Nanotubular Segments. *Science*, 334(6054):340–343, October 2011.

[9] T. Aida, E.W. Meijer, and S.I. Stupp. Functional Supramolecular Polymers. *Science*, 335(6070):813–817, February 2012.

[10] Y.C. Cheng and R.J. Silbey. Coherence in the B800 ring of purple bacteria LH2. *Physical Review Letters*, 96(2):028103, 2006.

[11] C. Külheim, J. Agren, and S. Jansson. Rapid regulation of light harvesting and plant fitness in the field. *Science*, 297(5578):91–93, July 2002.

[12] G.D. Scholes, G.R. Fleming, A. Olaya-Castro, and R. van Grondelle. Lessons from nature about solar light harvesting. *Nature Chemistry*, 3(10):763–774, September 2011.

[13] R.E. Blankenship, D.M. Tiede, J. Barber, G.W. Brudvig, G.R. Fleming, M. Ghirardi, M.R. Gunner, W. Junge, D.M. Kramer, A. Melis, T.A. Moore, C.C. Moser, D.G. Nocera, A.J. Nozik, D.R. Ort, W.W. Parson, R.C. Prince, and R.T. Sayre. Comparing photosynthetic and photovoltaic efficiencies and recognizing the potential for improvement. *Science*, 332(6031):805–809, May 2011.

[14] Y. Tachibana, L. Vayssieres, and J.R. Durrant. Artificial photosynthesis for solar water-splitting. *Nature Photonics*, 6:511–518, 2012.

[15] P.W. Bohn. Aspects of structure and energy transport in artificial molecular assemblies. *Annual Review of Physical Chemistry*, 44(1):37–60, 1993.

[16] A.K. Ringsmuth, G.J. Milburn, and T.M. Stace. Multiscale photosynthetic and biomimetic excitation energy transfer. *Nature Physics*, 8(7):562–567, June 2012.

[17] R.E. Fenna and B.W. Matthews. Chlorphyll arrangement in a bacteriochlorphyll protein from Chlorbium limicola. *Nature*, 258:573–577, 1975.

[18] S. Ganapathy, G.T. Oostergetel, P.K. Wawrzyniak, M. Reus, A. Gomez Maqueo Chew, F. Buda, E.J. Boekema, D.A. Bryant, A.R. Holzwarth, and H.J.M. de Groot. Alternating syn-anti bacteriochlorophylls form concentric helical nanotubes in chlorosomes. *Proceedings of the National Academy of Sciences of the United States of America*, 106(21):8525–8530, May 2009.

[19] V. May and O. Kuhn. *Charge and Energy Transfer Dynamics in Molecular Systems*. Wiley-VCH Verlag GmbH & Co. KGaA, Weinheim, Germany, 2 edition, 2004.

[20] T. Brixner, J. Stenger, H.M. Vaswani, M. Cho, R.E. Blankenship, and G.R. Fleming. Two-dimensional spectroscopy of electronic couplings in photosynthesis. *Nature*, 434(7033):625–8, March 2005.

[21] G.S. Engel, T.R. Calhoun, E.L. Read, T.K. Ahn, T. Mančal, Y.C. Cheng, R.E. Blankenship, and G.R. Fleming. Evidence for wavelike energy transfer through quantum coherence in photosynthetic systems. *Nature*, 446(7137):782–786, 2007.

[22] J. Dostál, T. Mančal, R. Augulis, F. Vácha, J. Pšenčík, and D. Zigmantas. Two-Dimensional Electronic Spectroscopy Reveals Ultrafast Energy Diffusion in Chlorosomes. *Journal of the American Chemical Society*, 134(28):11611–11617, July 2012.

[23] G.R. Fleming and G.D. Scholes. Quantum mechanics for plants. *Nature*, 431:256–257, 2004.

[24] M. Cho, N.F. Scherer, S. Mukamel, and G.R. Fleming. Photon echoes and related four-wave-mixing using phase-locked pulses. *The Journal of Chemical Physics*, 96(8):5618, 1992.

[25] S. Mukamel. *Principles of Nonlinear Optical Spectroscopy.* Oxford University Press, Inc., New York, 1995.

[26] T. Joo, Y. Jia, J. Yu, M.J. Lang, and G.R. Fleming. Third-order nonlinear time domain probes of solvation dynamics. *The Journal of Chemical Physics*, 104(16):6089, 1996.

[27] T. Renger and V. May. Multiple exciton effects in molecular aggregates: Application to a photosynthetic antenna complex. *Physical Review Letters*, 78(17):3406–3409, 1997.

[28] T. Renger, V. May, and O. Kuhn. Ultrafast excitation energy transfer dynamics in photosynthetic pigment-protein complexes. *Physics Reports*, 343(3):137–254, 2001.

[29] D.M. Jonas. Two-dimensional femtosecond spectroscopy. *Annual Review of Physical Chemistry*, 54:425–463, 2003.

[30] Y.C. Cheng and G.R. Fleming. Dynamics of light harvesting in photosynthesis. *Annual Review of Physical Chemistry*, 60:241–262, 2009.

[31] N.S. Ginsberg, Y.C. Cheng, and G.R. Fleming. Two-dimensional electronic spectroscopy of molecular aggregates. *Accounts of Chemical Research*, 42(9):1352–63, September 2009.

[32] G.R. Fleming and M. Cho. Chromophore-Solvent Dynamics. *Annual Review of Physical Chemistry*, 47(1):109–134, October 1996.

[33] M. Yang and G.R. Fleming. Third-order nonlinear optical response and energy transfer in static disordered systems. *The Journal of Chemical Physics*, 113(7):2823, 2000.

[34] D. Zigmantas, E.L. Read, T. Mancal, T. Brixner, A.T. Gardiner, R.J. Cogdell, and G.R. Fleming. Two-dimensional electronic spectroscopy of the B800-B820 light-harvesting complex. *Proceedings of the National Academy of Sciences*, 103(34):12672–12677, August 2006.

[35] D. Abramavicius, D.V. Voronine, and S. Mukamel. Double-quantum resonances and exciton-scattering in coherent 2D spectroscopy of photosynthetic complexes. *Proceedings of the National Academy of Sciences*, 105(25):8525, 2008.

[36] G.D. Scholes. Designing light-harvesting antenna systems based on superradiant molecular aggregates. *Chemical Physics*, 275(1-3):373–386, 2002.

[37] A. Perdomo, L. Vogt, A. Najmaie, and A. Aspuru-Guzik. Engineering directed excitonic energy transfer. *Applied Physics Letters*, 96(9):093114, 2010.

[38] E.E. Jelley. Spectral Absorption and Fluorescence of Dyes in the Molecular State. *Nature*, 138:1009, 1936.

[39] G. Scheibe. ber die Vernderlichkeit der Absorptionsspektren in Lsungen und die Nebenvalenzen als ihre Ursache. *Angew. Chem.*, 50:212–219, 1937.

[40] F. Würthner, T.E. Kaiser, and C.R. Saha-Möller. J-Aggregates: From Serendipitous Discovery to Supramolecular Engineering of Functional Dye Materials. *Angewandte Chemie International Edition*, 50:3376–3410, March 2011.

[41] T. Kobayashi, editor. *J-aggregates*. World Scientific, Singapore, 1996.

[42] T. Kobayashi, editor. *J-aggregates*. World Scientific, Singapore, 2012.

[43] H. von Berlepsch, C. Bottcher, A. Ouart, C. Burger, S. Dahne, and S. Kirstein. Supramolecular structures of J-aggregates of carbocyanine dyes in solution. *The Journal of Physical Chemistry B*, 104(22):5255–5262, 2000.

[44] H. von Berlepsch, C. Böttcher, A. Ouart, M. Regenbrecht, S. Akari, U. Keiderling, H. Schnablegger, S. Dähne, and S. Kirstein. Surfactant-Induced Changes of Morphology of J-Aggregates: Superhelix-to-Tubule Transformation. *Langmuir*, 16(14):5908–5916, July 2000.

[45] H. von Berlepsch, S. Kirstein, and C. Böttcher. Effect of Alcohols on J-Aggregation of a Carbocyanine Dye. *Langmuir*, 18(20):7699–7705, October 2002.

[46] H. von Berlepsch, S. Kirstein, and C. Böttcher. Controlling the Helicity of Tubular J-Aggregates by Chiral Alcohols. *The Journal of Physical Chemistry B*, 107(36):9646–9654, September 2003.

[47] S. Kirstein and S. Daehne. J-aggregates of amphiphilic cyanine dyes: Self-organization of artificial light harvesting complexes. *International Journal of Photoenergy*, 2006:1–21, 2006.

[48] D.M. Eisele, J. Knoester, S. Kirstein, J.P Rabe, and D.A. Vanden Bout. Uniform exciton fluorescence from individual molecular nanotubes immobilized on solid substrates. *Nature Nanotechnology*, 4(10):658–63, October 2009.

[49] K. Misawa, H. Ono, K. Minoshima, and T. Kobayashi. New fabrication method for highly oriented J aggregates dispersed in polymer films. *Applied Physics Letters*, 63:577, 1993.

[50] Y.V. Malyukin, O.G. Tovmachenko, G.S. Katrich, and K. Kemnitz. Optical spectroscopy of disorder in molecular chains (J-aggregates). *Low Temperature Physics*, 24(12):879, December 1998.

[51] M.S. Bradley, J.R. Tischler, and V. Bulović. Layer-by-Layer J-Aggregate Thin Films with a Peak Absorption Constant of 10^6cm1. *Advanced Materials*, 17(15):1881–1886, August 2005.

[52] J.R. Tischler, M.S. Bradley, and V. Bulovic. Critically coupled resonators in vertical geometry using a planar mirror and a 5 nm thick absorbing film. *Optics Letters*, 31(13):2045–7, July 2006.

[53] Q. Zhang, T. Atay, J.R. Tischler, M.S. Bradley, V. Bulovic, and A.V. Nurmikko. Highly efficient resonant coupling of optical excitations in hybrid organic/inorganic semiconductor nanostructures. *Nature Nanotechnology*, 2(9):555–559, 2007.

[54] J.E. Halpert, J.R. Tischler, G.P. Nair, B.J. Walker, W. Liu, V. Bulovic, and M.G. Bawendi. Electrostatic Formation of Quantum Dot/J-aggregate FRET Pairs in Solution. *The Journal of Physical Chemistry C*, 113(23):9986–9992, June 2009.

[55] B.J. Walker, V. Bulović, and M.G. Bawendi. Quantum Dot/J-Aggregate Blended Films for Light Harvesting and Energy Transfer. *Nano Letters*, 10:3995–3999, September 2010.

[56] B.J. Walker, A. Dorn, V. Bulovic, and M.G. Bawendi. Color-Selective Photocurrent Enhancement in Coupled J-Aggregate/Nanowires Formed in Solution. *Nano Letters*, 11(7):2655–2659, May 2011.

[57] V. Sundström, T. Gillbro, R.A. Gadonas, and A. Piskarskas. Annihilation of singlet excitons in J aggregates of pseudoisocyanine (PIC) studied by pico- and subpicosecond spectroscopy. *The Journal of Chemical Physics*, 89(5):2754, 1988.

[58] H. Fidder and D.A. Wiersma. Collective optical response of molecular aggregates. *Physica Status Solidi (B)*, 188:285–285, 1995.

[59] M. van Burgel, D.A. Wiersma, and K. Duppen. The dynamics of one-dimensional excitons in liquids. *The Journal of Chemical Physics*, 102(1):20, 1995.

[60] J. Moll, S. Daehne, J.R. Durrant, and D.A. Wiersma. Optical dynamics of excitons in J aggregates of a carbocyanine dye. *The Journal of Chemical Physics*, 102(16):6362, 1995.

[61] I.G. Scheblykin, O.P. Varnavsky, M.M. Bataiev, O. Sliusarenko, M. Van Der Auweraer, and G. Vitukhnovsky. Non-coherent exciton migration in J-aggregates of the dye THIATS: excitonexciton annihilation and fluorescence depolarization. *Chemical Physics Letters*, 298:341–350, 1998.

[62] K. Nishimura, E. Tokunaga, and T. Kobayashi. Sub-5-fs two-dimensional spectroscopy of pseudoisocyanine J-aggregates. *Chemical Physics Letters*, 395(1-3):114–119, September 2004.

[63] A.G. Dijkstra, T. la Cour Jansen, and J. Knoester. Localization and coherent dynamics of excitons in the two-dimensional optical spectrum of molecular J-aggregates. *The Journal of Chemical Physics*, 128(16):164511, April 2008.

[64] A. Nemeth, F. Milota, J. Sperling, D. Abramavicius, S. Mukamel, and H.F. Kauffmann. Tracing exciton dynamics in molecular nanotubes with 2D electronic spectroscopy. *Chemical Physics Letters*, 469(1-3):130–134, February 2009.

[65] F. Milota, J. Sperling, A. Nemeth, D. Abramavicius, S. Mukamel, and H.F. Kauffmann. Excitonic couplings and interband energy transfer in a double-wall molecular aggregate imaged by coherent two-dimensional electronic spectroscopy. *The Journal of Chemical Physics*, 131(5):054510, August 2009.

[66] F. Milota, J. Sperling, A. Nemeth, and H.F. Kauffmann. Two-dimensional electronic photon echoes of a double band J-aggregate: Quantum oscillatory motion versus exciton relaxation. *Chemical Physics*, 357:45–53, 2009.

[67] J.M. Womick, S.A. Miller, and A.M. Moran. Probing the dynamics of intraband electronic coherences in cylindrical molecular aggregates. *The Journal of Physical Chemistry A*, 113(24):6587–98, June 2009.

[68] J.M. Womick, S.A. Miller, and A.M. Moran. Correlated exciton fluctuations in cylindrical molecular aggregates. *The Journal of Physical Chemistry B*, 113(19):6630–6639, May 2009.

[69] J. Sperling, A. Nemeth, J. Hauer, D. Abramavicius, S. Mukamel, H.F. Kauffmann, and F. Milota. Excitons and disorder in molecular nanotubes: a 2D electronic spectroscopy study and first comparison to a microscopic model. *The Journal of Physical Chemistry A*, 114(32):8179–89, August 2010.

[70] D. Abramavicius, A. Nemeth, F. Milota, J. Sperling, S. Mukamel, and H.F. Kauffmann. Weak Exciton Scattering in Molecular Nanotubes Revealed by Double-Quantum Two-Dimensional Electronic Spectroscopy. *Physical Review Letters*, 108(6):067401, February 2012.

[71] D.G. Lidzey, D.D.C. Bradley, T. Virgili, A. Armitage, M.S. Skolnick, and S. Walker. Room temperature polariton emission from strongly coupled organic semiconductor microcavities. *Physical Review Letters*, 82(16):3316–3619, 1999.

[72] J. Song, Y. He, J.R. Tischler, A.V. Nurmikko, and V. Bulovic. Exciton-polariton dynamics in a transparent organic semiconductor microcavity. *Physical Review B*, 69(23):235330, 2004.

[73] J.R. Tischler, M.S. Bradley, and V. Bulović. Strong Coupling in a Microcavity LED. *Physical Review Letters*, 95(3):036401, July 2005.

[74] J.R. Tischler, M.S. Bradley, Q. Zhang, T. Atay, A.V. Nurmikko, and V. Bulovic. Solid state cavity QED: Strong coupling in organic thin films. *Organic Electronics*, 8(2-3):94–113, April 2007.

[75] G.C. La Rocca. Organic photonics: Polariton lasing. *Nature Photonics*, 4(6):343–345, June 2010.

[76] J. Shah. *Ultrafast Spectroscopy of Semiconductors and Semiconductor Nanostructures*. Springer-Verlag, Berlin, 1996.

[77] T. Meier, P. Thomas, and S. Koch. *Coherent Semiconductor Optics*. Springer-Verlag, Berlin, 2007.

[78] S.T. Cundiff. Coherent spectroscopy of semiconductors. *Optics Express*, 16(7):4639–4664, 2008.

[79] A. Tokmakoff. Time-Dependent Quantum Mechanics and Spectroscopy. http://www.mit.edu/ tokmakof/TDQMS/, 2011.

[80] R.W. Boyd. *Nonlinear Optics*. Academic Press, Burlington, MA, 3 edition, 2008.

[81] D.J. Griffiths. *Introduction to Electromagnetism*. Addison Wesley, Upper Saddle River, 3 edition, 1999.

[82] S. Mukamel. Femtosecond Optical Spectroscopy: A Direct Look at Elementary Chemical Events. *Annual Review of Physical Chemistry*, 41(1):647–681, October 1990.

[83] K. Blum. *Density Matrix Theory and Applications*. Plenum Press, New York, NY, 1981.

[84] Steven T Cundiff. Coherent spectroscopy of semiconductors. *Opt. Express*, 16(7):4639–4664, Mar 2008.

[85] T. Meier, P. Thomas, and S. Koch. *Coherent Semiconductor Optics*. Springer-Verlag, Berlin, 2007.

[86] K Leo, M Wegener, J Shah, DS Chemla, EO Gobel, TC Damen, S Schmitt-Rink, and W Schäfer. Effects of coherent polarization interactions on time-resolved degenerate four-wave mixing. *Phys. Rev. Lett.*, 65(11):1340–1343, Sep 1990.

[87] M Wegener, DS Chemla, S Schmitt-Rink, and W Schafer. Line shape of time-resolved four-wave mixing. *Phys. Rev. A*, 42(9):5675–5683, 1990.

[88] D S Chemla and J Shah. Many-body and correlation effects in semiconductors. *Nature*, 411(6837):549–57, 2001.

[89] H Wang, K Ferrio, DG Steel, YZ Hu, R Binder, and SW Koch. Transient nonlinear optical response from excitation induced dephasing in gaas. *Phys. Rev. Lett.*, 71(8):1261–1264, Aug 1993.

[90] J. M. Shacklette and S. T. Cundiff. Role of excitation-induced shift in the coherent optical response of semiconductors. *Phys. Rev. B*, 66:045309, 2002.

[91] M.D. Fayer. Dynamics of Molecules in Condensed Phases: Picosecond Holographic Grating Experiments. *Annual Review of Physical Chemistry*, 33(1):63–87, October 1982.

[92] W.T. Pollard and R.A. Mathies. Analysis of femtosecond dynamic absorption spectra of nonstationary states. *Annual Review of Physical Chemistry*, 43:497–523, 1992.

[93] D.A. Wiersma and K. Duppen. Picosecond Holographic-Grating Spectroscopy. *Science*, 237(4819):1147–1154, 1987.

[94] W.P. de Boeij, M.S. Pshenichnikov, and D.A. Wiersma. Ultrafast solvation dynamics explored by femtosecond photon echo spectroscopies. *Annual Review of Physical Chemistry*, 49(1):99–123, 1998.

[95] J.R. Salcedo, A.E. Siegman, D.D. Dlott, and M.D. Fayer. Dynamics of energy transport in molecular crystals: the picosecond transient-grating method. *Physical Review Letters*, 41(2):131–134, 1978.

[96] V.M. Kenkre. *Exciton dynamics in molecular crystals and aggregates.* Springer Verlag, New York, NY, 1982.

[97] K.A. Nelson, R. Casalegno, R.J.D. Miller, and M.D. Fayer. Laser-induced excited state and ultrasonic wave gratings: Amplitude and phase grating contributions to diffraction. *The Journal of Chemical Physics*, 77(3):1144, 1982.

[98] J.T. Fourkas and M.D. Fayer. The Transient Grating: A Holographic Window to Dynamic Processes. *Accounts of Chemical Research*, 25(5):227–233, May 1992.

[99] E.C. Fulmer, P. Mukherjee, A.T. Krummel, and M.T. Zanni. A pulse sequence for directly measuring the anharmonicities of coupled vibrations: Two-quantum two-dimensional infrared spectroscopy. *The Journal of Chemical Physics*, 120(17):8067–8078, May 2004.

[100] Z. Li, D. Abramavicius, and S. Mukamel. Probing electron correlations in molecules by two-dimensional coherent optical spectroscopy. *Journal of the American Chemical Society*, 130(11):3509–3515, 2008.

[101] J. Kim, S. Mukamel, and G.D. Scholes. Two-dimensional electronic double-quantum coherence spectroscopy. *Accounts of Chemical Research*, 42(9):1375–1384, September 2009.

[102] J. Kim, V.M. Huxter, C. Curutchet, and G.D. Scholes. Measurement of electron-electron interactions and correlations using two-dimensional electronic double-quantum coherence spectroscopy. *The Journal of Physical Chemistry A*, 113(44):12122–12133, November 2009.

[103] N. Christensson, F. Milota, A. Nemeth, I. Pugliesi, E. Riedle, J. Sperling, T. Pullerits, H.F. Kauffmann, and J. Hauer. Electronic Double-Quantum Coherences and Their Impact on Ultrafast Spectroscopy: The Example of β-Carotene. *The Journal of Physical Chemistry Letters*, 1:3366–3370, November 2010.

[104] L. Yang and S. Mukamel. Two-dimensional correlation spectroscopy of two-exciton resonances in semiconductor quantum wells. *Physical Review Letters*, 100(5):057402, 2008.

[105] L. Yang and S. Mukamel. Revealing exciton-exciton couplings in semiconductors using multidimensional four-wave mixing signals. *Physical Review B*, 77(7):75335, 2008.

[106] K.W. Stone, D.B. Turner, K. Gundogdu, S.T. Cundiff, and K.A. Nelson. Exciton-exciton correlations revealed by two-quantum, two-dimensional fourier transform optical spectroscopy. *Accounts of Chemical Research*, 42(9):1452–61, September 2009.

[107] D.B. Turner, K.W. Stone, K. Gundogdu, and K.A. Nelson. Three-dimensional electronic spectroscopy of excitons in GaAs quantum wells. *The Journal of Chemical Physics*, 131(14):144510, October 2009.

[108] K.W. Stone, K. Gundogdu, D.B. Turner, X. Li, S.T. Cundiff, and K.A. Nelson. Two-quantum 2D FT electronic spectroscopy of biexcitons in GaAs quantum wells. *Science*, 324(5931):1169–73, May 2009.

[109] D. Karaiskaj, A.D. Bristow, L. Yang, X. Dai, R.P. Mirin, S. Mukamel, and S.T. Cundiff. Two-Quantum Many-Body Coherences in Two-Dimensional Fourier-Transform Spectra of Exciton Resonances in Semiconductor Quantum Wells. *Physical Review Letters*, 104(11):117401, 2010.

[110] D.B. Turner and K.A. Nelson. Coherent measurements of high-order electronic correlations in quantum wells. *Nature*, 466(7310):1089–1092, August 2010.

[111] K.A. Velizhanin and A. Piryatinski. Probing Interband Coulomb Interactions in Semiconductor Nanostructures with 2D Double-Quantum Coherence Spectroscopy. *The Journal of Physical Chemistry B*, 115(18):5372–82, May 2011.

[112] D. Abramavicius, B. Palmieri, and S. Mukamel. Extracting single and two-exciton couplings in photosynthetic complexes by coherent two-dimensional electronic spectra. *Chemical Physics*, 357(1-3):79–84, 2009.

[113] X. Dai, M. Richter, H. Li, A.D. Bristow, C. Falvo, S. Mukamel, and S.T. Cundiff. Two-Dimensional Double-Quantum Spectra Reveal Collective Resonances in an Atomic Vapor. *Physical Review Letters*, 108(19):193201, May 2012.

[114] M. Cho. Nonlinear response functions for the three-dimensional spectroscopies. *The Journal of Chemical Physics*, 115(10):4424, 2001.

[115] F. Ding and M.T. Zanni. Heterodyned 3D IR spectroscopy. *Chemical Physics*, 341(1-3):95–105, 2007.

[116] S. Garrett-Roe and P. Hamm. Purely absorptive three-dimensional infrared spectroscopy. *The Journal of Chemical Physics*, 130(16):164510, 2009.

[117] J.A. Davis, C.R. Hall, L.V. Dao, K.A. Nugent, H.M. Quiney, H.H. Tan, and C. Jagadish. Three-dimensional electronic spectroscopy of excitons in asymmetric double quantum wells. *The Journal of Chemical Physics*, 135(4):044510, 2011.

[118] S. Mukamel. Multidimensinoal Femtosecond Correlation Spectroscopies of Electronic and Vibrational Excitations. *Annual Review of Physical Chemistry*, 51:691–729, 2000.

[119] M. Cho. Coherent two-dimensional optical spectroscopy. *Chemical Reviews*, 108:1331–1418, 2008.

[120] M. Cho. *Two-Dimensional Optical Spectroscopy.* CRC Press, Boca Raton, FL, 2009.

[121] R.R. Ernst, G. Bodenhausen, and A. Wokaun. *Principles of Nuclear Magnetic Resonance in One and Two Dimensions.* Clarendon, Oxford, 1987.

[122] M. Khalil, N. Demirdöven, and A. Tokmakoff. Obtaining Absorptive Line Shapes in Two-Dimensional Infrared Vibrational Correlation Spectra. *Physical Review Letters*, 90(4):047401, January 2003.

[123] A.D. Bristow, D. Karaiskaj, X. Dai, T. Zhang, C. Carlsson, K.R. Hagen, R. Jimenez, and S.T. Cundiff. A versatile ultrastable platform for optical multidimensional Fourier-transform spectroscopy. *Review of Scientific Instruments*, 80(7):073108, July 2009.

[124] P.F. Tekavec, G.A. Lott, and A.H. Marcus. Fluorescence-detected two-dimensional electronic coherence spectroscopy by acousto-optic phase modulation. *The Journal of Chemical Physics*, 127(21):214307, December 2007.

[125] M. Aeschlimann, T. Brixner, A. Fischer, C. Kramer, P. Melchior, W. Pfeiffer, C. Schneider, C. Strüber, P. Tuchscherer, and D.V. Voronine. Coherent Two-Dimensional Nanoscopy. *Science*, 333:1723, August 2011.

[126] E. Harel, A.F. Fidler, and G.S. Engel. Real-time mapping of electronic structure with single-shot two-dimensional electronic spectroscopy. *Proceedings of the National Academy of Sciences*, 107(38):16444–7, September 2010.

[127] E. Harel, A.F. Fidler, and G.S. Engel. Single-shot gradient-assisted photon echo electronic spectroscopy. *The Journal of Physical Chemistry A*, 115(16):3787–3796, April 2011.

[128] E. Harel, P.D. Long, and G.S. Engel. Single-shot ultrabroadband two-dimensional electronic spectroscopy of the light-harvesting complex LH2. *Optics Letters*, 36(9):1665–1667, May 2011.

[129] T. Brixner, I.V. Stiopkin, and G.R. Fleming. Tunable two-dimensional femtosecond spectroscopy. *Optics Letters*, 29(8):884–886, 2004.

[130] T. Brixner, T. Mancal, I.V. Stiopkin, and G.R. Fleming. Phase-stabilized two-dimensional electronic spectroscopy. *The Journal of Chemical Physics*, 121(9):4221–4236, September 2004.

[131] P. Tian, D. Keusters, Y. Suzaki, and W.S. Warren. Femtosecond phase-coherent two-dimensional spectroscopy. *Science*, 300:1553–1555, 2003.

[132] E.M. Grumstrup, S.H. Shim, M.A. Montgomery, N.H. Damrauer, and M.T. Zanni. Facile collection of two-dimensional electronic spectra using femtosecond pulse-shaping Technology. *Optics Express*, 15(25):16681, 2007.

[133] J.C. Vaughan, T. Hornung, K.W. Stone, and K.A. Nelson. Coherently controlled ultrafast four-wave mixing spectroscopy. *The Journal of Physical Chemistry A*, 111(23):4873–4883, June 2007.

[134] J.A. Myers, K.L.M. Lewis, P.F. Tekavec, and J.P. Ogilvie. Two-color two-dimensional Fourier transform electronic spectroscopy with a pulse-shaper. *Optics express*, 16(22):17420–17428, October 2008.

[135] V.I. Prokhorenko, A. Halpin, and R.J.D. Miller. Coherently-controlled two-dimensional photon echo electronic spectroscopy. *Optics Express*, 17(12):9764, 2009.

[136] D.B. Turner, K.W. Stone, K. Gundogdu, and K.A. Nelson. Invited Article: The coherent optical laser beam recombination technique (COLBERT) spectrometer: Coherent multidimensional spectroscopy made easier. *Review of Scientific Instruments*, 82(8):081301, 2011.

[137] L. Lepetit, G. Cheriaux, and M. Joffre. Linear techniques of phase measurement by femtosecond spectral interferometry for applications in spectroscopy. *Journal of the Optical Society of America B*, 12(12):2467–2474, 1995.

[138] M.F. Emde, W.P. de Boeij, M.S. Pshenichnikov, and D.A. Wiersma. Spectral interferometry as an alternative to time-domain heterodyning. *Optics Letters*, 22(17):1338–1340, September 1997.

[139] S.M. Gallagher Faeder, A.W. Albrecht, J.D. Hybl, B.L. Landin, B. Rajaram, and D.M. Jonas. Heterodyne detection of the complete electric field of femtosecond four-wave mixing signals. *Journal of the Optical Society of America B*, 15(8):2338–2345, August 1998.

[140] J.C. Vaughan. *Two-Dimensional Ultrafast Pulse Shaping and its Application to Coherent Control and Spectroscopy.* PhD thesis, Massachusetts Institute of Technology, 2005.

[141] K.W. Stone. *Coherent multi-exciton dynamics in semiconductor nanostructures via two-dimensional Fourier Transform optical spectroscopy.* PhD thesis, Massachusetts Institute of Technology, 2009.

[142] D.B. Turner. *Investigating Exciton Correlations Using Coherent Multidimensional Optical Spectroscopy.* PhD thesis, Massachusetts Institute of Technology, 2010.

[143] G. Cerullo, M. Nisoli, and S. De Silvestri. Generation of 11 fs pulses tunable across the visible by optical parametric amplification. *Applied Physics Letters*, 71(25):3616, 1997.

[144] T. Wilhelm, J. Piel, and E. Riedle. Sub-20-fs pulses tunable across the visible from a blue-pumped single-pass noncollinear parametric converter. *Optics Letters*, 22(19):1494–1496, 1997.

[145] G. Cerullo, M. Nisoli, S. Stagira, and S. De Silvestri. Sub-8-fs pulses from an ultrabroadband optical parametric amplifier in the visible. *Optics Letters*, 23(16):1283–1285, August 1998.

[146] E. Riedle, M. Beutter, S. Lochbrunner, J. Piel, S. Schenkl, S. Spörlein, and W. Zinth. Generation of 10 to 50 fs pulses tunable through all of the visible and the NIR. *Applied Physics B: Lasers and Optics*, 71(3):457–465, 2000.

[147] G. Cerullo and S. De Silvestri. Ultrafast optical parametric amplifiers. *Review of Scientific Instruments*, 74(1):1–18, 2003.

[148] J. Piel, E. Riedle, L. Gundlach, R. Ernstorfer, and R. Eichberger. Sub-20 fs visible pulses with 750 nJ energy from a 100 kHz noncollinear optical parametric amplifier. *Optics Letters*, 31(9):1289–1291, May 2006.

[149] P.J.M. Johnson, V.I. Prokhorenko, and R.J.D. Miller. Enhanced bandwidth noncollinear optical parametric amplification with a narrowband anamorphic pump. *Optics Letters*, 36(11):2170–2172, June 2011.

[150] A.M. Weiner. Femtosecond pulse shaping using spatial light modulators. *Review of Scientific Instruments*, 71(5):1929–1960, 2000.

[151] J.C. Vaughan, T. Feurer, and K.A. Nelson. Automated two-dimensional femtosecond pulse shaping. *Journal of the Optical Society of America B*, 19(10):2489–2495, 2002.

[152] T. Feurer, J.C. Vaughan, R.M. Koehl, and K.A. Nelson. Multidimensional control of femtosecond pulses by use of a programmable liquid-crystal matrix. *Optics Letters*, 27(8):652–654, 2002.

[153] J.C. Vaughan. *Two-Dimensional Ultrafast Pulse Shaping and its Application to Coherent Control and Spectroscopy.* PhD thesis, Massachusetts Institute of Technology, 2005.

[154] J.C. Vaughan, T. Hornung, T. Feurer, and K.A. Nelson. Diffraction-based femtosecond pulse shaping with a two-dimensional spatial light modulator. *Optics Letters*, 30(3):323–325, 2005.

[155] A.M. Weiner, D.E. Leaird, G.P. Wiederrecht, and K.A. Nelson. Femtosecond pulse sequences used for optical manipulation of molecular motion. *Science*, 247(4948):1317, 1990.

[156] D. Meshulach and Y. Silberberg. Coherent quantum control of two-photon transitions by a femtosecond laser pulse. *Nature*, 396:239–242, 1998.

[157] N. Dudovich, B. Dayan, S.M. Gallagher Faeder, and Y. Silberberg. Transform-Limited Pulses Are Not Optimal for Resonant Multiphoton Transitions. *Physical Review Letters*, 86(1):47–50, 2001.

[158] M. Dantus. Coherent Nonlinear Spectroscopy: From Femtosecond Dynamics to Control. *Annual Review of Physical Chemistry*, 52:639–79, 2001.

[159] Y. Silberberg. Quantum coherent control for nonlinear spectroscopy and microscopy. *Annual Review of Physical Chemistry*, 60:277–292, 2009.

[160] D. Brinks, F.D. Stefani, F. Kulzer, R. Hildner, T.H. Taminiau, Y. Avlasevich, K. Mu, and N.F. van Hulst. Visualizing and controlling vibrational wave packets of single molecules. *Nature*, 465:905–909, 2010.

[161] R. Hildner, D. Brinks, and N.F. van Hulst. Femtosecond coherence and quantum control of single molecules at room temperature. *Nature Physics*, 7(2):172–177, December 2010.

[162] K. Gundogdu, K.W. Stone, D.B. Turner, and K.A. Nelson. Multidimensional coherent spectroscopy made easy. *Chemical Physics*, 341(1-3):89–94, November 2007.

[163] A.A. Maznev, T.F. Crimmins, and K.A. Nelson. How to make femtosecond pulses overlap. *Optics Letters*, 23(17):1378–1380, 1998.

[164] G.D. Goodno, G. Dadusc, and R.J.D. Miller. Ultrafast heterodyne-detected transient-grating spectroscopy using diffractive optics. *Journal of the Optical Society of America B*, 15(6):1791–1794, 1998.

[165] A.A. Maznev, K.A. Nelson, and J.A. Rogers. Optical heterodyne detection of laser-induced gratings. *Optics Letters*, 23(16):1319–1321, August 1998.

[166] D.J. Kane and R. Trebino. Characterization of Arbitrary Femtosecond Pulses Using Frequency-Resolved Optical Gating. *IEEE Journal of Quantum Electronics*, 29(2):571–579, 1993.

[167] R. Trebino and D.J. Kane. Using phase retrieval to measure the intensity and phase of ultrashort pulses: frequency-resolved optical gating. *Journal of the Optical Society of America A*, 10(5):1101, May 1993.

[168] Q.-H. Xu, Y. Ma, and G.R. Fleming. Heterodyne detected transient grating spectroscopy in resonant and non-resonant systems using a simplied diffractive optics method. *Chemical Physics Letters*, 338(4-6):254–262, April 2001.

[169] J.P. Ogilvie, M. Plazanet, G. Dadusc, and R.J.D. Miller. Dynamics of Ligand Escape in Myoglobin: Q-Band Transient Absorption and Four-Wave Mixing Studies. *The Journal of Physical Chemistry B*, 106(40):10460–10467, October 2002.

[170] C. Khurmi and M.A. Berg. Differential heterodyne detection with diffractive optics for multidimensional transient-grating spectroscopy. *Journal of the Optical Society of America B*, 26(12):2357–2362, 2009.

[171] C. Spitz and S. Daehne. Low temperature exciton-exciton annihilation in amphi-PIPE J-aggregates. *International Journal of Photoenergy*, 2006:84950, 2006.

[172] G.M. Akselrod, Y.R. Tischler, E.R. Young, D.G. Nocera, and V. Bulovic. Exciton-exciton annihilation in organic polariton microcavities. *Physical Review B*, 82(11):113106, September 2010.

[173] A.S. Davydov. *Theory of Molecular Excitons*. Plenum Press, New York, NY, 1 edition, 1971.

[174] P. Kjellberg and T. Pullerits. Three-pulse photon echo of an excitonic dimer modeled via Redfield theory. *The Journal of Chemical Physics*, 124:024106, 2006.

[175] P. Kjellberg, B. Brüggemann, and T. Pullerits. Two-dimensional electronic spectroscopy of an excitonically coupled dimer. *Physical Review B*, 74(2):024303, July 2006.

[176] H. Fidder, J. Knoester, and D.A. Wiersma. Optical properties of disordered molecular aggregates: A numerical study. *The Journal of Chemical Physics*, 95(11):7880, 1991.

[177] J. Knoester. Nonlinear optical line shapes of disordered molecular aggregates: Motional narrowing and the effect of intersite correlations. *The Journal of Chemical Physics*, 99(11):8466–8479, 1993.

[178] R.M. Hochstrasser and J.D. Whiteman. Exciton Band Structure and Properties of a Real Linear Chain in a Molecular Crystal. *The Journal of Chemical Physics*, 56(12):5945–5958, 1972.

[179] L.D. Bakalis and J. Knoester. PumpProbe Spectroscopy and the Exciton Delocalization Length in Molecular Aggregates. *The Journal of Physical Chemistry B*, 103(31):6620–6628, August 1999.

[180] M.S. Skolnick, T.A. Fisher, and D.M. Whittaker. Strong coupling phenomena in quantum microcavity structures. *Semiconductor Science and Technology*, 13:645–669, 1998.

[181] F.C. Spano, J.R. Kuklinski, and S. Mukamel. Temperature-Dependent Superradiant Decay of Excitons in Small Aggregates. *Physical Review Letters*, 65(2):211–214, 1990.

[182] H. Fidder, J. Knoester, and D.A. Wiersma. Superradiant emission and optical dephasing in J-aggregates. *Chemical Physics Letters*, 171(5-6):529–536, August 1990.

[183] V.A. Malyshev. Localization length of one-dimensional exciton and low-temperature behaviour of radiative lifetime of J-aggregated dye solutions. *Journal of Luminescence*, 55(5-6):225–230, August 1993.

[184] T. Meier, V. Chernyak, and S. Mukamel. Multiple Exciton Coherence Sizes in Photosynthetic Antenna Complexes viewed by PumpProbe Spectroscopy. *The Journal of Physical Chemistry B*, 101(37):7332–7342, September 1997.

[185] I.V. Stiopkin, T. Brixner, M. Yang, and G.R. Fleming. Heterogeneous exciton dynamics revealed by two-dimensional optical spectroscopy. *The Journal of Physical Chemistry B*, 110(40):20032–7, 2006.

[186] E.W. Knapp. Lineshapes of Molecular Aggregates. Exchange Narrowing and Intersite Correlations. *Chemical Physics*, 85(1):73–82, March 1984.

[187] N. Bloembergen, E.M. Purcell, and R.V. Pound. Relaxation Effects in Nuclear Magnetic Resonance Absorption. *Physical Review*, 73(7):679–715, 1948.

[188] D.M. Whittaker, P. Kinsler, T.A. Fisher, M.S. Skolnick, A. Armitage, A.M. Afshar, M.D. Sturge, and J.S. Roberts. Motional Narrowing in Semiconductor Microcavities. *Physical Review Letters*, 77(23):4792–4795, December 1996.

[189] D.W. Oxtoby. Hydrodynamic theory for vibrational dephasing in liquids. *The Journal of Chemical Physics*, 70(6):2605, 1979.

[190] A. Berthelot, I. Favero, G. Cassabois, C. Voisin, C. Delalande, Ph. Roussignol, R. Ferreira, and J.M. Gérard. Unconventional motional narrowing in the optical spectrum of a semiconductor quantum dot. *Nature Physics*, 2(11):759–764, October 2006.

[191] P.W. Anderson. Absence of Diffusion in Certain Random Lattices. *Physical Review*, 109(5):1492–1505, 1958.

[192] J.L. Skinner. Models of Anderson Localization. *The Journal of Physical Chemistry*, 98(10):2503–2507, March 1994.

[193] D. Abramavicius, B. Palmieri, D.V. Voronine, F. Sanda, and S. Mukamel. Coherent multidimensional optical spectroscopy of excitons in molecular aggregates; quasiparticle versus supermolecule perspectives. *Chemical Reviews*, 109(6):2350–2408, June 2009.

[194] A.G. Redfield. On the Theory of Relaxation Processes. *IBM Journal of Research and Development*, 1(1):19–31, 1957.

[195] A.G. Redfield. *The Theory of Relaxation Processes*, volume 1. Academic Press, New York, January 1965.

[196] W.M. Zhang, T. Meier, V. Chernyak, and S. Mukamel. Exciton-migration and three-pulse femtosecond optical spectroscopies of photosynthetic antenna complexes. *The Journal of Chemical Physics*, 108(18):7763, 1998.

[197] M. Yang and G.R. Fleming. Influence of phonons on exciton transfer dynamics: comparison of the Redfield, Forster, and modified Redfield equations. *Chemical Physics*, 275:355–372, 2002.

[198] M. Wubs and J. Knoester. Exchange narrowing in dynamically disordered molecular aggregates. *Chemical Physics Letters*, 284:63–70, 1998.

[199] F.C. Spano. The Spectral Signatures of Frenkel Polarons in H- and J-Aggregates. *Accounts of Chemical Research*, 43(3):429–39, March 2010.

[200] M.P. Bednarz, V.A. Malyshev, and J. Knoester. Intraband relaxation and temperature dependence of the fluorescence decay time of one-dimensional Frenkel excitons: The Pauli master equation approach. *The Journal of Chemical Physics*, 117(13):6200, 2002.

[201] M.P. Bednarz, V.A. Malyshev, and J. Knoester. Temperature Dependent Fluorescence in Disordered Frenkel Chains: Interplay of Equilibration and Local Band-Edge Level Structure. *Physical Review Letters*, 91(21):217401, November 2003.

[202] D.J. Heijs, V.A. Malyshev, and J. Knoester. Thermal broadening of the J-band in disordered linear molecular aggregates: a theoretical study. *The Journal of Chemical Physics*, 123(14):144507, October 2005.

[203] D.J. Heijs, V.A. Malyshev, and J. Knoester. Decoherence of Excitons in Multichromophore Systems: Thermal Line Broadening and Destruction of Superradiant Emission. *Physical Review Letters*, 95(17):177402, October 2005.

[204] D.J. Heijs, A.G. Dijkstra, and J. Knoester. Ultrafast pump-probe spectroscopy of linear molecular aggregates: Effects of exciton coherence and thermal dephasing. *Chemical Physics*, 341(1-3):230–239, November 2007.

[205] M. Wendling, T. Pullerits, M.A. Przyjalgowski, S.I.E. Vulto, T.J. Aartsma, R. van Grondelle, and H. van Amerongen. Electron-Vibrational Coupling in the Fenna-Matthews-Olson Complex of Prosthecochloris aestuarii Determined by Temperature-Dependent Absorption and Fluorescence Line-Narrowing Measurements. *The Journal of Physical Chemistry B*, 104:5825–5831, 2000.

[206] M. Cho, H.M. Vaswani, T. Brixner, J. Stenger, and G.R. Fleming. Exciton analysis in 2D electronic spectroscopy. *The Journal of Physical Chemistry B*, 109(21):10542–10556, 2005.

[207] D. Abramavicius and S. Mukamel. Exciton dynamics in chromophore aggregates with correlated environment fluctuations. *The Journal of Chemical Physics*, 134(17):174504, 2011.

[208] J. Knoester. Nonlinear optical susceptibilities of disordered aggregates. A comparison of schemes to account for intermolecular interactions. *Physical Review A*, 47(3):2083, 1993.

[209] D. Abramavicius, B. Palmieri, and S. Mukamel. Extracting single and two-exciton couplings in photosynthetic complexes by coherent two-dimensional electronic spectra. *Chemical Physics*, 357(1-3):79–84, 2009.

[210] G. Juzeliunas and P. Reineker. Pumpprobe spectra of linear molecular aggregates: Effect of excitonexciton interaction and higher molecular levels. *The Journal of Chemical Physics*, 109(16):6916, 1998.

[211] V.A. Malyshev, H. Glaeske, and K.-H. Feller. Excitonexciton annihilation in linear molecular aggregates at low temperature. *Chemical Physics Letters*, 305(1-2):117–122, May 1999.

[212] O. Golonzka, M. Khalil, N. Demirdöven, and A. Tokmakoff. Vibrational anharmonicities revealed by coherent two-dimensional infrared spectroscopy. *Physical review letters*, 86(10):2154–2157, 2001.

[213] O. Golonzka, M. Khalil, N. Demirdoven, and A. Tokmakoff. Coupling and orientation between anharmonic vibrations characterized with two-dimensional

infrared vibrational echo spectroscopy. *The Journal of Chemical Physics*, 115(23):10814, 2001.

[214] B. Brüggemann and V. May. Exciton exciton annihilation dynamics in chromophore complexes. I. Multiexciton density matrix formulation. *The Journal of Chemical Physics*, 118(2):746, 2003.

[215] B. Brüggemann and V. May. Exciton exciton annihilation dynamics in chromophore complexes. II. Intensity dependent transient absorption of the LH2 antenna system. *The Journal of Chemical Physics*, 120(5):2325–36, February 2004.

[216] H. von Berlepsch, S. Kirstein, R. Hania, C. Didraga, A. Pugzlys, and C. Bottcher. Stabilization of individual tubular J-aggregates by poly(vinyl alcohol). *The Journal of Physical Chemistry B*, 107(51):14176–14184, 2003.

[217] D.M. Eisele, C.W. Cone, E.A. Bloemsma, S.M. Vlaming, C.G.F. van der Kwaak, R.J. Silbey, M.G. Bawendi, J. Knoester, J.P. Rabe, and D.A. Vanden Bout. Utilizing redox-chemistry to elucidate the nature of exciton transitions in supramolecular dye nanotubes. *Nature Chemistry*, 4:655–662, July 2012.

[218] C. Didraga, J.A. Klugkist, and J. Knoester. Optical Properties of Helical Cylindrical Molecular Aggregates: The Homogeneous Limit. *The Journal of Physical Chemistry B*, 106(44):11474–11486, November 2002.

[219] C. Didraga, A. Pugzlys, P.R. Hania, H. von Berlepsch, K. Duppen, and J. Knoester. Structure, spectroscopy, and microscopic model of tubular carbocyanine dye aggregates. *The Journal of Physical Chemistry B*, 108(39):14976–14985, 2004.

[220] C. Didraga and J. Knoester. Chiral exciton wave functions in cylindrical J aggregates. *The Journal of Chemical Physics*, 121(2):946–59, 2004.

[221] S.M. Vlaming, E.A. Bloemsma, M.L. Nietiadi, and J. Knoester. Disorder-induced exciton localization and violation of optical selection rules in supramolecular nanotubes. *The Journal of Chemical Physics*, 134(11):114507, 2011.

[222] D.H. Arias, K.W. Stone, S.M. Vlaming, B.J. Walker, M.G. Bawendi, R.J. Silbey, V. Bulović, and K.A. Nelson. Thermally-Limited Exciton Delocalization in Superradiant Molecular Aggregates. *The Journal of Physical Chemistry B*, December 2012.

[223] E. Collini, C.Y. Wong, K.E. Wilk, P.M.G. Curmi, P. Brumer, and G.D. Scholes. Coherently wired light-harvesting in photosynthetic marine algae at ambient temperature. *Nature*, 463(7281):644–647, 2010.

[224] G.M. Akselrod, B.J. Walker, W.A. Tisdale, M.G. Bawendi, and V. Bulovic. Twenty-Fold Enhancement of Molecular Fluorescence by Coupling to a J-Aggregate Critically Coupled Resonator. *ACS Nano*, 6(1):467–71, January 2012.

[225] S. de Boer and D.A. Wiersma. Dephasing-Induced Damping of Superradiant Emission in J-Aggregates. *Chemical Physics Letters*, 165(1):45–53, 1990.

[226] D. Beljonne, C. Curutchet, G.D. Scholes, and R.J. Silbey. Beyond Förster resonance energy transfer in biological and nanoscale systems. *The Journal of Physical Chemistry B*, 113(19):6583–99, May 2009.

[227] E.V. Emelianova, S. Athanasopoulos, R.J. Silbey, and D. Beljonne. 2D Excitons as Primary Energy Carriers in Organic Crystals: The Case of Oligoacenes. *Physical Review Letters*, 104(20):206405, May 2010.

[228] S. Athanasopoulos, E.V. Emelianova, A.B. Walker, and D. Beljonne. Exciton diffusion in energetically disordered organic materials. *Physical Review B*, 80(19):195209, November 2009.

[229] A. Huijser, T.J. Savenije, S.C.J. Meskers, M.J.W. Vermeulen, and L.D.A. Siebbeles. The Mechanism of Long-Range Exciton Diffusion in a Nematically Organized Porphyrin Layer. *Journal of the American Chemical Society*, 130(37):12496–500, September 2008.

[230] S. Valleau, S.K. Saikin, M. Yung, and A. Aspuru-Guzik. Exciton transport in thin-film cyanine dye J-aggregates. *The Journal of Chemical Physics*, 137(3):034109, 2012.

[231] J. Wenus, S. Ceccarelli, D.G. Lidzey, A.I. Tolmachev, J.L. Slominskii, and J.L. Bricks. Optical strong coupling in microcavities containing J-aggregates absorbing in near-infrared spectral range. *Organic Electronics*, 8(2-3):120–126, 2007.

[232] E. Collini and G.D. Scholes. Coherent intrachain energy migration in a conjugated polymer at room temperature. *Science*, 323(5912):369–73, January 2009.

[233] A. Tokmakoff. Two-Dimensional Line Shapes Derived from Coherent Third-Order Nonlinear Spectroscopy. *The Journal of Physical Chemistry A*, 104(18):4247–4255, May 2000.

[234] M.E. Siemens, G. Moody, H. Li, A.D. Bristow, and S.T. Cundiff. Resonance lineshapes in two-dimensional Fourier transform spectroscopy. *Optics Express*, 18(17):17699–708, August 2010.

[235] J.R. Durrant, J. Knoester, and D.A. Wiersma. Local energetic disorder in molecular aggregates probed by the one-exciton to two-exciton transition. *Chemical Physics Letters*, 222(5):450–456, May 1994.

[236] J.C. Vaughan, T. Feurer, K.W. Stone, and K.A. Nelson. Analysis of replica pulses in femtosecond pulse shaping with pixelated devices. *Optics Express*, 14(3):1314, 2006.

[237] A. Pugzlys, P.R. Hania, R. Augulis, K. Duppen, and P.H.M. van Loosdrecht. Cylindrical aggregates of 5,5',6,6'-tetrachlorobenzimida-carbocyanine amphiphilic derivatives: Structure-related optical properties and exciton dynamics. *International Journal of Photoenergy*, 2006:1–10, 2006.

[238] V.A. Malyshev. Length of 1D-Exciton Localizatoin and Temperature-Dependence of Radiative Lifetime for Frozen-Solutions of Dyes with J-aggregates. *Optics and Spectroscopy*, 71(6):873–875, 1991.

[239] V.A. Malyshev and P. Moreno. Hidden structure of the low-energy spectrum of a one-dimensional localized Frenkel exciton. *Physical Review B*, 51(20):14587–14593, 1995.

[240] L. Schultheis, A. Honold, J. Kuhl, K. Köhler, and C.W. Tu. Optical dephasing of homogeneously broadened two-dimensional exciton transitions in GaAs quantum wells. *Physical Review B*, 34(12):9027, 1986.

[241] H. Lee, Y.C. Cheng, and G.R. Fleming. Coherence dynamics in photosynthesis: protein protection of excitonic coherence. *Science*, 316(5830):1462–1465, June 2007.

[242] G.D. Scholes. Quantum-Coherent Electronic Energy Transfer: Did Nature Think of It First? *The Journal of Physical Chemistry Letters*, 1(1):2–8, 2010.

[243] C.Y. Wong, R.M. Alvey, D.B. Turner, K.E. Wilk, D.A. Bryant, P.M.G. Curmi, R.J. Silbey, and G.D. Scholes. Electronic coherence lineshapes reveal hidden excitonic correlations in photosynthetic light harvesting. *Nature Chemistry*, 4(5):396–404, March 2012.

[244] G.S. Schlau-Cohen, A. Ishizaki, T.R. Calhoun, N.S. Ginsberg, M. Ballottari, R. Bassi, and G.R. Fleming. Elucidation of the timescales and origins of quantum electronic coherence in LHCII. *Nature Chemistry*, 4(5):389–395, March 2012.

[245] J.L. Mchale. Hierarchal Light-Harvesting Aggregates and Their Potential for Solar Energy Applications. *The Journal of Physical Chemistry Letters*, 3:587–597, 2012.

[246] H. von Berlepsch, K. Ludwig, S. Kirstein, and C. Böttcher. Mixtures of achiral amphiphilic cyanine dyes form helical tubular J-aggregates. *Chemical Physics*, 385(1-3):27–34, June 2011.

[247] S.S. Lampoura, C. Spitz, S. Dahne, J. Knoester, and K. Duppen. The Optical Dynamics of Excitons in Cylindrical J-Aggregates. *The Journal of Physical Chemistry B*, 106(12):3103–3111, 2002.

[248] F. Milota, J. Sperling, A. Nemeth, T. Mancal, and H.F. Kauffmann. Two-dimensional electronic spectroscopy of molecular excitons. *Accounts of Chemical Research*, 42(9):1364–1374, September 2009.

[249] J. Knoester. Modeling the optical properties of excitons in linear and tubular J-aggregates. *International Journal of Photoenergy*, 2006:61364, 2006.

[250] H. von Berlepsch, S. Kirstein, R. Hania, A. Pugzlys, and C. Böttcher. Modification of the nanoscale structure of the J-aggregate of a sulfonate-substituted amphiphilic carbocyanine dye through incorporation of surface-active additives. *The Journal of Physical Chemistry B*, 111(7):1701–11, February 2007.

[251] J.A. Myers, K.L.M. Lewis, F.D. Fuller, P.F. Tekavec, C.F. Yocum, and J.P. Ogilvie. Two-Dimensional Electronic Spectroscopy of the D1-D2-cyt b559 Photosystem II Reaction Center Complex. *The Journal of Physical Chemistry Letters*, 1(19):2774–2780, October 2010.

[252] G. Panitchayangkoon, D. Hayes, K.A. Fransted, J.R. Caram, E. Harel, J. Wen, R.E. Blankenship, and G.S. Engel. Long-lived quantum coherence in photosynthetic complexes at physiological temperature. *Proceedings of the National Academy of Sciences*, 107(29):12766–12770, July 2010.

[253] G. Panitchayangkoon, D.V. Voronine, D. Abramavicius, J.R. Caram, N.H.C. Lewis, S. Mukamel, and G.S. Engel. Direct evidence of quantum transport in photosynthetic light-harvesting complexes. *Proceedings of the National Academy of Sciences*, 108(52):20908–20912, December 2011.

[254] G.S. Schlau-Cohen, A. Ishizaki, and G.R. Fleming. Two-dimensional electronic spectroscopy and photosynthesis: Fundamentals and applications to photosynthetic light-harvesting. *Chemical Physics*, 386(1-3):1–22, May 2011.

[255] K.L.M. Lewis and J.P. Ogilvie. Probing Photosynthetic Energy and Charge Transfer with Two-Dimensional Electronic Spectroscopy. *The Journal of Physical Chemistry Letters*, 3:503–510, 2012.

[256] J.M. Anna, E.E. Ostroumov, K. Maghlaoui, J. Barber, and G.D. Scholes. Two-Dimensional Electronic Spectroscopy Reveals Ultrafast Downhill Energy Transfer in Photosystem I Trimers of the Cyanobacterium Thermosynechococcus elongatus. *The Journal of Physical Chemistry Letters*, 3:3677–3684, 2012.

[257] E.E. Ostroumov, R.M. Mulvaney, R.J. Cogdell, and G.D. Scholes. Broadband 2D Electronic Spectroscopy Reveals a Carotenoid Dark State in Purple Bacteria. *Science*, 340(6128):52–56, April 2013.

[258] E.L. Read, G.S. Engel, T.R. Calhoun, T. Mancal, T.K. Ahn, R.E. Blankenship, and G.R. Fleming. Cross-peak-specific two-dimensional electronic spectroscopy. *Proceedings of the National Academy of Sciences*, 104(36):14203–14208, September 2007.

[259] H. Fidder, J. Knoester, and D.A. Wiersma. Observation of the one-exciton to two-exciton transition in a J aggregate. *The Journal of Chemical Physics*, 98(8):6564, 1993.

[260] A. Pugžlys, P.R. Hania, C. Didraga, J. Knoester, and K. Duppen. Cylindrical Aggregates of TDBC: Linear and Nonlinear Optical Properties Versus Morphology. *Solid State Phenomena*, 97-98:201–206, 2004.

[261] R. Augulis, A. Pugžlys, and P.H.M. Van Loosdrecht. Exciton dynamics in molecular aggregates. *Physica Status Solidi (C)*, 3(10):3400–3403, November 2006.

[262] M.A. Nielsen and I.L. Chuang. *Quantum Computation and Quantum Information*. Cambridge University Press, Cambridge, 2000.

[263] M. Mohseni and D.A. Lidar. Direct Characterization of Quantum Dynamics. *Physical Review Letters*, 97(17):170501, October 2006.

[264] J. Yuen-Zhou, J.J. Krich, I. Kassal, and A. Aspuru-Guzik. Ultrafast spectroscopy: Wavepackets and Quantum Information. In *Ultrafast Dynamics in Biomolecular Systems*. PanStanford, Singapore, 2013.

[265] Y. Glickman, S. Kotler, N. Akerman, and R. Ozeri. Emergence of a Measurement Basis in Atom-Photon Scattering. *Science*, 339:1187–1191, 2013.

[266] M. Neeley, M. Ansmann, R.C. Bialczak, M. Hofheinz, N. Katz, E. Lucero, A. OConnell, H. Wang, A.N. Cleland, and J.M. Martinis. Process tomography of quantum memory in a Josephson-phase qubit coupled to a two-level state. *Nature Physics*, 4(7):523–526, April 2008.

[267] D. Nigg, J.T. Barreiro, P. Schindler, M. Mohseni, T. Monz, M. Chwalla, M. Hennrich, and R. Blatt. Experimental Characterization of Quantum Dynamics Through Many-Body Interactions. *Physical Review Letters*, 110(6):060403, February 2013.

[268] J. Yuen-Zhou, J.J. Krich, M. Mohseni, and A. Aspuru-Guzik. Quantum state and process tomography of energy transfer systems via ultrafast spectroscopy. *Proceedings of the National Academy of Sciences*, 108(43):17615–17620, October 2011.

[269] J. Yuen-Zhou and A. Aspuru-guzik. Quantum process tomography of excitonic dimers from two-dimensional electronic spectroscopy. I. General theory and application to homodimers. *The Journal of Chemical Physics*, 134505:134505, 2011.

[270] S. Hoyer and K.B. Whaley. Inverting pump-probe spectroscopy for state tomography of excitonic systems. *The Journal of Chemical Physics*, 138(16):164102, 2013.

[271] M. Grant and S. Boyd. Matlab software for disciplined convex programming, version 1.21. http://cvxr.com/cvx, 2011.

[272] R.R. Cooney, S.L. Sewall, D.M. Sagar, and P. Kambhampati. Gain Control in Semiconductor Quantum Dots via State-Resolved Optical Pumping. *Physical Review Letters*, 102(12):127404, 2009.

[273] J. Xiao, Y. Wang, Z. Hua, X. Wang, C. Zhang, and M. Xiao. Carrier multiplication in semiconductor nanocrystals detected by energy transfer to organic dye molecules. *Nature Communications*, 3:1170, November 2012.

[274] Patanjali Kambhampati. Multiexcitons in Semiconductor Nanocrystals: A Platform for Optoelectronics at High Carrier Concentration. *The Journal of Physical Chemistry Letters*, 3(9):1182–1190, May 2012.

[275] P. W. Anderson. More is different. *Science*, 177(4047):393–396, 1972.

[276] J Shah. *Ultrafast Spectroscopy of Semiconductors and Semiconductor Nanostructures*. Springer Verlag, Berlin, 1999.

[277] Hartmut Haug and S. W Koch. *Quantum Theory of the Optical and Electronic Properties of Semiconductors*. World Scientific, New Jersey, 2009.

[278] J Hegarty, M. D. Sturge, A. C. Gossard, and W. Wiegmann. Resonant degenerate 4-wave mixing in gaas multiquantum well structures. *Appl. Phys. Lett.*, 40:132–134, 1982.

[279] D. A. B. Miller, D. S. Chemla, D. J. Eilenberger, P. W. Smith, A. C. Gossard, and W. Wiegmann. Degenerate four-wave mixing in room-temperature gaas/algaas multiple quantum well structures. *Appl. Phys. Lett.*, 42(11):925–927, 1983.

[280] L Schultheis, M. D. Sturge, and J. Hegarty. Photon-echoes from two-dimensional excitons in gaas-algaas quantum wells. *Appl. Phys. Lett.*, 47:995–997, 1985.

[281] D. S. Chemla and D. A. B. Miller. Room-temperature excitonic nonlinear-optical effects in semiconductor quantum-well structures. *J. Opt. Soc. Am. B*, 2(7):1155–1173, 1985.

[282] S. Schmitt-Rink, D. S. Chemla, and D. A. B. Miller. Theory of transient excitonic optical nonlinearities in semiconductor quantum-well structures. *Phys. Rev. B*, 32:6601–6609, 1985.

[283] L. Schultheis, J. Kuhl, A. Honold, and C. W. Tu. Picosecond phase coherence and orientational relaxation of excitons in gaas. *Phys. Rev. Lett.*, 57(1797-1800), 1986.

[284] L. Schultheis, A. Honold, J. Kuhl, K. Köhler, and C. W. Tu. Optical dephasing of homogeneously broadened two-dimensional exciton-transitions in gaas quantum-wells. *Phys. Rev. B*, 34:9027–9030, 1986.

[285] M. Lindberg and S. W. Koch. Effective bloch equations for semiconductors. *Phys. Rev. B*, 38:3342–3350, 1988.

[286] A. Honold, L. Schultheis, J. Kuhl, and C. W. Tu. Collision broadening of two-dimensional excitons in a gaas single quantum well. *Phys. Rev. B*, 40:6442–6445, 1989.

[287] M. Wegener, D. S. Chemla, S. Schmitt-Rink, and W. Schäfer. Line shape of time-resolved four-wave mixing. *Phys. Rev. A*, 42(9):5675–5683, Nov 1990.

[288] M. Koch, J. Feldmann, E.O. Göbel, P. Thomas, and K. Köhler. Quantum beats versus polarization interference: An experimental distinction. *Phys. Rev. Lett.*, 69(25):3631, 1992.

[289] J. Feldmann, T. Meier, G. von Plessen, M. Koch, E. O. Göbel, P. Thomas, G. Bacher, C. Hartmann, H. Schweizer, W. Schäfer, and H. Nickel. Coherent dynamics of excitonic wave-packets. *Phys. Rev. Lett.*, 70:3027–3030, 1993.

[290] A. Lohner, K. Rick, P. Leisching, A. Leitenstorfer, T. Elsaesser, T. Kuhn, F. Rossi, and W. Stolz. Coherent optical polarization of bulk gaas studied by femtosecond photon-echo spectroscopy. *Phys. Rev. Lett.*, 71:77–80, 1993.

[291] V. G. Lyssenko, J. Erland, I. Balslev, K. H. Pantke, B. S. Razbirin, and J. H. Hvam. Nature of nonlinear 4-wave-mixing beats in semiconductors. *Phys. Rev. B*, 48:5720–5723, 1993.

[292] V. M. Axt and A. Stahl. A dynamics-controlled truncation scheme for the hierarchy of density matrices in semiconductor optics. *Zeit. für Phys. B*, 93:195–204, 1994.

[293] A. Leitenstorfer, A. Lohner, K. Rick, P. Leisching, T. Elsaesser, T. Kuhn, F. Rossi, W. Stolz, and K. Ploog. Excitonic and free-carrier polarizations of bulk gaas studied by femtosecond coherent spectroscopy. *Phys. Rev. B*, 49:16372–16380, 1994.

[294] M. Koch, R. Hellmann, G. Bastian, J. Feldmann, E. O. Göbel, and P. Dawson. Enhanced energy and phase relaxation of excitons in the presence of bare electrons. *Phys. Rev. B*, 51:13887–13890, 1995.

[295] Steven T. Cundiff, M. Koch, W. H. Knox, and J. Shah. Optical coherence in semiconductors: Strong emission mediated by nondegenerate interactions. *Phys. Rev. Lett.*, 77:1107–1110, 1996.

[296] X. Chen, W.J. Walecki, O. Buccafusca, D.N. Fittinghoff, and A.L. Smirl. Temporally and spectrally resolved amplitude and phase of coherent four-wave-mixing emission from gaas quantum wells. *Phys. Rev. B*, 56(15):9738–9743, 1997.

[297] V. M. Axt and S. Mukamel. Nonlinear optics of semiconductor and molecular nanostructures; a common perspective. *Rev. Mod. Phys.*, 70(1):145–174, 1998.

[298] K. B. Ferrio and D. G. Steel. Raman quantum beats of interacting excitons. *Phys. Rev. Lett.*, 80(4):786–789, 1998.

[299] G. Manzke, Q. Y. Peng, K. Henneberger, U. Neukirch, K. Hauke, K. Wundke, J. Gutowski, and D. Hommel. Density dependence of the exciton energy in semiconductors. *Phys. Rev. Lett.*, 80(22):4943–4946, 1998.

[300] M. Phillips and H. Wang. Coherent oscillation in four-wave mixing of interacting excitons. *Solid State Comm.*, 111:317–321, 1999.

[301] A.L. Smirl, M. J. Stevens, X. Chen, and O. Buccafusca. Heavy-hole and light-hole oscillations in the coherent emission from quantum wells: Evidence for exciton-exciton correlations. *Phys. Rev. B*, 60:8267–8275, 1999.

[302] S. R. Bolton, U. Neukirch, L. J. Sham, and D. S. Chemla. Demonstration of sixth-order coulomb correlations in a semiconductor single quantum well. *Phys. Rev. Lett.*, 85:2002–2005, 2000.

[303] Camelia N Borca, Tianhao Zhang, Xiaoqin Li, and Steven T. Cundiff. Optical two-dimensional fourier transform spectroscopy of semiconductors. *Chem. Phys. Lett.*, 416:311–315, 2005.

[304] Xiaoqin Li, Tianhao Zhang, Camelia N Borca, and Steven T Cundiff. Many-body interactions in semiconductors probed by optical two-dimensional fourier transform spectroscopy. *Phys. Rev. Lett.*, 96(5):057406, Feb 2006.

[305] Tianhao Zhang, Irina Kuznetsova, Torsten Meier, Xiaoqin Li, Richard P Mirin, Peter Thomas, and Steven T Cundiff. Polarization-dependent optical 2d fourier transform spectroscopy of semiconductors. *Proc. Natl. Acad. Sci. U.S.A.*, 104(36):14227–14232, Sep 2007.

[306] Lijun Yang, Tianhao Zhang, Alan D Bristow, Steven T Cundiff, and Shaul Mukamel. Isolating excitonic raman coherence in semiconductors using two-dimensional correlation spectroscopy. *J. Chem. Phys.*, 129(23):234711, Dec 2008.

[307] Alan D. Bristow, Denis Karaiskaj, Xingcan Dai, Richard P. Mirin, and Steven T. Cundiff. Polarization dependence of semiconductor exciton and biexciton contributions to phase-resolved optical two-dimensional fourier-transform spectra. *Phys. Rev. B*, 79(16):161305(R), 2009.

[308] Xiaoqin Li, Tianhao Zhang, Shaul Mukamel, Richard P. Mirin, and Steven T. Cundiff. Investigation of electronic coupling in semiconductor double quantum wells using coherent optical two-dimensional fourier transform spectroscopy. *Solid State Comm.*, 149:361–366, 2009.

[309] Lijun Yang, Igor V. Schweigert, Steven T. Cundiff, and Shaul Mukamel. Two-dimensional optical spectroscopy of excitons in semiconductor quantum wells: Liouville-space pathway analysis. *Phys. Rev. B*, 75(12):125302, 2007.

[310] Lijun Yang and Shaul Mukamel. Revealing exciton-exciton couplings in semiconductors using multidimensional four-wave mixing signals. *Phys. Rev. B*, 77(7):075335, 2008.

[311] M. Kira and S. W. Koch. (not sure). *Prog. Quantum Electr.*, 30:155–296, 2006.

[312] R. P. Smith, J. K. Wahlstrand, A. C. Funk, R. P. Mirin, S. T. Cundiff, J. T. Steiner, M. Schafer, M. Kira, and S. W. Koch. Extraction of many-body configurations from nonlinear absorption in semiconductor quantum wells. *Phys. Rev. Lett.*, 104(24):247401, 2010.

[313] Alan D Bristow, Denis Karaiskaj, Xingcan Dai, and Steven T Cundiff. All-optical retrieval of the global phase for two-dimensional fourier-transform spectroscopy. *Opt. Express*, 16(22):18017–27, Oct 2008.

[314] N Demirdöven, M Khalil, and A Tokmakoff. Correlated vibrational dynamics revealed by two-dimensional infrared spectroscopy. *Phys. Rev. Lett.*, 89(23):237401, Dec 2002.